STUDY OF TISSUE TEMPERATURE DISTRIBUTION DURING LASER-IMMUNOTHERAPY FOR CANCER TREATMENT

By

SURYA C. GNYAWALI

Master of Science
Tribhuvan University
Kirtipur, Kathmandu, Nepal
1994

Master of Philosophy
Kathmandu University
Dhulikhel, Kavre, Nepal
2001

Submitted to the Faculty of the
Graduate College of the
Oklahoma State University
in partial fulfillment of
the requirements for
the Degree of
DOCTOR OF PHILOSOPHY
May, 2007

STUDY OF TISSUE TEMPERATURE DISTRIBUTION

DURING LASER-IMMUNOTHERAPY

FOR CANCER TREATMENT

Thesis Approved by:

James P. Wicksted

Chair of Advisory Committee

Wei R. Chen

Research Advisor

Kenneth E. Bartels

Member

Paul A. Westhaus

Member

Bret N. Flanders

Member

A. Gordon Emslie

Dean of the Graduate College

Dedicated to

My Late Father

Balkrishna U. Gnyawali

ACKNOWLEDGEMENTS

I would like to express my sincere gratitude to Dr. Wei R. Chen for continued support and guidance in completing this project. I would also like to express my sincere appreciation to Dr. James P. Wicksted for his kind support not only as my committee chair but also for a close guidance. I appreciate Dr. Kenneth E. Bartels who has been a part my small animal project. I am grateful to Dr. Paul Westhaus who supported me from the very beginning of my study not only in solving academic problems as a professor but also as a guardian. I am thankful to my wife Urmila S. Gnyawali for her incredible heart-felt support. My sons Bipul and Ankit are a part of my recreation after jaded day-long work. I would like to thank my research group especially Dr. Yichao Chen at University of Central Oklahoma and people from OMRF who provided the MRI facility and helped run the MRI experiments. This work was support in part by NIH INBRE. Finally, I would like to extend my sincere thanks to my advisory committee for its help bring the academic process in the end without which I would not have ever finished.

Surya C. Gnyawali

Department of Physics

Oklahoma State University

TABLE OF CONTENTS

LIST OF TABLES

LIST OF FIGURES

NOMENCLATURE

MCML	Monte Carlo Multilayer
MRI	Magnetic Resonance Imaging
MRT	Magnetic Resonance Thermometry
MRA	Magnetic Resonance Angiography
MRS	Magnetic Resonance Spectroscopy
IRT	Infrared Thermography
ICG	Indocyanine Green
GC	Glycated Chitosan
PTIT	Photothermal Immunotherapy
ppm	parts per million
CS	Chemical Shift
PRF	Proton Resonance Frequency
MHz	Megahertz
OMRF	Oklahoma Medical Research Foundation
CCD	Charged-Coupled Devices
MOS	Metal Oxide Semiconductor
PDT	Photodynamic Therapy
HbCO	Deoxy-hemoglobin
FLASH	Fast-Low-Angle-Shot
FOV	Field of View
ALA	5-aminolaevulinic acid
EMT6	epithelial-to-mesencymal transition

IM Intra Muscle

Basic Optical Parameters			Unit
μ_a	absorption coefficient		cm^{-1}
μ_s	scattering coefficient		cm^{-1}
μ_t	total attenuation coefficient	$\mu_t = \mu_a + \mu_s$	cm^{-1}
L(r, s)	radiance		$W/cm^2.sr$
$\varphi(r)$	fluence rate		W/cm^2

Dimensionless Parameters			
a	single particle albedo	$a = \mu_s/(\mu_a + \mu_s)$	
σ	screening coefficient		ppm

Chapter 1

General Introduction

1.1 Current Cancer Status

Cancer is a prevalent health problem of human beings. It is a disease that involves dynamic changes in the genome. It is characterized by uncontrolled growth and spread of abnormal cells. Its effective control may be expressed as "better prevention, early detection, and effective treatment". However, metastases and recurrence are the leading causes of treatment failure for cancer patients. More than a million new cancer cases in the U.S. are expected to be diagnosed in 2007. In addition, more than 1 million cases of basal cell and squamous cell carcinoma are expected to be diagnosed. About one in eight women in the United States develop breast cancer during her lifetime and more than 40,000 patients each year die of breast cancer. An estimate of 178,480 new breast cancer cases are expected in the U.S. in 2007 [1]. Deaths are due to tumors that metastasize despite local control.

1.2 Metastatic Tumors

Cancer cells break away from the primary tumor and enter the bloodstream or lymphatic system. This characteristic of a cancer to develop a secondary tumor is referred to as metastasis. Cancer cells can spread to any part of body; however lungs, bones, liver, and brain are the most common metastatic sites. Other metastatic tumors, such as

melanoma also pose a serious threat to human health. Metastases spread to multiple sites before detection of primary tumors. Statistics shows that 30% of patients with solid tumors already have metastasis, and another 10% of the patients will have developed clinically occult micro-metastases [2]. Metastasis is a major cause of cancer death through local invasion and metastasis to remote sites and vital organs.

1.3 Current Treatment Modalities

Many therapeutic methods have been developed for the treatment of benign or malignant tumors and include chemotherapy, radiation therapy, biological therapy, hormone therapy, neutron therapy, surgery and cryosurgery. However, most modalities are not effective for treating metastasis.

1.3.1 Chemotherapy and Its Effects

Chemotherapy is a tumor treatment using drugs that kill dividing cells. In this method there is a high risk of side effects in other parts of the body. There are different ways a chemotherapy dose may be administered to a patient, such as oral medication or intravenous injections. Because the drug being administered is often effective and is delivered to the dividing cells, it kills both tumor and non-tumor cells. Therefore, the treatment can actually be toxic. Reduction in the production of red blood cells by bone marrow, and reduction of white blood cells and immune suppression can result due to chemotherapy [1].

1.3.2 Radiation Therapy and Its Effects

Ionizing radiation can be used in the treatment of different types of cancers such as melanomas. Photons like x-rays, gamma rays, and particles like protons, neutrons, alpha particles are commonly used as sources of radiation. In this method, either high-

energy radiation may be targeted from radiation emitting device or radioactive materials may be implanted in the local area which emits the radiation and destroys the surrounding tumor mass. Testing errors also results in a high risk of killing surrounding healthy tissue. Radiation therapy is a local treatment and can not be usually used for the treatment of metastatic tumors. Radiation therapy has severe side effects; including fatigue, skin burn, cavity formation in teeth, memory loss, nausea and vomiting, immune suppression, and loss of fertility.

1.3.3 Photodynamic Therapy and Its Effects

Photodynamic therapy (PDT) is a modality for the treatment of tumors involving excitation of photosensitizers with low level light energy producing reactive oxygen species. The major biological effects of PDT are apoptosis (necrosis of tumor cells), inhibition of blood flow by stenosis (lyses preventing necessary nutrient supply) and deactivation of the immune system. Photodynamic therapy (PDT) uses a photosensitizing agent, and a particular wavelength of light. This light is able to excite the singlet state molecules of the agent into excited triplet state thereby the molecules either fluoresce or produce heat. When photosensitizers are exposed to a specific wavelength of light, they produce a form of singlet oxygen and/or other toxic radicals that kill nearby biological cells. Each molecule of photosensitizer is activated by a light of specific wavelength. The wavelength determines how far the light can travel into the tissue [3].

1.4 Laser Immunotherapy and Its Effects

Immunity is important in the control of tumor growth and spread. Host immune responses have been found associated with increased body temperature [4]. Recent experimental results have shown that hyperthermia can stimulate certain components of the immune response, leading to increased anti-tumor activity [5]. The immunity may also be potentiated by low dose immunoadjuvant. A number of studies have suggested possible benefits of hyperthermia to host defense mechanisms, such as improved in vitro proliferation of lymphocytes (spleen cells, thymus cells, bone marrow) at elevated temperatures [6, 7]. Laser irradiation of tumors provides an effective method of tumor destruction. Rapid tissue destruction is accompanied by elevation of the tissue temperature. Heat sensitivity of the tissue is lost at higher temperatures resulting in tumor and normal tissues destruction at the same rate.

1.5 Challenges in the Treatment of Metastatic Tumors

All existing treatment modalities have side effects, and none is totally effective for metastatic tumor treatment. For example, radiation therapy has been most commonly used in clinical trials and patient treatment. However, its side effects and its inability to treat metastasis is a challenge for optimal treatment outcome. Chemotherapy can be sometimes a first choice over radiation therapy and surgery for treating some cancers such as leukemia. Bone marrow suppression is the most challenging side effect of chemotherapy among many other conditions such as nausea and vomiting, diarrhea, fatigue, heart and lung damage, memory loss, liver, and kidney damage [1].

Photodynamic therapy is a new and promising treatment method for some specific cancers such as leukemia. It may also stimulate the host immune response [8]. However, it is also not free from side effects. The skin can become sensitive to light. This method is also effective for local tumor treatment along with the metastasis.

The successful treatment modality may be a combination of photothermal therapy coupled with optimal immune stimulation. Heat and some drugs can stimulate the immune response enabling the immune system to recognize foreign invading germs and cancerous cells. Therefore, optimal thermal treatment and immune stimulation may be required for the effective treatment.

1.6 Motivation

The above facts are motivation for the investigation of a method for precise measurement of temperature at the right location during the application of laser-immunotherapy so as to minimize damage to healthy surrounding tissue. The popularity of laser surgery has advanced over the past two decades. With the advancement of new, powerful and specific devices, the therapeutic applications have also been advancing steadily. Lasers can uniquely treat cutaneous pathology compared to others such as radiation therapy, chemotherapy, surgical or other medical modalities. As laser technology becomes more advanced, its role in treating disease should expand to provide better tools for clinical treatment.

The positive immune-stimulant effect of temperature-increase on the living system encourages the thermal treatment and thermal mapping as the tool for more accurate dose estimation. Essential laser parameters include laser, beam power, beam size,

and irradiation time. Small differences in any of these parameters can determine whether an application is efficacious or disastrous. These factors provide motivation for temperature mapping using MRI (3D mapping) and IR (surface mapping) for the laser-assisted dye-enhanced immune-stimulant cancer treatment modality.

1.7 Objectives

The long-term objective of this research is to develop a novel method using laser-immunotherapy for the treatment of soft tissue cancers such as breast cancer, skin cancer in combination with immunological stimulation. The goal is to study the effects of selective photothermal-tissue interaction using an 805-nm laser-wavelength and absorption enhancing dye indocyanine green (ICG) in combination with glycated chitosan (GC) as an immunoadjuvant in the treatment of metastatic tumors in rat and mouse models for ultimate application in human cancer treatment. The outcome from experimental animals can lead to applications in treatment of breast cancer and other soft tissue cancer in human being. This may also lead to potential use of treatment in other types of cancers such as melanoma and prostate cancers in human as well as in veterinary patients.

1.8 Necessity of Temperature Measurement

Selective photothermal-tissue interaction can destroy tumor cells directly by raising temperature of the target tissue using laser radiation. The optimum outcome of the laser photothermal interaction is to kill tumor target cells as effectively as possible and preserve the tumor proteins for immunological stimulation.

Temperature increase, combined with immunoadjuvants, also causes the immune activation by exposing tumor antigens [4]. Thus, the treatment effectiveness has a close

relationship with the thermal distribution inside the tumor and surrounding tissue. It has been shown that the temperature distribution due to laser irradiation is determined by both laser and tissue parameters [9]. Optical and thermal properties of tissue along with the tissue geometry contribute to the complicated heat diffusion pattern. Monitoring and controlling heat diffusion in terms of temperature play a significant role in obtaining optimal tumor treatment. However, determining the optical and thermal treatment parameters remains a challenge.

Continuous 3D-temperature measurement during laser treatment is possible using well established methods: magnetic resonance thermometry (MRT) and surface temperature measurement by infrared thermometry. Therefore, our focus is on temperature measurement using both volume and surface temperature measurement methods following the Monte Carlo simulation for light transport and the finite difference method with forward Euler integration of bio-heat diffusion equation.

The current study will also lead to understanding the relationship between temperature elevation and immune stimulation. Most cancer types such as basal cell carcinoma are developed underneath the skin. During treatment using lasers, the induced heat may cause skin-tissue damage. Therefore, it is necessary that surface temperature be measured and tissue damage be analyzed before onset of the treatment procedures. We have used an infrared thermal imaging technique to determine surface temperature patterns and the well established Arrhenius damage integral was used to study how temperature rise and tissue damage were related. This is intended to preserve the skin integrity even after laser-thermal treatment. We also want to study thermal-caused

immune stimulation which requires precise temperature measurement before, during, and after the treatment.

1.9 Organization of Research

This thesis is divided into six chapters. In the introductory chapter, general ideas about different types of cancers are introduced. This chapter also describes the status of current treatment modalities. The motivation of the work in which MRI and IR thermography guided cancer treatment is also briefly discussed.

Chapter two includes the Monte Carlo simulation of light transport and finite difference method for the solution of bio-heat diffusion equation. The simulation results of 2D-surface temperature distribution and 3D-volume temperature distribution are also given.

Chapter three focuses on the method of MRI 3-D temperature measurement. The temperature dependent susceptibility, susceptibility dependent chemical shift, and temperature dependent magnetic field are discussed. The determination of temperature distribution using MRI is discussed in this chapter.

Chapter four focuses on infrared thermography. In this chapter, we use an infrared camera for the measurement of changes in skin temperature profiles during laser treatment. The infrared thermometry discussion covers the heat radiation principles, detection of the radiation, and image formation technology that governs the thermal camera.

Chapter five describes the laser-immunotherapy using Glycated Chitosan (GC) as an immunoadjuvant and ICG as light absorption enhancing dye in the cancer treatment. The results are discussed.

Chapter six provides a summary of the work that interconnects the different approaches used in this study. A list of bibliography is provided. Finally, an appendix provides a list of simulation codes and image processing codes at the end.

Chapter 2

Monte Carlo Simulation of Laser-Tissue Interaction

2.1 Introduction

The laser has become an effective tool in surgical applications in medicine. Selective photothermal interaction in cancer treatment is one of the clinical uses of laser irradiation. Specifically, it has been shown that the combination of an 805-nm laser and *in situ* indocyanine green (ICG), a dye with an absorption peak around 800 nm, can result in selective heating when treating tumors buried in normal tissue [4-5, 12]. Recent studies using nanoparticles as *in situ* dye also have shown the selective photothermal effect [13]. Since tumor tissue is more sensitive to temperature elevation than normal tissue [7, 14], the control of temperature in the target region during laser irradiation is crucial to the outcome of the treatment.

Selective photothermal interaction can destroy tumor cells directly by raising the temperature of the target tissue. It can also serve as a precursor for immune activation by exposing tumor antigens, when combined with an immunotherapy [15, 16]. Tumor tissue responds to thermal change according to the treatment conditions. High-level thermal irradiation with extra-high temperature elevation can lead to total tissue destruction with potential denatured cells, which does not have much effect on the host immune stimulation. Low-level thermal irradiation may not destroy enough tumor

cells and may not expose enough tumor antigens. The optimal outcome of laser photothermal interaction is to kill as much target tumor as possible, and at the same time preserves tumor proteins for immunological stimulation. Such outcome depends on the temperature distribution in the tumor tissue.

The desired thermal effect strongly depends on the laser parameters, and the tissue optical and thermal properties. In the case of dye-enhanced laser therapy, dye administration also becomes crucial. The concentrations of absorbing dye and the optical and thermal properties of a specific target region are important factors. Improper dye administration causes undesired tissue damage or insufficient heating of target tissue. To choose treatment parameters properly and to predict the outcome of the photothermal effect, a reliable tissue model and simulation method is needed. Since biological tissue is a turbid medium and the mean free path of the light involved in irradiation is far less than the dimension of the medium, light propagation in tissue becomes a random process. The ideal mathematical tool for such a process is the Monte Carlo method [17-19]. The Monte Carlo method can effectively simulate absorption and scattering of the light in tissue, hence providing the spatial distribution of photon absorption. Heat transfer in the tissue during laser irradiation also affects temperature distribution and tissue responses in the target tissue and surrounding tissue. Using the absorbed energy in tissue as the heat source, thermal energy diffusion process can be determined, hence providing information on thermal responses of tissue. In this study, Monte Carlo simulation was used to acquire information of laser absorption in tissue, and the finite difference method for thermal diffusion in tissue was used to determine temperature distribution during and after laser

irradiation. In this study, the dynamic processes of tissue thermal responses to laser irradiation under different tissue configurations and laser parameters are reported.

2.2 Light-Tissue Interaction

2.2.1 Light Transport in Tissue

Laser tissue interaction is a process of light absorption and scattering in tissue. The most important parameter in the interaction is power density, φ (r, z) [W/cm^2] which is a function of power delivered and laser source spot size on the tissue,

$$\varphi_0(r,z) = \frac{P}{\pi r^2} \qquad (2.1)$$

where P [W] is laser input power and r [cm] is the radius of the spot, called spot size. The product of fluence and the absorption coefficient equals the heat source: the amount of energy deposited in a unit volume of tissue, $\dot{q}(r,z) = \varphi(r,z)\mu_a$. High irradiance corresponds to higher temperature. The depth of light penetration depends upon optical properties of tissue and laser wavelength. The wavelength from 600nm-1100nm can penetrate 5-10 millimeters through the tissue [12, 20]. As the laser beam propagates through the tissue, the intensity is attenuated exponentially due to absorption and scattering given by the Beer-Lambert law

$$\varphi\ (r,\ z)\ =\ \varphi_0\ e^{-\mu\ d\ (r,\ z)} \qquad (2.2)$$

The rate of heat generation per unit volume S(r, z) [W/cm^3] is $\dot{q}(r,\ z)\ =\ \mu_a\ \varphi(r,\ z)$. The propagation of scattered light is described by the light transport equation

$$(s\cdot\nabla)L(\vec{r},\hat{s}) = \frac{dL(\vec{r},\hat{s})}{ds} = -\mu_t L(\vec{r},\hat{s}) + \mu_s \int_{4\pi} p(\hat{s},\hat{s}')L(\vec{r},\hat{s}')\, d\omega' \qquad (2.3)$$

where $\mu_t = \mu_a + \mu_s$ is the attenuation coefficient, μ_a [cm^{-1}] is the absorption coefficient and μ_s [cm^{-1}] is the scattering coefficient. The left-hand side of the transport equation describes the rate of change of radiance $L(\vec{r},\hat{s})$ [$W/cm^2.sr$] at a point indicated by $\vec{r}(x,y,z)$ in the direction $\hat{s}$. The first term on the right-hand side is energy attenuated due to absorption and scattering. The minus sign in this term is due to the radiance decrease. The second term is the energy increase due to radiance from all other directions $\hat{s}'$ scattered into direction $\hat{s}$ about a solid angle $d\omega'$.

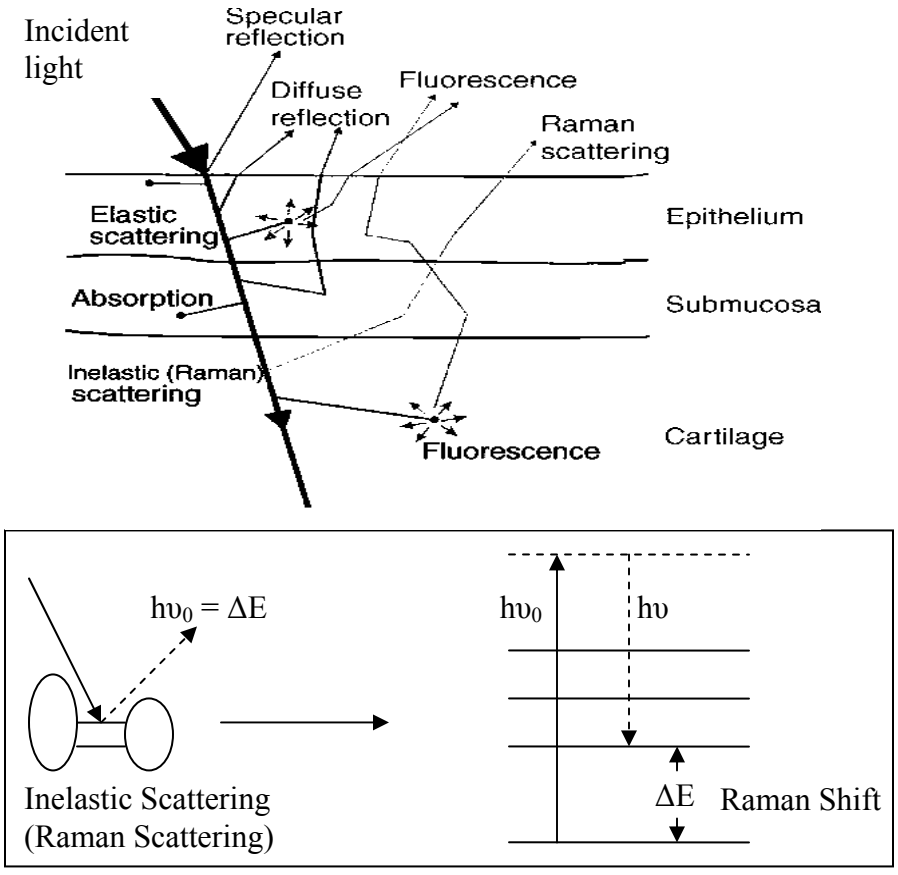

Figure 2.1 Pathways of light-tissue interaction. (a) light pathways (b) energy level diagram

The Phase Function

When light strikes a particle, it scatters. The angle at which the light is bent is a function of the size and shape of the particle as well as the wavelength of the incident light and the angle of incidence. In general, each particle has its own scattering profile and this scattering profile is called phase function or the probability density function. It is assumed that scattering by all particles may be described by a single phase function $p(\hat{s},\hat{s}')\,[\mathrm{sr}^{-1}]$ and it is not yet all related to the phase of the incident light. Scattering depends on the angle θ between $\hat{s}$ and $\hat{s}'$. Thus the phase function can be written as

$$\mathrm{p}(\hat{\mathrm{s}},\hat{\mathrm{s}}') = \mathrm{p}(\hat{\mathrm{s}}.\hat{\mathrm{s}}') = \mathrm{p}(\cos\theta) \qquad (2.4)$$

such that it satisfies the normalization condition

$$\int_{4\pi} \mathrm{p}(\hat{\mathrm{s}},\hat{\mathrm{s}}')\mathrm{d}\omega = 1 \qquad \text{where } \mathrm{d}\omega = \sin\theta\,\mathrm{d}\theta\,\mathrm{d}\varphi \qquad (2.5)$$

The simplest phase function is the isotropic phase function $p(\hat{s},\hat{s}') = 1/4\pi$. If the phase function is not isotropic, then a parameter called the average cosine of the phase function is used to describe the degree of anisotropy of the phase function. This parameter is often denoted by g and is defined as an integral over all angles of the phase function multiplied by the cosine of the angle

$$\mathrm{g} = \int_{4\pi} \mathrm{p}(\hat{\mathrm{s}},\hat{\mathrm{s}}')(\hat{\mathrm{s}}.\hat{\mathrm{s}}')\mathrm{d}\omega = 2\pi\int_{-1}^{1} \mathrm{p}(\cos\theta)\cos\theta\,\mathrm{d}(\cos\theta) \qquad (2.6)$$

The average cosine of the phase function g is a measure of how much light is scattered in the forward direction. For total forward scattering g = 1.00 and an isotropic scattering g = 0.00. For biological tissues in the range of infrared wavelength, g lies between 0.70-0.99 [9, 12, 20].

2.2.2 Thermal Diffusion

Generation of heat is due to deposition of photons and by excitation and de-excitation of molecules increasing the internal energy. In biological tissues the light absorbers are water, pigments, and tissue chromophores. In the visible and near-infrared range of wavelength melanin, lipofuscine, xantophyll, oxy- and deoxyhemoglobin are the main absorbers. Local absorption of photons creates local volumetric heat production, S(r,z) [W/cm^3] which is equal to the product of the local absorption coefficient and local fluence rate φ(r,z) [W/cm^2], $S(r,z) = \mu_a \varphi(r,z)$. The steady-state absorbed optical power density from a localized optical source can be expressed by [9, 12, 20]

$$S(r,z) = \dot{q}(r,z) = \mu_a \varphi(r,z) = \frac{P}{4\pi\delta^2 r} e^{-\frac{d(r,z)}{\delta}} \qquad (2.7)$$

where φ(r,z) is the steady-state fluence rate or power density [W/cm^2] , P is optical laser power [W], δ is the optical penetration depth $\delta = (3\mu_a[\mu_s(1-g)+\mu_a])^{-\frac{1}{2}}$ and r is the position from the axis of laser beam. At $\delta = d$, the heat generated is only 37% of the incident energy.

Heat Transfer

Heat in biological samples is mainly transferred due to conduction, convection, radiation, and blood perfusion. For a solid tumor, conduction dominates the other processes. Heat conduction requires a temperature gradient between two locations. The rate at which the temperature changes depends on the thermal diffusivity of tissue, $\alpha = \frac{k}{\rho\, c}$ [$cm^2\ s^{-1}$]. The rate of the temperature rise is governed by heat conduction in addition to the rate of volumetric heat production. These two rates are incorporated into the bioheat diffusion equation,

$$\nabla^2 T(r,\ z,\ t) + \frac{\dot{q}(r,\ z)}{k} = \frac{\rho\ c}{k}\frac{\partial T(r,\ z,\ t)}{\partial t}$$

$$\text{or} \qquad \nabla^2 T(r,\ z,\ t) + \frac{\mu_a \varphi(r,\ z)}{k} = \frac{\rho\ c}{k}\frac{\partial T(r,\ z,\ t)}{\partial t} \qquad (2.8a)$$

where $T(r,z,t)$ [^{0}C] is temperature field, k is thermal conductivity [W/cm^2.^{0}C], ρ is density [kg/cm^3] and c is specific heat [J/kg.^{0}C], and $\dot{q}(r,z)$ [W/cm^3] is the heat generated per unit volume per unit time [20, 21],

$$\dot{q}(r,z) \cong 3\mu_a\mu_s \frac{P}{4\pi\, r} e^{-\frac{d(r,z)}{\delta}} \qquad (2.9)$$

at a depth of $\delta = d$, $\dot{q}(r,z) \cong \frac{37\%\ \text{of}\ \mu_a\mu_s P}{4\pi\, r}$, assuming the scattering is very high compared to absorption and medium is isotropic. Using Laplacian in cylindrical

coordinates, Equation 2.8(a) becomes

$$\frac{1}{r}\frac{\partial}{\partial r}\left(r\frac{\partial T(r,\varphi,z,t)}{\partial r}\right)+\frac{1}{r^2}\frac{\partial^2 T(r,\varphi,z,t)}{\partial \varphi^2}+\frac{\partial^2 T(r,\varphi,z,t)}{\partial z^2}+\frac{\mu_a \varphi(r,z)}{k}=\frac{\rho c}{k}\frac{\partial T(r,\varphi,z,t)}{\partial t} \quad (2.8b).$$

For azimuthal symmetry, $T(r,\varphi,z,t)$ is invariant with ϕ. Therefore, the Equation 2.8(b) reduces to

$$\frac{1}{r}\frac{\partial}{\partial r}\left(r\frac{\partial T(r,z,t)}{\partial r}\right)+\frac{\partial^2 T(r,z,t)}{\partial z^2}+\frac{\mu_a \varphi(r,z)}{k}=\frac{\rho c}{k}\frac{\partial T(r,z,t)}{\partial t}$$

or
$$\frac{1}{r}\frac{\partial T(r,z,t)}{\partial r}+\frac{\partial^2 T(r,z,t)}{\partial r^2}+\frac{\partial^2 T(r,z,t)}{\partial z^2}+\frac{\mu_a \varphi(r,z)}{k}=\frac{\rho c}{k}\frac{\partial T(r,z,t)}{\partial t} \qquad (2.10)$$

This equation can be solved by using forward Euler time integration method, which is an explicit finite difference technique.

$$\frac{1}{r}\frac{\partial T(r,z,t)}{\partial r}=\frac{1}{i\Delta r}\frac{T^n_{i+1,j}-T^n_{i,j}}{\Delta r}, \qquad \frac{\partial^2 T(r,z,t)}{\partial r^2}=\frac{T^n_{i+1,j}-2T^n_{i,j}+T^n_{i-1,j}}{(\Delta r)^2}$$

$$\frac{\partial^2 T(r,z,t)}{\partial z^2}=\frac{T^n_{i,j+1}-2T^n_{i,j}+T^n_{i,j-1}}{(\Delta z)^2}, \qquad \frac{\partial T(r,z,t)}{\partial t}=\frac{T^{n+1}_{i,j}-T^n_{i,j}}{\Delta t}$$

Where, $i\Delta r = r$ and $i = 0, 1, 2, 3 \ldots$ is an integer represents the grid elements along r-axis and $j = 0, 1, 2, 3 \ldots$ along z-axis. When the above finite difference approximations are inserted into the Equation 2.10 for 3-D heat diffusion equation we get:

$$\frac{1}{i\,\Delta r}\frac{T^n_{i+1,j}-T^n_{i,j}}{\Delta r}+\frac{T^n_{i+1,j}-2T^n_{i,j}+T^n_{i-1,j}}{(\Delta r)^2}+\frac{T^n_{i,j+1}-2T^n_{i,j}+T^n_{i,j-1}}{(\Delta z)^2}+\frac{\dot{q}_{i,j}}{k}=\frac{\rho\, c}{k}\frac{T^{n+1}_{i,j}-T^n_{i,j}}{\Delta t}$$

Here, $T_{i,j}^{n}$ is an average of its neighboring temperatures, we have, $T_{i,j}^{n} \rightarrow \frac{T_{i+1,j}^{n} + T_{i-1,j}^{n}}{2}$

$$\frac{1}{i\,\Delta r}\frac{T_{i+1,j}^{n} - (T_{i+1,j}^{n} + T_{i-1,j}^{n})/2}{\Delta r} + \frac{T_{i+1,j}^{n} - 2T_{i,j}^{n} + T_{i-1,j}^{n}}{(\Delta r)^2} + \frac{T_{i,j+1}^{n} - 2T_{i,j}^{n} + T_{i,j-1}^{n}}{(\Delta z)^2} + \frac{\dot{q}_{i,j}}{k}$$
$$= \frac{\rho\, c}{k}\frac{T_{i,j}^{n+1} - T_{i,j}^{n}}{\Delta t}$$

$$\frac{1}{i\,\Delta r}\frac{T_{i+1,j}^{n} - T_{i-1,j}^{n}}{2\,\Delta r} + \frac{T_{i+1,j}^{n} - 2T_{i,j}^{n} + T_{i-1,j}^{n}}{(\Delta r)^2} + \frac{T_{i,j+1}^{n} - 2T_{i,j}^{n} + T_{i,j-1}^{n}}{(\Delta z)^2} + \frac{\dot{q}_{i,j}}{k} = \frac{\rho\, c}{k}\frac{T_{i,j}^{n+1} - T_{i,j}^{n}}{\Delta t} \qquad (2.11)$$

Solving Equation 2.11 for $T_{i,j}^{n+1}$ we get;

$$T_{i,j}^{n+1} = (1 - 2\frac{\alpha\,\Delta t}{(\Delta r)^2} - 2\frac{\alpha\,\Delta t}{(\Delta z)^2})T_{i,j}^{n} + \frac{\alpha\,\Delta t}{(\Delta r)^2}(1 + \frac{1}{2i})T_{i+1,j}^{n} + \frac{\alpha\,\Delta t}{(\Delta r)^2}(1 - \frac{1}{2i})T_{i-1,j}^{n}$$
$$+ \frac{\alpha\,\Delta t}{(\Delta z)^2}(T_{i,j+1}^{n} + T_{i,j-1}^{n}) + \frac{\alpha\,\Delta t}{k}\dot{q}_{i,j} \qquad (2.12)$$

with $F_{om} \equiv \frac{\alpha\,\Delta t}{(\Delta r)^2}$ defined as Fourier number, Equation 2.12 becomes

$$T_{i,j}^{n+1} = (1 - 4F_{om})T_{i,j}^{n} + (1 + \frac{1}{2i})F_{om}T_{i+1,j}^{n} + (1 - \frac{1}{2i})F_{om}T_{i-1,j}^{n} + F_{om}(T_{i,j+1}^{n} + T_{i,j-1}^{n}) + \frac{\alpha\,\Delta t}{k}\dot{q}_{i,j} \qquad (2.13)$$

Thus the Equation 2.13 is the solution of the Equation 2.8.

2.3 Methods of Simulation

2.3.1 Simulation of Volume Temperature Distribution

A cylindrical sample of radius 3cm and length 3cm was irradiated by laser light from above of the cylinder axially as shown in Figure 2.2. Laser rings carrying packets of photons propagate into the sample and are absorbed. The motion of these photons and their absorption is described by Monte Carlo method for light transport equation. As photons are absorbed, heat is generated locally. This heat dissipates all around the sample described by the bio-heat diffusion equation. The volume temperature distribution is obtained by Euler's Forward finite difference solution of the heat equation. The result of the solution is obtained as power density matrix and temperature matrix.

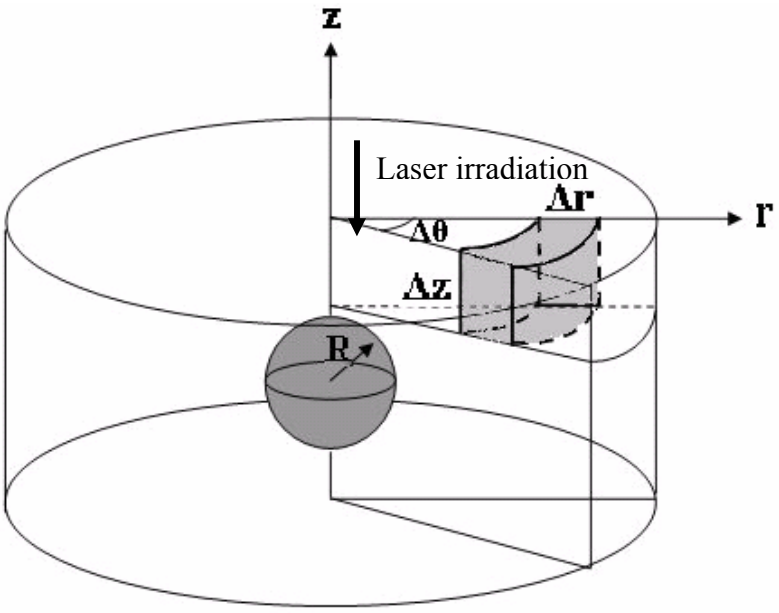

Figure 2.2 Tissue geometry used in the simulation. A 3 cm by 3 cm cylinder consisting of a spherical tumor of 0.5 cm radius at the center was irradiated by laser from above the cylinder. The optical properties used for get phantom were $\mu_a = 1.0\ cm^{-1}$, $\mu_s = 100\ cm^{-1}$ and $\mu_a = 0.01\ cm^{-1}$, where $\mu_{eff} = \mu_a + \mu_s$.

The optical and thermal properties used for the simulation purpose are as follows: thermal conductivity k = 0.0056 W/cm°C, specific heat capacity c = 3.4 J/g°C, and density ρ = 1.09 g/cm^3. A tumor with a radius of 0.5 cm was placed in the center with scattering coefficient of 100 cm^{-1} and an absorption coefficient of 4.8 cm^{-1}. The cross section is through the center of the cylinder with the laser beam incident from the top. The laser beam has a 0.25-cm radius with a power of 5.0 W. Both the top and bottom of the cylinder are subjected to natural convection with convection coefficient h = 0.000433 W/cm^2 ^{o}C. The simulation parameters are summarized in Tables 2.1 and 2.2.

Table 2.1. Tissue optical and thermal properties.

Symbol	Physical variable	Values used in this study	Units
μ_a	Absorption coefficient	0.01/4.0 for normal/dye enhanced tissue	cm^{-1}
μ_s	Scattering coefficient	100	cm^{-1}
n	Index of refraction	1.0 for both tissue types	n/a
g	Anisotropy factor	0.9	n/a
ρ	Density	1.09	g.cm^{-3}
k	Thermal conductivity	0.0054	W/cm.^{0}C
c	Specific heat	3.4	J/g.^{0}C
h	Convection coefficient	0.000433	W/cm^2.^{0}C

Table 2.2. Laser beam parameters and tissue geometry.

Symbol	Physical variables	Values used in this study	Units
P	Power	2.0-5.0	W
r	Beam radius	0.25-1.5	cm
n	Number of rings	10-100	n/a
n_p	Number of photons	10^5	n/a
dr	Radial space increment	0.01	cm
dz	Axial depth increment	0.01	cm
n_r	Number of radial divisions	100	n/a
n_z	Number of axial depth divisions	100	n/a
n_a	Number of angular division	30	n/a
n_l	Number of layers	3	n/a
d	Depth of spherical layer	0.5	cm
R	Radius of spherical layer	0.5	cm

2.3.2 Simulation of Surface Temperature Distribution

Volume temperature simulation program was developed earlier using Monte Carlo finite difference method [9]. The modified version of the same program was used to simulate the surface temperature. The temperature field T(r, z, t) becomes T(r, 2, t) for surface geometry at z = 2 mm from the surface. The radial heat is assumed to dissipate around the target with time. The top boundary of the surface is subjected to convection, which follows a Neumann boundary condition. The convection condition at the top of the cylinder is given by,

$$-k\frac{\partial T}{\partial z} = h(T_b - T_\infty)$$

The left side of this boundary condition becomes zero where dT approaches zero. In this case, $T_b = T_\infty$. Also as r approaches zero following a radial path, the slope of the temperature field vanishes so that

$$-k\frac{\partial T}{\partial r} = 0$$

The coordinate system of the simulation is user-defined radius r with thickness z assumed to be constant. In our simulation, the surface thickness was taken as 2 mm. Energy deposition was accounted using Monte Carlo simulation of photon transport and the finite difference method is used for the determination of heat and temperature distribution. A flat circular beam was used. In this simulation, the flat incident beam is constructed of multiple concentric rings. Each ring consists of an equally weighted number of photons to produce an isotropic incident beam. For a desired beam radius, the number of rings may be increased to approach a continuum of incident energy. A total of 100,000 photons were used in each of the simulations in this study. Tissue optical and

thermal properties, laser beam parameters, and tissue configurations used in this simulation are based on previous studies which are experimentally measured values for gel phantoms and mice tissue [19].

2.4 Results

2.4.1 Simulation of Volume Temperature Distribution

The photon absorption power density matrix obtained by the Monte Carlo simulation for a cylinder of 3.0-cm radius and 3.0-cm height is shown in Figure 2.3. A tumor with a radius of 0.5 cm was placed in the center with an absorption coefficient of 1.0 cm^{-1} and scattering coefficient of 100 cm^{-1}. Due to symmetry, only half of the cylinder cut axially is shown in Figure 2.3(a). The laser beam incidents from the top through the center of the cylinder with a cross section shown. The laser beam has a 0.5 cm radius and a power of 1.7 W incidents normally on the tumor. The color scale bar in Figure 2.3 (a) represents the amount of power absorbed by the target. Temperature profiles at the center of the cylinder T(r, z, t) at different depths and different time points during and after laser irradiation are depicted in Figure 2.3 (b). Both the top and bottom of the cylinder are subjected to natural convection. The gray curve represents the temperature at the surface, the thick solid curve represents the temperature in the middle (1.5 cm below the surface, with dye enhancement that increases the absorption from 0.01 to 10 cm^{-1}), and the thin solid blue curve represents the temperature at the bottom (3 cm below the surface), Figure 2.3 (b). Temperature distribution at different time intervals during and after laser irradiation are shown in Figure 2.3 c(1-8). The cross sections are through the center of the cylinder and only half of the cylinder is shown as follows: (1) 10 s after onset of the laser irradiation, and (2) through (8) 200s to 1400 s, with a 200 s increment, after the start of the laser irradiation.

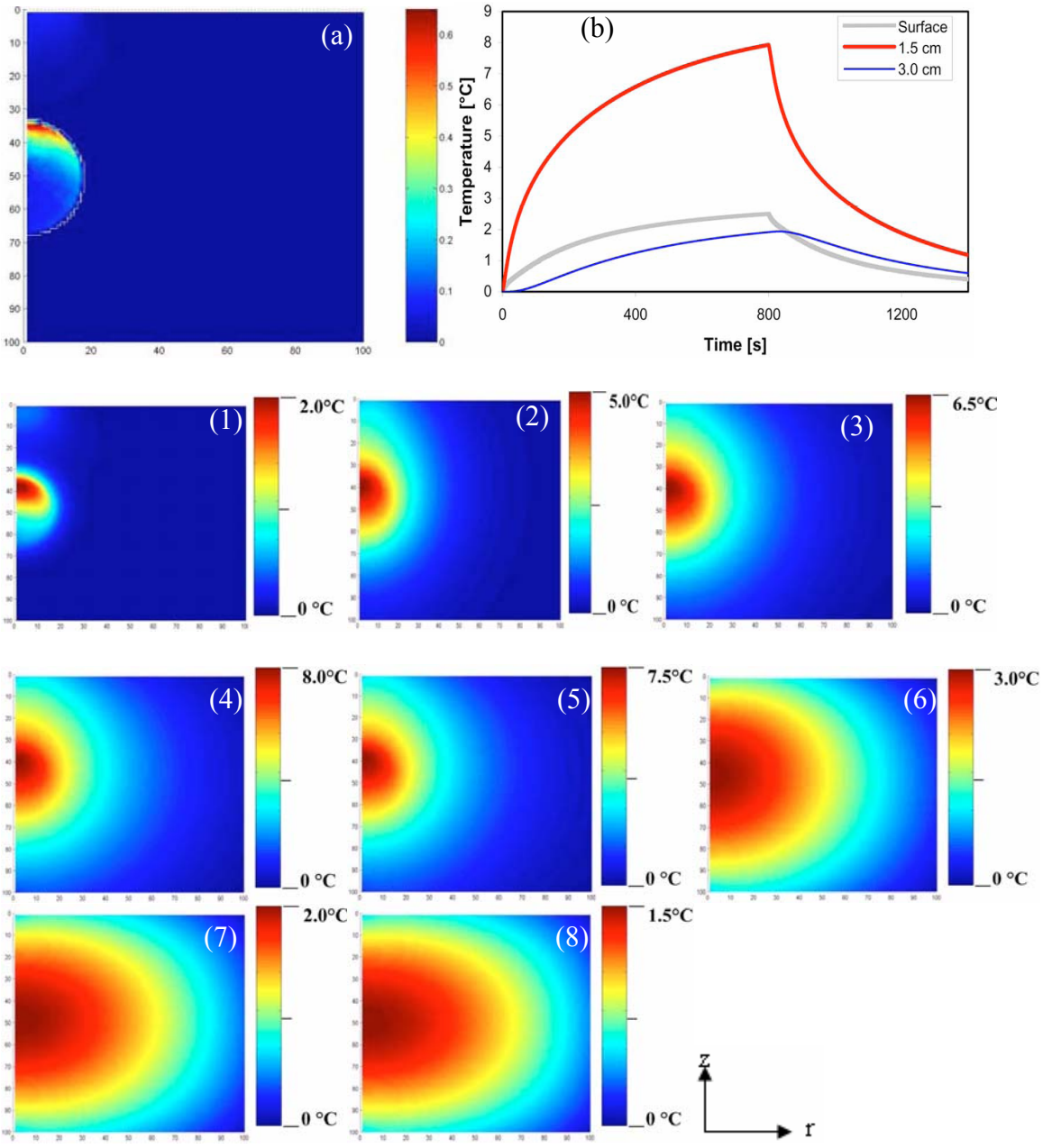

Figure 2.3 (a) Photon absorption power density matrix obtained by the Monte Carlo simulation for a cylinder of 3.0-cm radius and 3.0-cm height. A tumor with a radius of 0.5 cm was placed in the center with an absorption coefficient of 1.0 cm^{-1}. The cross section is through the center of the cylinder with the laser beam incident from the top. The laser beam has a 0.5-cm radius with a power of 1.7 W. The irradiation time is 800 s. The scale bar represents power absorbed by the region in W/cm^2. (b) Temperature profiles at the center of the cylinder *T(r, z, t)* at different depths and different time points during and after laser

irradiation. Both the top and bottom of the cylinder have natural convection. The gray curve represents the temperature at the surface, the thick solid curve represents the temperature in the middle (1.5 cm below the surface, with dye enhancement), and the thin solid curve represents the temperature at the bottom (3 cm below the surface). (c) Temperature distributions at different time frames during and after laser irradiation. The cross sections are through the center of the cylinder and only half of the cylinder is shown here: (1) 10 s after the starting of the laser irradiation, and (2) through (8) 200s to 1400 s, with a 200s increment, after the start of the laser irradiation

2.4.2 Simulation of Surface Temperature Distribution

A slice cut axially from the cylinder was taken as input data, Figure 2.3 (a). A row matrix of dimension 1 x 51 at a depth of z = 2 mm from the power density matrix (the line in image of Figure 2.3(a)) was used. Radial temperature distribution was generated as a function of angle that varies from 0 radians to 2π radians. Each element of the row matrix was taken as radius of the concentric circles. By writing a matlab code (see appendix C) that generates the isotherms of the input data. The result so obtained was plotted to obtain a surface varying color pattern as shown in the Fig.2.4 (b).

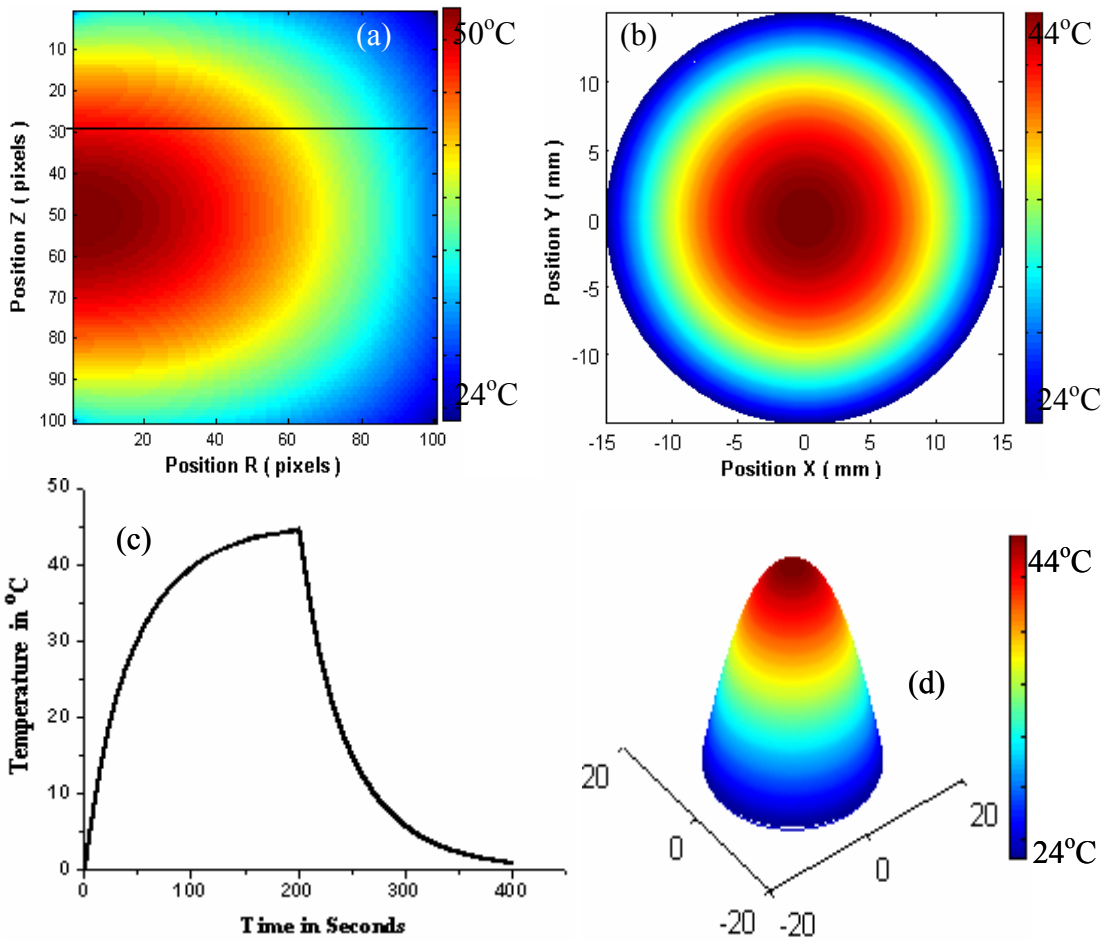

Figure 2.4 (a) Photon absorption power density matrix obtained by Monte Carlo simulation of volume temperature distribution on a cylinder of 3.0-cm radius and 3.0-cm height. A tumor with a radius of 0.5-cm was placed in the center with an absorption coefficient 0.10-cm^{-1}. Due to symmetry, only half of the cylinder is shown. The cross section is through the center of the cylinder with the laser beam from the top. The laser beam has a 0.25-cm radius with a power of 5.0 W. The irradiation time is 200 s. The scale bar represents the temperature corresponding to the power density. (b) Radial surface temperature increment in a phantom. Axes x and y represent the variation of radial position starting from center of cylinder axis as the center of the rings. Concentric rings of same temperature are indicated by color bar. The central temperature is the maximum temperature. (c) Temperature profile at the center of cylinder at different time points during and after the laser irradiation. Both top and bottom of the cylinder are subject to natural convection. (d) A 3D-plot representing the radial surface temperature increase.

2.5 Discussion and Conclusion

Simulation of volume temperature distribution using a cylindrical semi-infinite geometry may be used to investigate the effect of boundary conditions and tissue geometry. The photon absorption property of target tissue is enhanced by increasing the absorption coefficient. Hence, the tumor can be heated to a desired temperature without damaging the surrounding tissue. This information can be easily obtained from the simulation results of Figure 2.3 and 2.4. As shown in Figure 2.3, the dye enhanced part (assumed absorption enhancement with ICG) of the cylinder depicts higher temperature than the upper and lower layers. The temperature field T(r, z, t) is a function of time and space. Figure 2.3 c(1-8) are temporal temperature patterns. The temperature increases exponentially with time, it saturates, and drops off exponentially (Figure 2.3(b)) after the laser is turned off. As illustrated in Figure 2.3 (b), the layer at a depth of 1.5 cm is heated much more than the upper and lower layers, due to the absorption enhancement.

Surface simulation in Figure 2.4 shows that the temperature increases at the beam center is highest and the temperature decreases with the increase in radial position. The results clearly show the treatment method is noninvasive and selective. The choice of dye and its concentration is important for an optimal treatment outcome. However, the unavailability of blood perfusion in the simulation algorithm to account for the blood vessels and capillaries in the tumor limits the accuracy of temperature measurement. It is very important that the blood circulation prevents the excessive heating of the target experiments. The simulation method, therefore, remains incomplete unless the blood vessels and capillaries are included in the algorithm. Our model does not include vessel

geometry and corresponding boundary conditions which are required in the simulation algorithm for the further preciseness of the temperature measurement. The blood perfusion can be incorporated by designing different layers of tissue with different refractive indices in the algorithm. Limitation of finite difference method (FDM) occurs when the tissue within its boundaries is heterogeneous or has irregular geometry such as blood vessels and lipid layers. Our model doesn't incorporate photon scattering in skin. Also it doesn't incorporate changes in optical and thermal properties of the tissue due to temperature increase. The temperature gradient in the skin tissue induces water transport from deeper layers to surface which may have a significant effect on heat transfer and light absorption coefficient. Finite element method (FEM) is suitable for solving such problems because this method considers a number of nodes in the tissue geometry and the heat diffusion equation is solved with a polynomial equation for each node, which can be a future interest.

Chapter 3

Magnetic Resonance Thermometry (MRT)

3.1 Introduction

Mapping internal temperature with a minimally invasive procedure has clinical relevance. The body temperature is closely related to physiological function. A normal blood supply warms tissue and infected tissue is at higher temperature. Measurement of internal body temperature by a non-invasive method enables the diagnosis of pathology of disease beneath the body surface and helps treat many types of diseases such as cancer through thermal ablation, and hyperthermia. MRI can be an ideal solution, because it allows for three-dimensional images with high spatial and temporal resolution. Furthermore, as MRI does not use ionizing radiation, it does not cause any harm to the patient [22, 23]. In tumor thermal therapy, MRI provides good visualization of tumors in different parts of the body. The idea behind the image-guided thermal therapy is to deposit heat energy into a prelocalized diseased tissue volume and induce necrosis while avoiding the destruction of surrounding healthy tissue. MR imaging method has been used for both diagnostic and therapeutic purposes. Hindman in his research paper [24] reported the proton resonance shift of water to be 0.01 ppm per ^{o}C which is very useful in calculating temperature from MR phase-images. Saher et al, [25] used magnetic resonance thermography (MRT) on a laser-induced heating in an ocular phantom

utilizing the property of temperature dependent phase changes in proton resonance frequency. Young et al [26] have developed models for temperature dependent T_1-based in vivo studies using MRI. Rieke et al [27] reported referenceless proton resonance frequency (PRF) shift minimally invasive thermometry. Ishihara et al [22] studied the effect of phase and chemical shift on temperature change using MRI chemical shift method. Those studies motivated us in the MRI temperature measurement during dye-enhanced immune stimulated laser tumor treatment.

We used laser irradiation in tumor treatment along with dye-enhancement. This method provides a non-invasive treatment modality that minimizes surrounding tissue damage. Temperature is a crucial factor in this non-invasive study. Magnetic Resonance imaging method enables us to determine temperature distribution non-invasively. However, magnetic susceptibility-related errors cause significant deviations in the temperature measurement. Present studies have used the diamagnetic susceptibility-related pure water shielding coefficient, ignoring the abundant paramagnetic materials such as Fe^{2+}, Fe^{3+} and other ions present in the tissue. Those susceptibilities contribute higher temperature dependency in the chemical shift and hence on applied magnetic field [28]. This can not be ignored to get better information in MRI-guided studies.

3.2 Magnetic Resonance Imaging (MRI)

Each proton in the nucleus has a magnetic moment. In most nuclei, the particles are paired so that the net magnetic moment is zero. However, if the numbers of protons or neutrons are odd, the magnetic moments do not cancel completely. Nuclei with an unpaired proton or neutron such as ^{1}H, ^{13}C, ^{19}F and ^{31}P, among others, possesses a net

magnetic effect when they are placed in an external magnetic field. The ^{1}H nucleus, which is highly abundant in biological systems, has the strongest magnetic moment. Since the individual magnetic moments are randomly oriented, biological tissue does not normally exhibit a net magnetization. However, if biological tissues are placed in an external magnetic field, they show a net magnetization. This property is exploited in magnetic resonance imaging and spectroscopy.

The magnetic moment of the proton nucleus **μ** and an angular momentum **J** are parallel to each other,

$$\vec{\mu} = \gamma \hbar \vec{J} \tag{3.1}$$

The constant γ = gyromagnetic ratio, J = nuclear angular momentum quantized in the units of $\hbar$. The energy of interaction with the applied magnetic field $\vec{B}_a = B_0 \vec{z}$ along z-axis is

$$U = -\vec{\mu} \cdot \vec{B}_a = -\gamma \hbar B_0 J_z \tag{3.2}$$

where the allowed values of J_z are $m_J = +J \; to \; -J$ and for proton $m_J = \pm \frac{1}{2}$

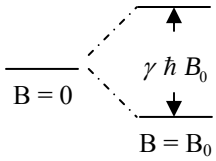

Figure 3.1 Energy level splitting of a hydrogen nucleus spin J = ½ in a static magnetic field B_0

In a magnetic field, a nucleus with m_J = + ½ and - ½ has two energy states $|J, m_J\rangle \rightarrow \left|\frac{1}{2}, \pm\frac{1}{2}\right\rangle$ as in Figure 3.1. The energy difference is $\hbar\,\omega_0 = \gamma\,\hbar\,B_0$ or

$$\omega_0 = \gamma\, B_0 \qquad (3.3)$$

This Equation 3.3 is the fundamental condition for magnetic resonance absorption and reemission. For proton $\gamma = 2.675\times10^8\ s^{-1}T^{-1}$ [29] and therefore, for $B_0 = 1\ tesla$, $\omega_0 = 2.675\times10^8\ s^{-1}$ and the frequency of precession or Larmor frequency

$$f_0(MHz) = \frac{2.675\times10^8\ s^{-1}}{2\pi} = 42.58\ B_0(tesla) \qquad (3.4)$$

The torque on a magnetic moment **μ** in a magnetic field **B** causes the magnetic moments to precess around main magnetic field. The torque $\vec{\mu}\times\vec{B}$ is equal to the rate of change of angular momentum of the nucleus. So that the equations of motion are

$$\frac{\hbar\, d\vec{J}}{dt} = \vec{\mu}\times\vec{B}_a \text{ Or } \frac{d\vec{\mu}}{dt} = \gamma\ \vec{\mu}\times\vec{B}_a \qquad (3.5)$$

Therefore, the magnetic moment precesses. The net nuclear magnetization **M** is the ensemble averaged sum of all magnetic moments in a unit volume.

$$\vec{M} = \sum \vec{\mu}_i \qquad (3.6)$$

So that Equation 3.5 becomes

$$\frac{d\vec{M}}{dt} = \gamma\ \vec{M}\times\vec{B}_a \qquad (3.7)$$

with the applied magnetic field along z-axis, $\vec{B}_a = B_0\ \hat{z}$. At thermal equilibrium at temperature T, the magnetization will also be along $\hat{z}$, so that the components of the nuclear magnetization are:

$$M_x = 0\ ,\ M_y = 0\ ,\ and\ M_z = M_0 = \chi_m\ B_0 \qquad (3.8)$$

The magnetization of a system of spins with J = ½ is related to the population difference N_1-N_2 of the lower and upper levels in Figure 3.1:

$$M_z = (N_1 - N_2)\mu \qquad (3.9)$$

where N_1 and N_2 are the populations of lower and upper levels per unit volume respectively and $N = N_1 + N_2$ is the total number of atoms. The equilibrium populations of the two levels with $x = \frac{\mu B_0}{K_B T}$ and Boltzman factor exp(K_BT) where K_B = Boltzman constant and T = absolute temperature, are:

$$N_1 = \frac{N\ e^x}{e^x + e^{-x}} \qquad for\ J = +1/2$$

$$N_2 = \frac{N\ e^{-x}}{e^x + e^{-x}} \qquad for\ J = -1/2 \qquad (3.10)$$

The resultant magnetization for N number of atoms per unit volume from Equation 3.9 and Equation 3.10 is,

$$M = \mu\ N\frac{e^x - e^{-x}}{e^x + e^{-x}} = N\mu\ \tanh\left(\frac{\mu\ B_0}{K_B T}\right)\ \cong N\mu\frac{\mu\ B_0}{3K_B T}\ \ for\ \frac{\mu\ B_0}{K_B T} << 1 \quad (3.11)$$

3.3 Magnetic Resonance Thermometry (MRT)

Equation 3.11 shows the dependence of nuclear magnetization M with temperature T. That means the change in temperature of sample changes magnetization. In laser-tumor treatment, the tumor temperature raises. Therefore, taking the case of high temperature on Equation 3.11 we have,

$$M = N\mu \frac{\mu B_0}{3K_B T} = \left(\frac{N \mu^2}{3K_B}\right) \quad \frac{B_0}{T} = \frac{CB_0}{T} \tag{3.12}$$

where $C = \frac{n\mu^2}{3K_B}$ is so called Curie constant [30].

Now the paramagnetic susceptibility (magnetizability), χ_p is defined by

$$M = \chi_p B \tag{3.13}$$

From Equation 3.12 and Equation 3.13

$$\chi_p(T) = \frac{n\mu^2}{3K_B T} = \frac{C}{T} \tag{3.14}$$

From Equation 3.14 for a system of magnetic moments the susceptibility is dependent on temperature.

3.3.1 Chemical Shift

When an atom or a molecule is placed in an external magnetic field, orbital currents are induced in the electron clouds which surround the nucleus of interest. These

currents give rise to a small magnetic field which causes a modification in applied magnetic field. Chemical shift originates due to the modifications in local magnetic field experienced by a nucleus in an atom or a molecule as a result of such induced magnetic fields. These changes in local field affect the resonant frequency of the nuclei at different position of sample. A nucleus, in this case, is said to be shielded or particularly screened from the external field by the electron cloud. The variations in nuclear shielding are mainly due to variation in local electron density and special shielding effects produced by molecules and structures that force electrons to circulate only certain preferred directions. An external magnetic field can induce diamagnetic or paramagnetic currents in which one is opposite to the other in direction. The diamagnetic current induces a magnetic field that opposes the applied field, where as paramagnetic current induces a magnetic field which augments the applied field. Pure water is a diamagnetic material, in which the magnetic susceptibility is a complex function of temperature [31].

Water is the major component of animal tissue. The induced current increases as the water temperature increases. Therefore, the molecular screening of the water molecules becomes more effective as the temperature increases. This results in an increase in chemical shift of water proton which causes local field to decrease. The variation of local magnetic field with temperature is also determined by the temperature dependence of magnetic susceptibility. Thus the total susceptibility is the sum of susceptibility of pure water and paramagnetic compounds as well as ions in water [28]. In addition to water protons, animal tissue contains ions such as Ca^{2+}, Fe^{2+} and Fe^{3+} attached to the protein molecules like hemoglobin. Those are paramagnetic materials. Thus, the

total susceptibility is the sum of susceptibilities of water and the paramagnetic ions present

$$\chi_{tot} = \chi_w(T) + \sum_i \chi_{p,i}(T) = \chi_w(T) + \sum_i \frac{C_{p,i}}{T} \qquad (3.15)$$

where $C_{p,i}$ is the Curie constant for i species [31]. A relation between magnetizability and magnetic shielding for molecular system has been developed by Janowski and Wonlinski [32].

$$\sigma(\mathrm{T}) = -\frac{2}{3}\mu_0 \{\chi_w(T) + \sum_i \chi_{p,i}(T)\}$$

From Taylor expansion of both diamagnetic and paramagnetic susceptibilities,

$$\sigma(\mathrm{T}) = -\frac{2}{3}\mu_0 \{\chi_w(T_0) + (T-T_0)\frac{\partial \chi_w}{\partial T}\Big|_{T_0} + \ldots + \chi_p(T_0) + (T-T_0)\frac{\partial \chi_w}{\partial T}\Big|_{T_0} + \ldots\}$$

$$\sigma(\mathrm{T}) \cong -\frac{2}{3}\mu_0 \{\chi_w(T_0) + \chi_p(T_0) + (T-T_0)\frac{\partial \chi_w}{\partial T}\Big|_{T_0} + (T-T_0)\frac{\partial \chi_w}{\partial T}\Big|_{T_0}\}$$

$$\sigma(\mathrm{T}) \cong Cons\tan t + (T-T_0)\{-\frac{2}{3}\mu_0 \frac{\partial \chi_w}{\partial T}\Big|_{T_0}\} + (T-T_0)\frac{2}{3}\frac{\mu_0 C}{T_0^2}$$

$$\sigma(\mathrm{T}) \cong Cons\tan t + (T-T_0)\alpha_{dia} + (T-T_0)\alpha_p$$

$$\sigma(\mathrm{T_f}) - \sigma(\mathrm{T_i}) = (T_f - T_i)\alpha_{dia} + (T_f - T_i)\alpha_p \qquad (3.16)$$

where $\mu_0 = 4\pi \times 10^{-7} N/A^2$ is the permeability of vacuum.

It is known that the electron current due to surrounding orbital electrons on an individual proton (Figure 3.2) induces local magnetic field **B**, a susceptibility effect [31-33], which is a function of temperature T (^{0}C) via the shielding coefficient of the molecules σ(T) (ppm), which depends on the strength of applied magnetic field B_0 (tesla) of the MR scanner.

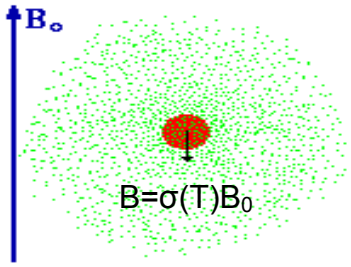

Figure 3.2 The extra magnetic field generated by local electron cloud. This local field varies with tissue composition causing the applied magnetic field B_0 to vary from position to position and hence the signal picked up by the receiver rf coil becomes different at different positions on the sample. This is an advantage in the image contrast.

Paramagnetic materials with positive susceptibility have the negative screening coefficient and diamagnetic materials with negative susceptibility have positive screening coefficient.. In both cases, the total magnetic field can be modeled as [34-43]

$$B_{loc}(T) = B_0 - \sigma(T)B_0 \qquad (3.17)$$

The chemical shift describes the dependence of nuclear magnetic energy levels on the electron environment on a molecule. In other words chemical shift is a separation of resonance frequencies from a reference frequency due to local field inhomogeneities. The

field inhomogeneity is due to the small secondary magnetic field generated by the current of surrounding electron cloud, Figure 3.2. As a result of shielding, Equation 3.3 becomes,

$$\omega(T) = \gamma\, B_{loc} = \gamma\, B_0 \{1 - \sigma(T)\} \qquad (3.18)$$

That means, the resonance frequency of the nucleus in an atom is slightly lower than that of bare nucleus (Figure 3.3). Similar effects occur for nuclei of molecules. However, in molecules the motion of the electrons in molecular environment is complicated. Therefore, the external field may be increased or decreased depending on the sign of susceptibility. Thus the resonance frequency of the nucleus is the characteristic of the environment.

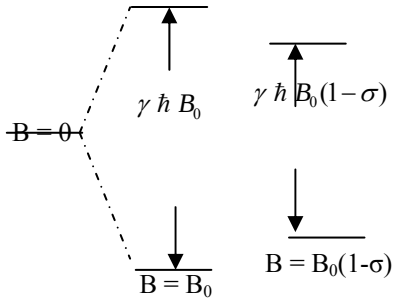

Figure 3.3 The energy levels of a ^{1}H in a screened magnetic field. The splitting of the energy level decreases the emitted energy as the proton is in the molecular environment thereby reducing the resonance frequency of the proton.

In MR imaging experiment, gradient echo pulse sequence is used to obtain phase images with high spatial and temporal resolution.

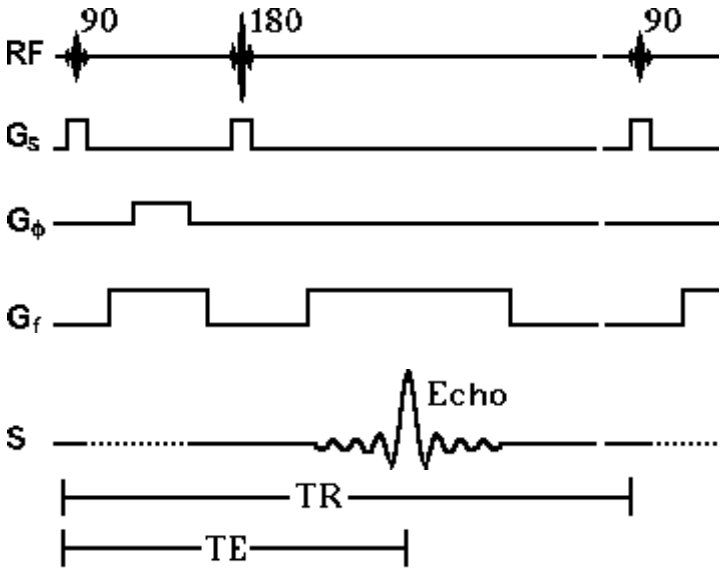

Figure 3.4 The timing diagram for a spin-echo imaging sequence has entries for the RF pulses, the gradients in the magnetic field, and the signal. G_s = slice selection field, G_φ = phase encoding field, G_f = frequency encoding field, S = output signal, TR = rf input signal repetition time, TE = echo time.

The frequency shift corresponds to a temperature dependent phase with the echo time T_E of a gradient echo sequence,

$$\Phi(T) = \omega(T)\, T_E \tag{3.19}$$

The phase is monitored using phase images of gradient echo sequence. At the initial temperature T_i, the phase is $\Phi(T_i)$ and when the temperature is changed to T_f, the phase is $\Phi(T_f)$. Thus the phase difference is

$$\Delta\Phi = \Phi(T_f) - \Phi(T_i) \tag{3.20}$$

And therefore, from Equation 3.18, Equation 3.19 and Equation 3.20

$$\Delta\Phi = T_E\{\omega(T_f) - \omega(T_i)\} = T_E \gamma\, B_0\{\sigma(T_f) - \sigma(T_i)\} \tag{3.21}$$

Also from Equations 3.16 and 3.21

$$\Delta\Phi = T_E \gamma\, B_0[(T_f - T_i)\alpha_{dia} + (T_f - T_i)\alpha_p] = T_E \gamma\, B_0(\alpha_{dia} + \alpha_p)\Delta T \tag{3.22}$$

Finally, from Equation 3.22,

$$\Delta T = \frac{\Delta\Phi}{\gamma\,(\alpha_{dia} + \alpha_p)\,T_E B_0} = \frac{\Delta\Phi}{f} = \Delta\Phi * F \qquad (3.23)$$

where $F = 1/f = 1/\,(\alpha_{dia} + \alpha_p)\,\gamma T_E B_0 = 1/(\gamma\, T_E B_0 (\alpha_{total}))$

Here we have calculated the temperature change due to contribution from paramagnetic components of tissue:

$$\alpha_p = \frac{2\mu_0 C}{3T_0^2} = \frac{2\mu_0 n\mu_p^2}{3T_0^2 \times 3K_B} = \frac{2\mu_0\mu_p^2}{9T_0^2 K_B}\left(\frac{N}{V}\right) = \frac{2\mu_0\mu_p^2}{9T_0^2 K_B}\left(\frac{M/V}{m}\right) = \frac{2\mu_0\mu_p^2}{9T_0^2 K_B}\left(\frac{\rho_{Fe}}{m_{H\,b}}\right) \qquad (3.24)$$

This is the first derivative of Equation 3.17 with respect to temperature change; it is referred to as paramagnetic contribution to chemical shift caused by the temperature change in the sample. Assuming the paramagnetic contribution is mainly from iron present in the blood in the form of hemoglobin (Hb), the number density becomes the mass density of Fe per mass of hemoglobin molecules. Upon substitution the values of the parameters $\mu_{Hb} = 1.298 \times 10^{-23}\ (J/T)$ [46], $m_{Hb} = 64500 \times 1.67 \times 10^{-27}\ (kg)$, $\rho_{Fe} = 7850\ (kg/m^3)$ at temperature $T = 300\ K$ in Equation 3.26, the calculation is as follows:

$$\alpha_p = \frac{2 \times 4\pi \times 10^{-7}\,(N/A^2) \times \{1.298 \times 10^{-23}\,(J/T)\}^2}{9 \times \{300(K)\}^2 \times 1.38 \times 10^{-23}\,(Nm/K)} \frac{\{7850(kg/m^3)\}}{64500 \times 1.67 \times 10^{-27}\,(kg)}$$
$$= 0.00276 \times 10^{-6}\,K^{-1}$$
$$= 0.00276\ (ppm/K)$$

This is the contribution from paramagnetic component of tissue to chemical shift. From the value $\alpha_p = 0.00276(ppm/K)$, it is clear that the effect of 1^0C rise in temperature on the phase change is only 0.01276 ppm. This means, even very small fluctuations in

magnetic field $\mathbf{B_0}$ in the order of 0.01276 ppm can cause phase change resulting in a significantly higher temperature change of 1 ^{0}C.

The diamagnetic contribution is mainly from water, which is experimentally determined to be 0.01 ppm / ^{o}C by Hindman [35-45]. Assuming tissue has both diamagnetic water and paramagnetic component,

$$\alpha_{\text{total}} = \alpha_{\text{dia}} + \alpha_{\text{p}} = 0.01\,ppm/K + 0.00276\,ppm/K = 0.01276\,ppm/K \qquad (3.25)$$

The total temperature change is the sum of contributions from diamagnetic and paramagnetic components of the tissue sample in consideration which can be calculated using Equation 3.23. The difference in phase-image after heating and the baseline phase-image provides the phase change to account the temperature increase. This explains the temperature sensitivity of chemical shift which is caused by the inhomogeneity in the external magnetic field due to the electronic environment of the nucleus.

3.4 Materials and Methods

3.4.1 Phantom Sample Preparation

Gelatin phantoms were used in this experiment to simulate biological tissue. The ICG-mixed gel was used to simulate absorption-enhanced target for selective photothermal interaction. Both target and non-target phantom specimens were prepared by mixing 76 ml of water in 20 ml of lyposin and 4 gm of gelatin. After mixing, the gel specimen was allowed to solidify at 4^{0}C. Target phantoms were prepared by solidifying the homogeneous target gel admixed with ICG solution. A spherical solid gel phantom with dye was buried in the non-target gel.

3.4.2 Dye Enhancement

Indocyanine Green (ICG) (Becton Dickinson, Cockeysville, MD, USA), a light absorbing dye was used to enhance the photon absorption. Indocyanine is a water soluble dye with absorption peak ranges from 800-nm to 810-nm as shown in Figure 3.5 [45]. When used with a near-infrared laser in situ, ICG can help achieve selective absorption of light. A 0.25% homogeneous solution of ICG was prepared in deionized water and mixed with semi-liquid target gel phantom.

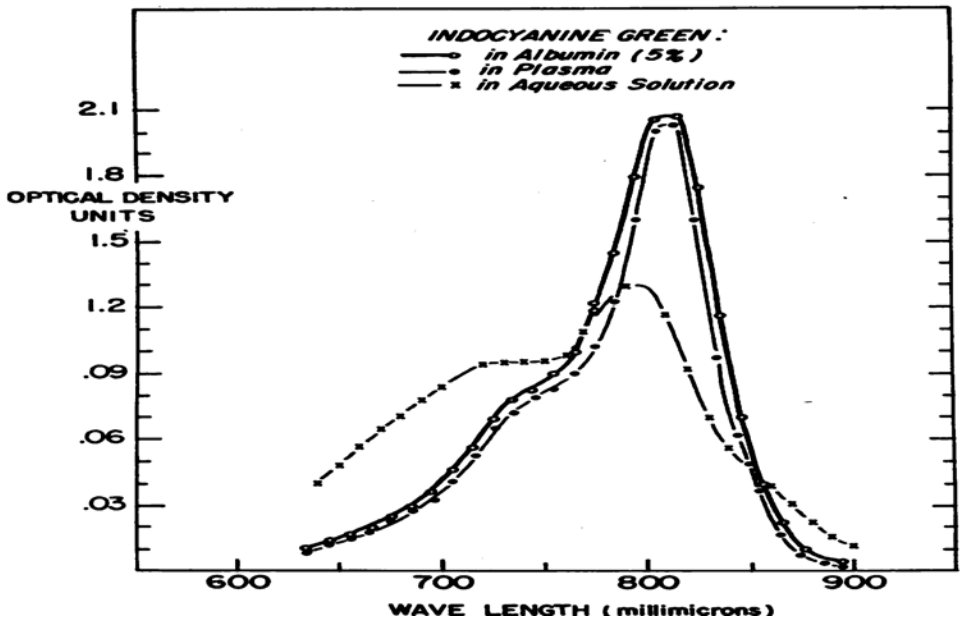

Figure 3.5 Experimental absorption spectra of ICG in Albumin, Plasma, and in Water [45].

3.4.3 Light Source

A diode laser of wavelength 805-nm (Diomed 25, Diomed, Cambridge, UK) was used to irradiate the tumor. The laser power was delivered through a 7-meter long microlens optical fiber (Pioneer Optics, Windsor Locks, CT) to separate laser from the MRI machine. The reason for such a long fiber is because metals can not be placed near

MRI machine. The output power of the laser was measured using optical power meter (Scientech Astral AD30, USA) for a proper field of view (output ring of diameter 1.34cm, power density 1 Wcm^{-2}). The beam profile of the laser source is rectangular (flat). The beam profile as obtained experimentally is shown in Figure 3.6. The spot size was changed according to the size of tumor so as to keep the output power density to be $1Wcm^{-2}$.

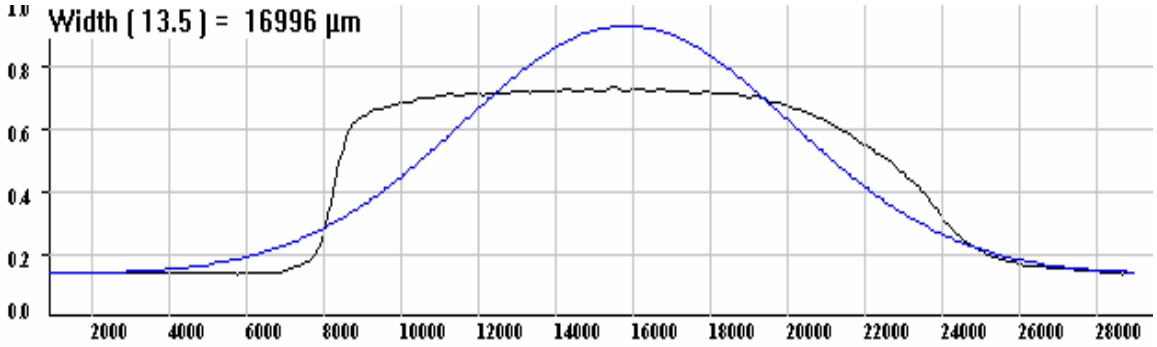

Figure 3.6 Beam profile of the laser obtained in our lab. Black solid curve represents the beam profile of the laser whereas the blue curve is the Gaussian beam profile of same data for comparison.

3.4.4 Method of Acquiring Images

MRI experiment was conducted on a MRI facility 7.1T Bruker 730 USR 30cm horizontal-bore small animal MR imaging system powered by ParaVision 3.0.2 software (Bruker BioSpin MRI GmbH, Germany) at the Oklahoma Medical Research Foundation (OMRF). The machine has greater than 80 mm image resolution of gradient system for rats and greater than 50 mm for mice. It has cardiac and respiratory monitoring device with ore isoflurane anesthetic machine. The MRI core facility is equipped with state-of-the-art equipment for small animal magnetic resonance imaging and spectroscopy. This

facility is capable of providing morphological, functional and metabolic imaging for tissues or organs in mice, rats, and rabbits.

Figure 3.7 A 7 tesla small animal MRI facility used in the study (OMRF, Oklahoma City).

The change in water proton chemical shift with the change in temperature is the basis for the temperature measurement. Fast-low-angle-shot (FLASH) gradient echo sequence method was used to acquire images. The typical parameters used to acquire images were: echo time (TE) / repetition time (TR) = 10/158 ms, field of view (FOV) =

5.5 cm x 5.5 cm, image dimensions of 128 x 128 pixels for phantom samples and 256 x 256 pixels for rats, flip angle = 30 degrees, slice thickness = 2.0 mm.

3.5 Results

3.5.1 Calibration Curves

System calibrations were performed using phantom and chicken samples during a natural temperature elevation from + 4 ^{0}C to + 23 ^{0}C using thermocouples, infrared thermography, and MRI. The results are shown in Figure 3.8. The thermal camera data show some higher value and faster temperature raise than the other two curves because the room temperature conditions could not be maintained as same as inside the MRI room where the cooling system inside the MRI machine keeps the room temperature lower than the outside temperature.

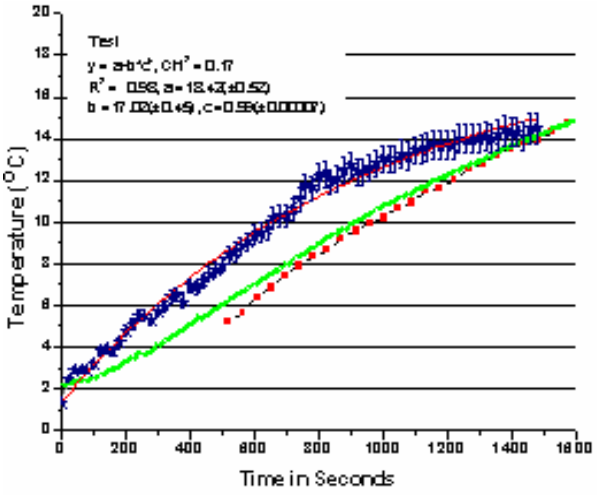

Figure 3.8 Calibration curves on phantom gel. Green thick curve represents the thermocouple data and the point-line plot represents the MRI data. The data from the thermocouple and MRI are compared with the thermal camera surface temperature (the blue curve). 5% error bars are shown relative to the standard fit (red line).

A calibration factor was calculated using the known temperature from the calibration data and the temperature calculation was performed by multiplying the factor on the unknown temperature of the sample.

3.5.2 MR Temperature Measurement in Gel Phantom

3.5.2.1 Image Processing on Gel Phantom

The MRT technique uses the protons of water and fat molecules in the sample. The sample is excited by applying radio frequency (rf) pulses and the tissue sample de-excites to generate output signals. These signals are received and collected to form an image. After the Fourier transform analysis using a proper algorithm, a phase matrix of known dimension is obtained and the matrix so obtained is used in the phase-temperature equation (Equation 3.24 and 3.26) to calculate a temperature matrix. This matrix was analyzed to obtain the temperature distribution in the desired region as shown on the flow diagram in Figure 3.9. The temperature distribution inside the gel phantom was determined during laser treatment. Figure 3.9 shows the signal data processing of MR phase images for temperature measurement. The magnitude image (Figure 3.9 (d)) is used as a filter function. This is a matrix having the same dimensions as that of phase-data matrix whose elements outside the phantom (inner rectangle) are taken to be 0 while all other elements on the inner rectangle are taken 1. This functions to minimize the noise in the data.

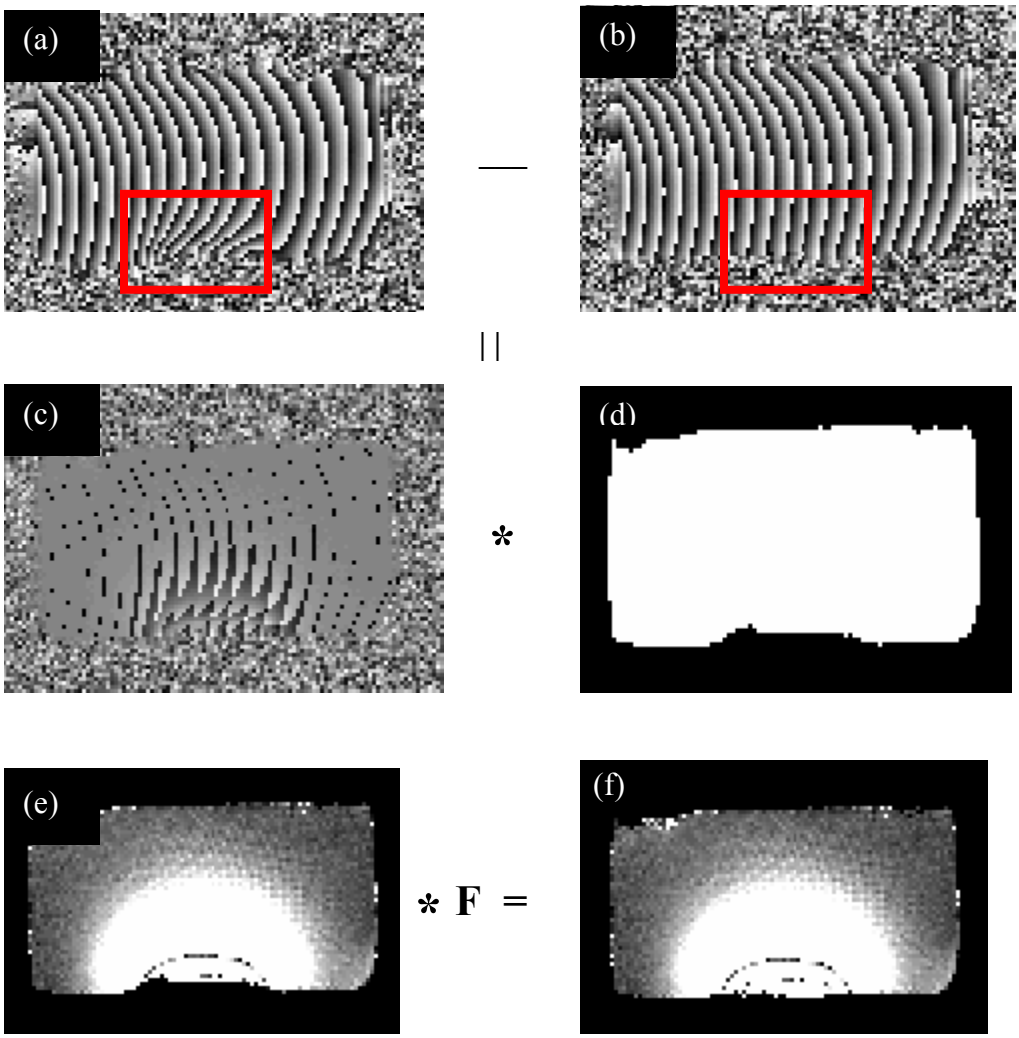

Figure 3.9 Flow diagram of MR image processing to obtain filtered phase-image and temperature-image. MRI phase maps of 4% gelatin phantom at different temperatures are illustrated. (a) 12th phase image after heating (small rectangle indicates the target phase change due to temperature rise): maximum phase angle = 3.14068108 radians, minimum phase angle = 0.000031477 radians, (b) 1st phase image before heating: maximum phase angle = 3.14155312 radians, minimum phase angle = 0.0001053 radians. (c) The phase difference (a) - (b) = (c) which has maximum phase angle = 3.13853 radians and minimum phase angle = -3.119789 radians. (d) Filter function designed from magnitude image to remove noise in delta-phase image. (e) Filtered phase-image obtained from the matrix multiplication of images (c) and (d). (f) Temperature image obtained after element-by-element multiplication by a factor F (Equation 3.24) on delta-phase image (e).

A typical temperature distribution inside a gel phantom specimen is shown in Figure 3.10. The phase information was acquired from reconstructed data images obtained using FLASH sequence method. The original MRI data were reconstructed into real and imaginary parts to obtain the phase information. The magnitude signals of

certain images were used as a filter with certain threshold set in the algorithm to eliminate the noise. The parameters were optimized to have high signal-to-noise ratio, low phase angle, and short data acquisition time.

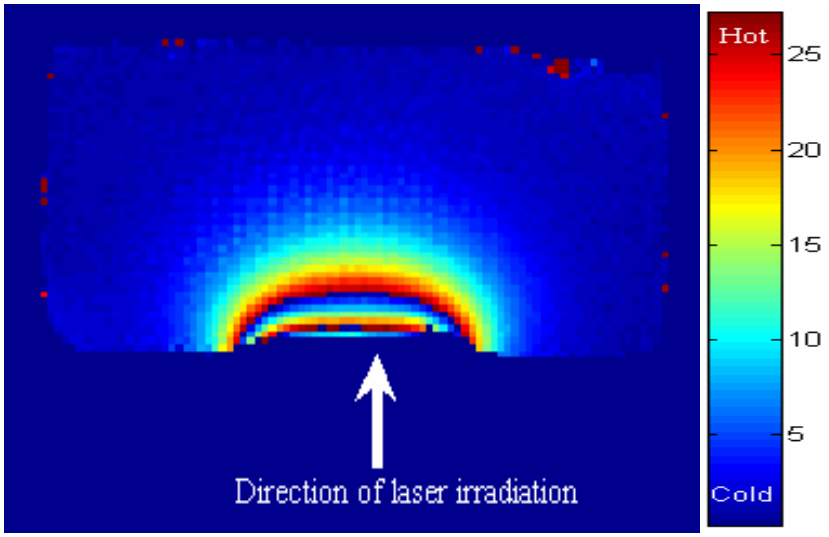

Figure 3.10 A typical MRI thermometry. Temperature isotherms are shown on 4% gelatin phantom of the 12^{th} image for a 10^{th} slice cut saggitally during gradient echo sequence. 16 slices each with 28 images of size 128x128 were acquired at equal intervals of 20 s. The arrow indicates the direction of laser irradiation. The color bar represents the hot and cold regions on tissue.

Temporal profiles of temperature distribution are given in Figure 3.11 with 23 images. The z-axis is the temperature axis and r-axis is the position axis. The temperature-position graphs on the right side of each image correspond to the temperature profile belonging to some time intervals. These graphs reveal the temperature change corresponding to position in pixels. If all peak temperatures are plotted with time, the temperature increases exponentially and attains its equilibrium condition during the laser is turned on. Therefore, it decreases exponentially after the laser is turned off.

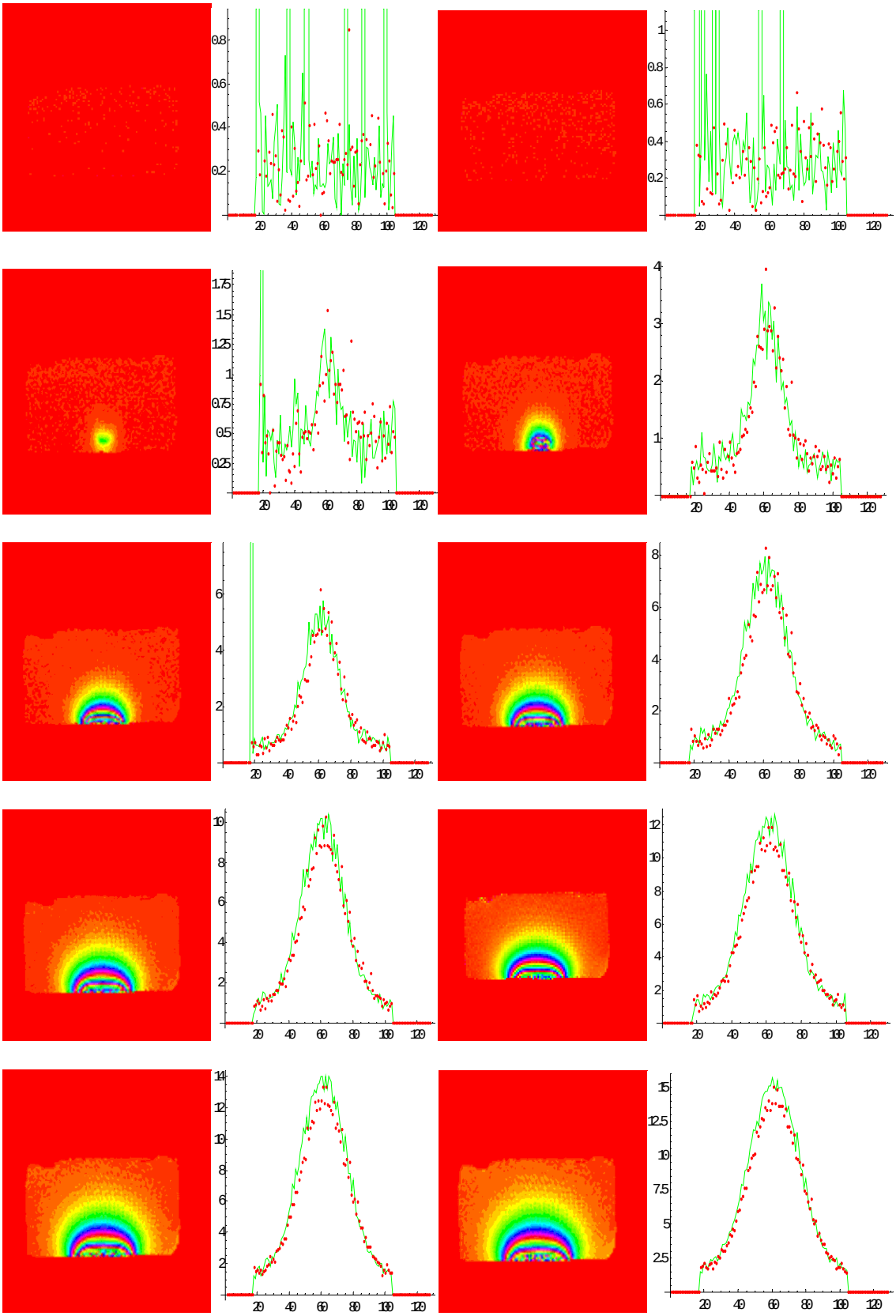

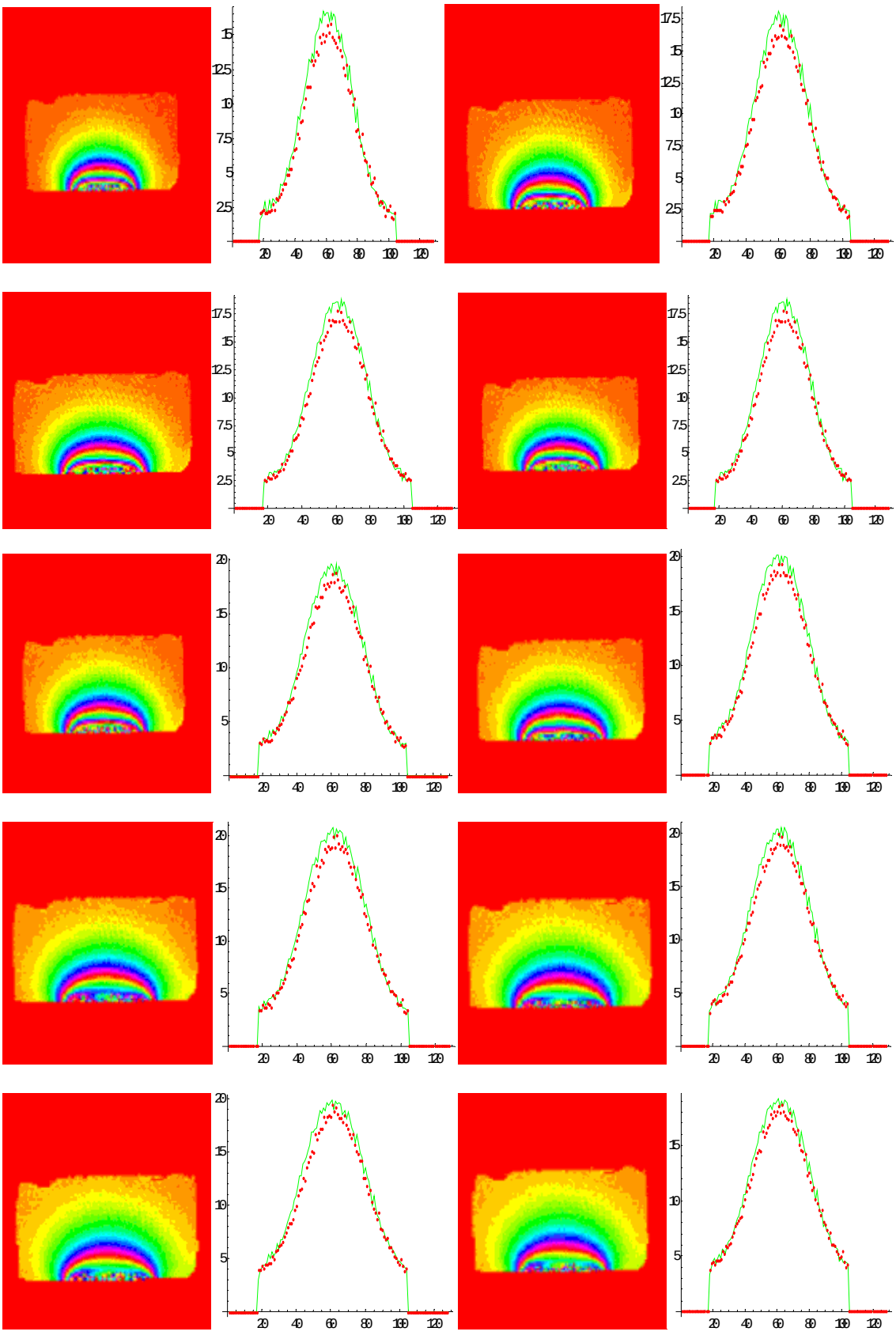

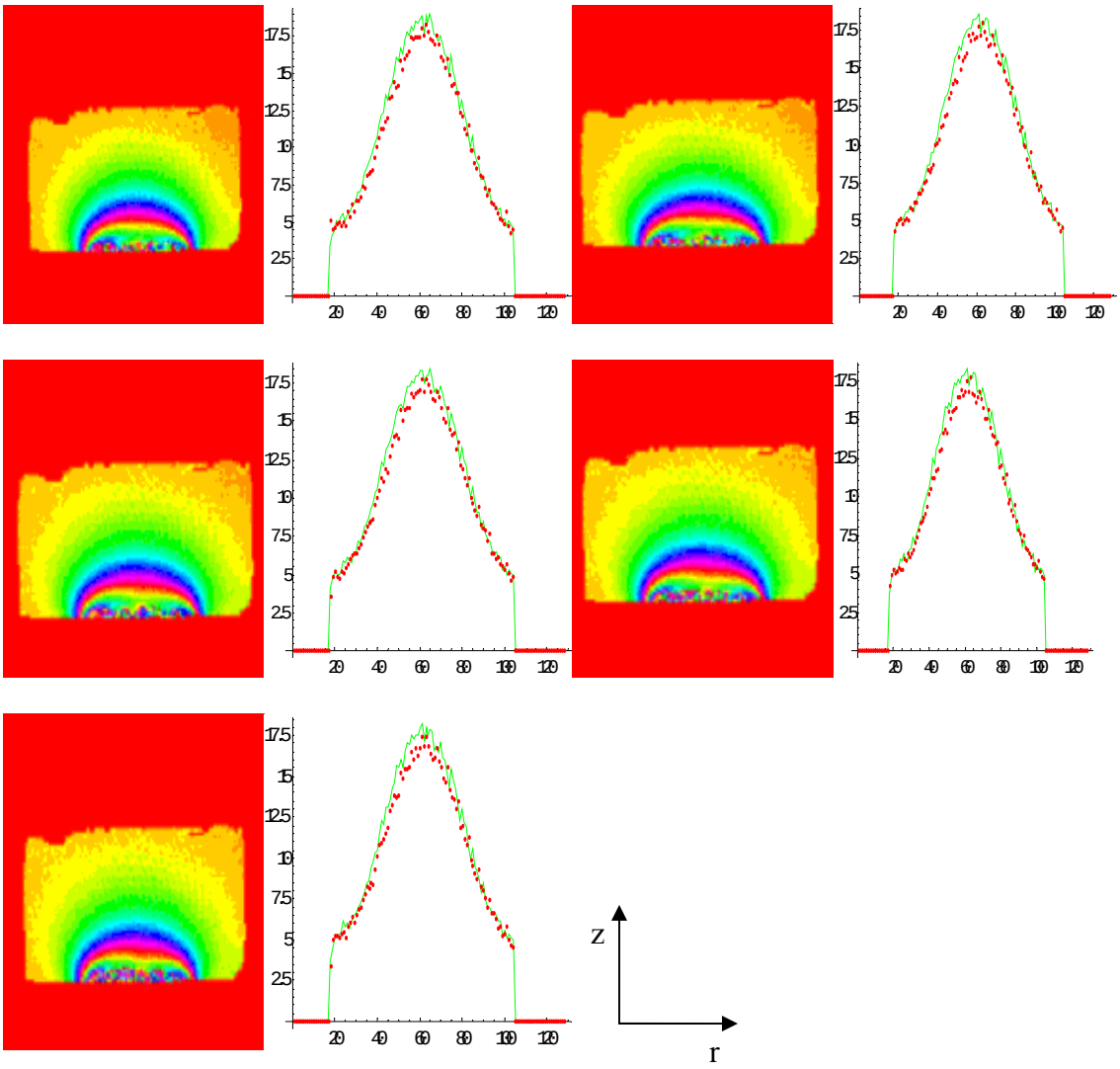

Fig.3.11 Analysis of temperature T(r, z, t) on 4 % gel phantom sample from reconstructed images acquired from MRI data. The cylindrical phantom tissue is sliced saggitally so as to get the rectangular projection images as shown. Twenty eight images of 128 x 128 pixel size were taken each image 20s after its preceding image. The temperature-increase profiles as a result of 805-nm wavelength laser irradiation corresponding to an increase in time of irradiation are shown at the right side of each image.

3.5.3 MR Temperature Measurement on Animals

A total of 10^5 viable tumor cells per animal were aseptically injected sub-Q in the lumber area of DMBA-4 female Wistar Furth rats which were used for MRI imaging (see Figure 3.12). The laser beam was focused on the tumor. Prior to treatment, animals were

anesthetized and the hair overlying the tumor was removed. The MR images were acquired during the laser irradiation of the tumor. The temperature distributions on the rats are shown in Figure 3.13. All the procedures in the animal experiments are in compliance with protocol approved by the Institutional Animal Care and Use Committee (IACUC).

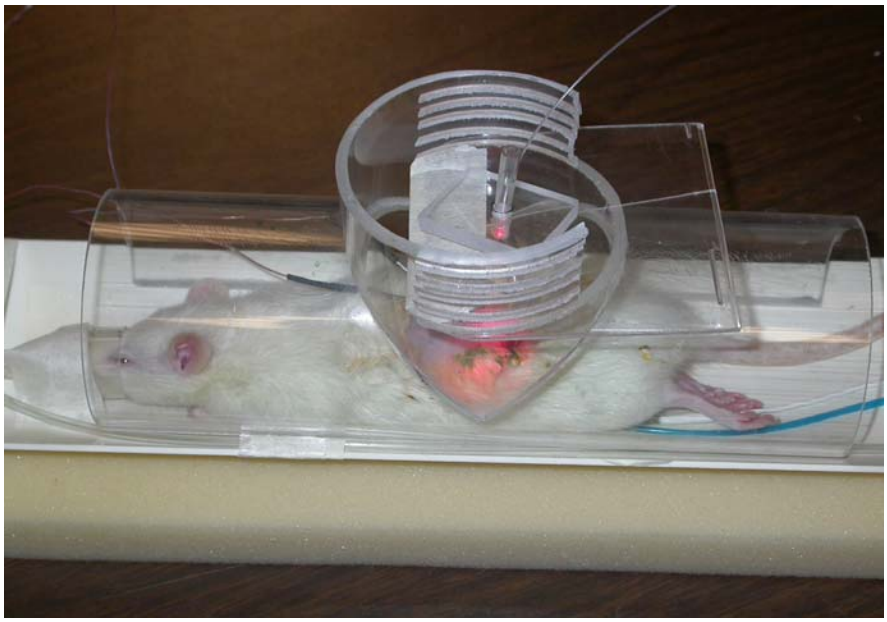

Figure 3.12 Anesthetized rat ready to place in the open bore MRI scanner. The rat is provided with an anesthetic inhalation and heart beat sensor during treatment.

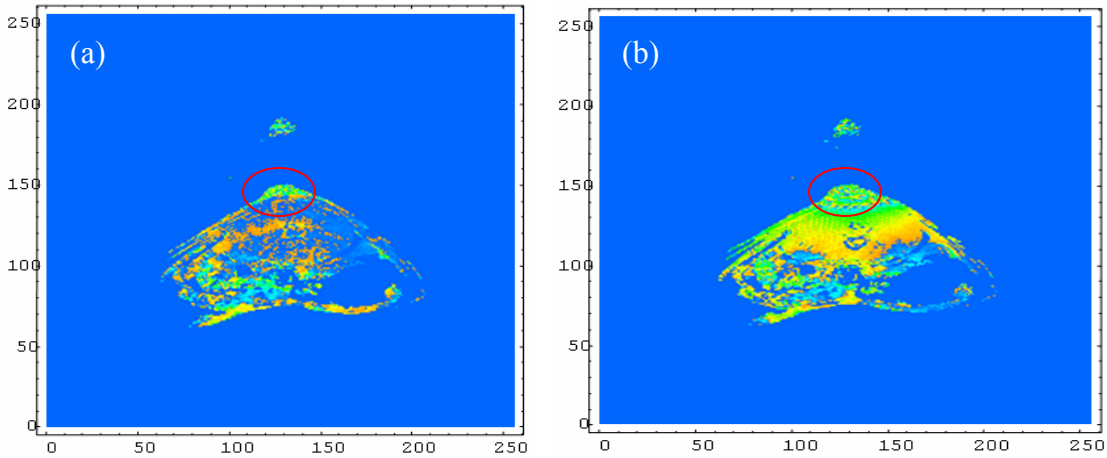

Figure 3.13 Temperature map of a rat. Reconstructed data images acquired from MRI scanner were analyzed using Matlab and Mathematica software. Red circle indicates tumor. The phase image difference is obtained by subtracting 1st phase image from 6th phase image and the temperature image (a) is obtained on multiplying by a factor F as in Equation 3.24. Temperature image (b) is obtained after 5 min of laser irradiation. The reduction in tumor size can be observed.

3.6 Discussion and Conclusion

Proton density resonance frequency (PRF) offers a number of advantages. It has high signal-to-noise ratio (0.20mm-0.40mm) and spatial resolution. The calibration curves in Figure 3.8 show a good agreement among the three temperature probes. The temperature calibration experiments were carried out on a gel phantom specimen. The thermograph data show slightly faster temperature rise than MR imaging thermometry. The reason for the thermograph result are slightly higher than the other two probes may be because of the heat radiation coming out of the heated tumor have additional back scattered radiation directly from the surface of the tissue layer overlying the tumor. The other reason for this discrepancy can be improper distance between specimen and the thermal camera.

The results of this study (Figures 3.10 and 3.11) show that MRI thermometry is feasible for the controlled temperature measurement both ‘in vitro’ and ‘in vivo’

experiments. In the case of MRI temperature measurement, in vitro studies show excellent results (see time series results of Figure 3.11). However, the in vivo measurements in rats show some noise in the images (as shown in Figure 3.13(b)). The reason of noise in the images may be due to the fact that the pulse rate and the radio frequency pulse repetition time may not have synchronized. Another reason could be because of the differences in the body temperature with the varying depth of tissue. Density of chromophores for laser light absorption and differing blood perfusion rates at different depth of tissue can also cause the temperature variation. Another reason for the inhomogeneous temperature distribution may be because of "inhomogeneities" in the laser irradiation such as diffusion.

The results from this study indicate that when all uncertainties are considered together, MR imaging-derived thermometry provides an index that can be used to estimate the threshold temperature and tissue damage during laser tumor treatment experiments. MR imaging thermometry offers a distinct advantage over traditional thermocouples used in determining temperature thresholds for tissue damage. With advances in MR imaging thermometry, temperature distribution can be controlled with sufficient precision. Knowledge of threshold exposure necessary to cause tissue damage as well as noninvasive temperature monitoring can help for optimal thermal treatments. An example of such exposure is to increase the blood vessel permeability for targeted drug delivery, or in delivery of gene in gene-therapy [46].

Chapter 4

Infrared Thermography (IRT)

4.1 Introduction

Skin temperature is the indicator of pathology or diseases underlying the skin. Thermal abnormalities, either elevated or depressed, are usually observed due to metabolic irregularities present in the body [47]. With the advancement in the new generation of IR thermographers, it is possible to make thermal images of the extended areas of skin to find out the abnormalities. It is also possible to establish correlations between unusual or abnormal thermal patterns and the presence of pathology within tumor as well as determining the temperature gradients between adjacent points and areas of skin, which helps localize the affected region [47]. This technique is safe and noninvasive because it uses spontaneously emitted radiant energy out of the skin.

Digital imaging temperature measurement has been a useful method in determining the surface temperature on a patient with skin and breast cancers [48]. For a surface with a tumor surrounded by healthy tissue, temperature changes have been found ranging from 1- 2 ^{0}C [48]. These changes result from the rapid oscillation in the skin blood perfusion. The tumor mass has lower temperature than its healthy surroundings. The reason for this discrepancy is due to the hypervascularity around the tumor which results from the rapid formation of new blood vessels [48]. For example, the increased metabolic activities and vascular neogenesis in breast cancer results in changes in the

breast surface temperature which helps detect early breast cancers [49]. Improved temperature sensitivity of current IR thermography makes it possible to detect temperature variations on the order of 0.1^0C [49]. Unlike earlier versions, the new cameras do not require thermal cooling. The spatial temperature resolution is significantly improved, and they are portable due to marked size reduction. This has resulted in an expansion of the potential use of infrared thermography (IRT) in clinical applications [50]. Infrared imaging can be used as a non-invasive method for assessing tumor angiogenesis. This technique can be used for temperature images.

Human skin behaves as an efficient blackbody radiator of heat in the wavelength range of 2 μm to 14 μm [51]. Therefore, it is possible to detect temperature changes due to many factors such as pathology underlying the skin using infrared camera. Infrared thermography has been used successfully in the studies of neurology, vascular disorders, rheumatic diseases, tissue viability, breast cancer, and dermatological disorders [51]. This technique also has been used successfully in photodynamic therapy (PDT) using photosensitizers such as 5-aminolaevulinic acid (ALA) and Photofrin [52].

In photothermal therapy, light is either scattered or absorbed when it enters on tissue and the extent of both processes depends on tissue type and light wavelength. Tissue ablation threshold, extent of peripheral tissue damage, laser pulse duration, laser power, beam size, and the beam profile have been modeled [53]. Tissue optics involves measuring the spatial/temporal distribution and the size distribution of tissue structures and their absorption and scattering properties. This is difficult because the biological tissue is inhomogeneous and the presence of microscopic inhomogeneities (such as macromolecules, cell organelles, organized cell structure) makes tissue a turbid medium.

Multiple scattering within a turbid medium leads to spreading of a light beam and loss of directionality. Absorption is mainly due to endogenous tissue chromophores such as hemoglobin, myoglobin, and cytochromes [54].

Photothermal therapy can be an effective modality for disease treatment due to its direct tissue thermal impact. During photothermal therapy, measurement of surface temperature can be crucial. For thermal effect desired at deeper tissue, excessive surface temperature increase can cause undesirable surface tissue damage, which can impede the absorption of thermal energy by deeper tissue. If the surface temperature is too low, it indicates insufficient energy delivery to the target. Therefore, appropriate laser parameters and procedures are important for optimal selective photothermal effect.

To study the photothermal effect during laser irradiation of biological tissue, Monte Carlo method can be used to simulate the propagation of laser photons in tissue [9]. It helps acquire the information of photon absorption in tissue, and together with finite difference method, it can be used to determine temperature distribution during and after laser irradiation. The details of simulation procedures are discussed in chapter 2.

In this study, infrared thermography was used to measure surface temperature during laser irradiation using gel phantom, chicken breast tissue, and tumor-bearing animals. Theoretical studies of the surface temperature using Monte Carlo simulation were also performed. This study is an attempt to acquire temperature distribution to guide laser photothermal treatment of tumors.

4.2 Infrared Radiation and Detection

4.2.1 Radiation from Tissue

An object at a temperature higher than absolute zero emits electromagnetic radiation. The infrared radiation is the part of the electromagnetic spectrum with a wavelength ranging from 0.75 microns to 30 microns. This spectrum consists of sub-wavelength bands such as 0.75-3 microns near-infrared (NIR), 3-6 microns mid-infrared (MIR), 6-15 microns far-infrared (FIR), 15-30 microns extreme infrared (EIR). A thermal camera which works in the MIR wavelength band was used. The concept of blackbody emissivity is the basics of the IR thermometry. The characteristic distribution of emitted blackbody radiation is given by Planck

$$dL_\nu = \frac{2\pi h}{c^2} \frac{\nu^3 d\nu}{e^{h\nu / k_B T} - 1} \tag{4.1}$$

within the frequency interval ν and dν where h is Planck constant, k_B is Boltzman constant, and T is absolute temperature. The Planck's distribution function has a well defined maximum at a frequency, which is a function of temperature, and decreases exponentially at higher frequencies and more slowly on the lower frequencies. Emissive power of a black body decreases exponentially with temperature and the wavelength of maximum emissive power moves to longer wavelengths as the temperature falls in accordance with Wien's law

$$\lambda_{max} T = 0.002898 \text{ m.K} \tag{4.2}$$

where λ_{max} is in meters. The emissivity is equal to the ratio of the body surface emissive power to the blackbody emissive power at the same temperature

$$\varepsilon_\nu = \frac{E_\nu}{E_{b\nu}} \tag{4.3}$$

which is the well known Kirchhoff's law of radiation.

For such a radiation emitting from a body with emissivity ε, the radiance is

$$dL_\nu(\nu, T) = \varepsilon \frac{2\pi h}{c^2} \frac{\nu^3 d\nu}{e^{h\nu/k_B T} - 1} \tag{4.4}$$

Integrating over the whole frequency range we get,

$$L_\nu(\nu, T) = \varepsilon \frac{2\pi}{c^2 h^3} \int_0^\infty \left(\frac{h\nu}{k_B T} \right)^3 \frac{d(h\nu/k_B T)(k_B T)^4}{e^{h\nu/k_B T} - 1} = \varepsilon \frac{2\pi (k_B T)^4}{c^2 h^3} \int_0^\infty \frac{x^3 dx}{e^x - 1} \tag{4.5}$$

where $x = \frac{h\nu}{k_B T}$. The integral $\int_0^\infty \frac{x^3 dx}{e^x - 1} = \frac{\pi^4}{15}$ simplifies the power as

$$L_\nu(T) = \varepsilon \left(\frac{2\pi^5 k_B^4}{15 c^2 h^3} \right) T^4 = \varepsilon \sigma T^4 \tag{4.6}$$

which is known as the Stefan-Boltzmann law and $\sigma = \frac{2\pi^5 k_B^4}{15 c^2 h^3} = 5.67 \times 10^{-12} W cm^{-2} K^{-4}$ is called the Stefan-Boltzmann coefficient. Thus, every object above absolute zero temperature emits radiation which is proportional to the fourth power of temperature. [55]

4.2.2 Concept of Photon Detection

Infrared detectors are transducers of radiant energy. They are classified into quantum detectors (photon) and thermal energy detectors. The infrared detector (FLIR Applications Engineering Group, Boston, MA) has a photon detector which converts photons into free current carriers by exciting electrons in the lattice sites across the energy band gap of the semiconductor to the conduction band which results in the voltage

or current output signal. Therefore, the temperature of the detector must be low enough for the minimization of the thermally excited electrons that add up to the photon current.

4.2.3 Charge Coupled Devices (CCD's)

The signals detected by the detectors are stored and transferred as output signal to form an image by the array devices called charge coupled devices (CCD). A charge coupled device passes information between spatial locations by transferring discrete packets of electronic charge. The position of the charge in the Metal Oxide Semiconductor (MOS) arrays of capacitors is electrostatically controlled by voltage levels. By a proper use of voltage levels and relative phases, MOS capacitors are capable to store and transfer the charge packets across the semiconductor substrate. Those CCD arrays are able to work in the wavelength range from visible to mid-infrared band but our work exploits the 3 μm - 15 μm wavelength window only [55].

MOS Capacitors

MOS capacitors are the basic units of the CCD arrays. These capacitors are made by coating Oxide (SiO_2) on the Si plate and on top of the oxide layer Aluminum (Al) metal is coated. The structure is soldered onto a p-type Silicon (Si) wafer as shown in Figure 4.1.

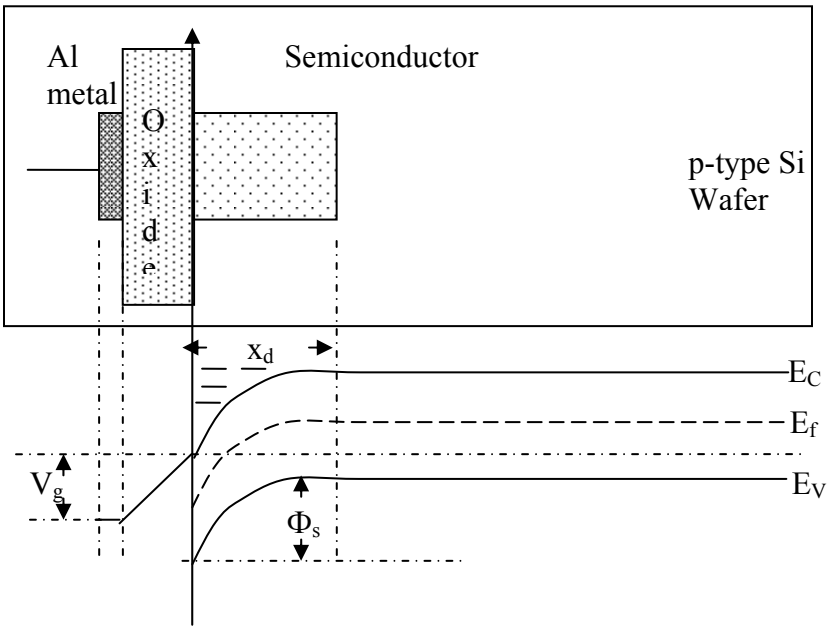

Figure 4.1 Schematic structure and the corresponding potential well formation of MOS capacitors.

Positive bias voltage on the metal gate produces a depletion region. Because SiO_2 is an insulator there is no charge transfer from the oxide wall and on the other side of the well the surface potential Φ_s helps keep the charges stored in the depletion region.

A positive voltage is applied on the gate which repels the holes in the p-type semiconductor creating a region of depleted positive charges. This region is called the depletion region. Even a small positive charge can cause the conduction band and the valance band to bend creating a lower potential well in the depleted region. In this well electrons (minority carriers) can be accumulated. The potential at the oxide-silicon interface is called the surface potential Φ_s. If a photon with energy greater than the band gap is absorbed in this depletion region it produces electron-hole pair. The hole moves

away from an oxide surface while electrons are held in the depletion region. The amount of negative charges that can be collected is proportional to the applied voltage, oxide thickness and area of metal gate electrode. Therefore, there is a control over the collected charges. The distribution of charge in the MOS capacitor is explained by the Poisson equation,

$$\nabla^2\Phi = \frac{\partial^2\Phi}{\partial x^2} = -\frac{\rho}{\varepsilon} = \frac{qN_a}{\varepsilon} \qquad (4.7)$$

this leads to

$$\Phi = \frac{qN_a}{2\varepsilon}x^2 \qquad (4.8)$$

where N_a = accepter doping concentration, ε = dielectric constant of oxide, q = -e is the electronic charge which makes the potential negative. The potential is constant in metal, linearly varies in oxide and is quadratic in the depletion region. This surface potential has a minimum at the oxide-semiconductor interface enabling accumulation of charges called surface channel CCD capacitor or the MOS capacitor [55].

Concept of charge transfer in an array of MOS capacitors

MOS capacitors are biased by sequences of pulsed voltages to transfer packets of charges periodically. The amount of charge is the signal output. The potential of the well is determined by the applied gate voltage and the oxide thickness. So the voltage level on the gate are varied serially as $V_n > \ldots\ldots V_3 > V_2 > V_1$ to create adjacent minimum

potential well. The transferred charge is forced to move only column wise by using channel stops.

Readout Technique

The charge is transferred off the CCD array into diffusion potential well via a transfer gate and the diffusion is connected to a transimpedance amplifier circuit that converts the charge to voltage. This technique is called the destructive readout technique which is commonly used in IR cameras [55].

4.3 Materials and Methods

The schematic diagram below shows the experimental setup for the measurement of surface temperature using the IR camera. Two temperature probes: one the thermocouples and the other IR camera were used together to compare data.

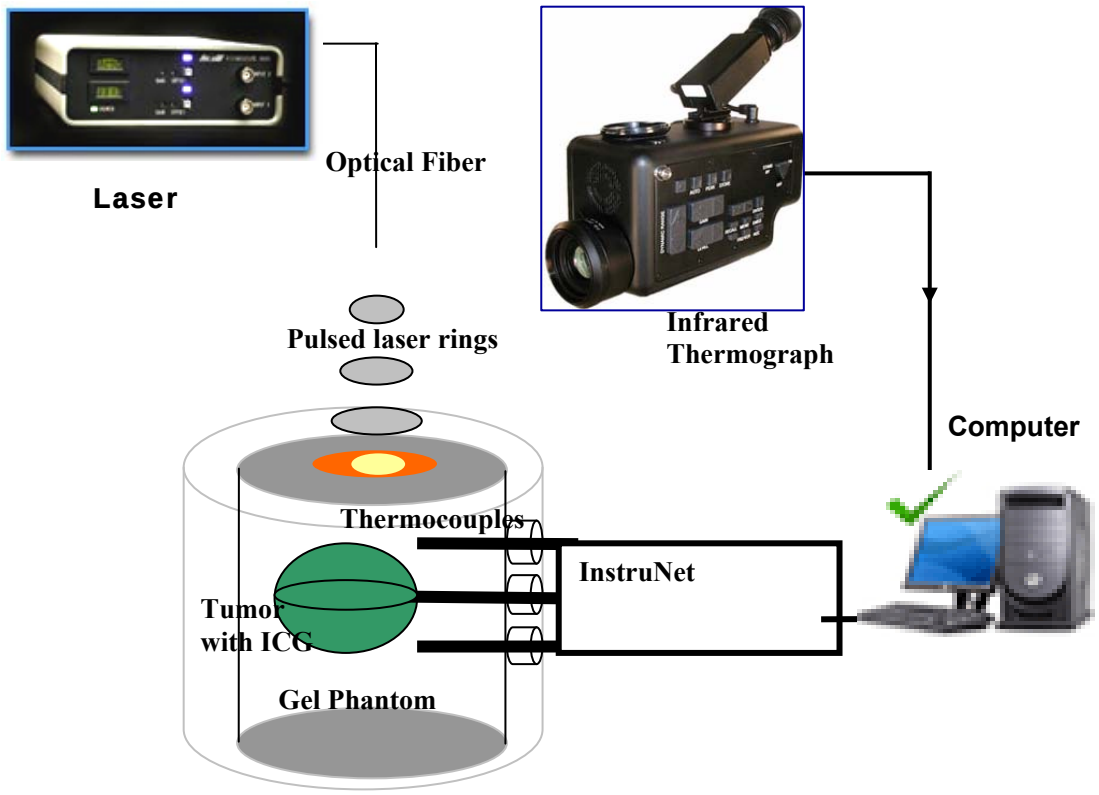

Fig. 4.2 Schematic experimental set-up for infrared thermography.

4.3.1 Phantom Sample Preparation

Gelatin phantoms were used in this experiment to simulate biological tissue. The ICG-mixed gel was used to simulate absorption-enhanced target for selective photothermal interaction. Both target and non-target phantom specimens were prepared by mixing 76 ml of water in 20 ml of lyposin and 4 gm of gelatin powder. After thorough mixing, gel samples were allowed to solidify at 4^0C. Target phantoms were

prepared by solidifying the homogeneous target gel with ICG solution. A spherical solid phantom with dye was then buried in the non-target gel.

4.3.2 Dye Enhancement

Indocyanine green (ICG) (Akron Inc., Buffalo Grove, IL) is a chemical with an absorption peak at a wavelength range of 800-810-nm [45, 56]. When used with a near-infrared laser, in situ ICG can help achieve selective absorption of light. A 0.25% homogeneous solution of ICG in deionized water was prepared. This dye solution was mixed with target gel phantom. The absorption spectra of the ICG are shown in Figure 3.4 under the subsection 3.4.2 of chapter 3.

4.3.3 Light Source

The same 805-nm diode laser in section 3.4.3 was used. Here, the spot size was varied according to the size of the target, while keeping a constant power density of 1 W/cm^2.

4.3.4 Thermocouples

Thermocouples are temperature sensors. In our experiments, Chromel (Ni-Cr alloy) sensors were used. They convert thermal potential difference into electrical potential difference. They can measure a wide range of temperatures such as -200 ^{0}C to +1200 ^{0}C. The main limitations are precision in measurement, and system errors less than 1 ^{0}C is difficult to achieve. The sensors were connected to an analog-digital converter and the temperature data were directly transferred to an Excel file. These data help to compare the data from IR image and MR image analyses.

4.3.5 Measurement of Surface Temperature

The Prism DS (digital storage) IR camera from FLIR Applications Engineering Group (Boston, MA) was used to detect emitted thermal energy in the medium

wavelength spectral range of 3.6 - 5 micron. Real-time images were displayed on a LCD monitor (Sharp, Japan) showing the relative intensity.

The camera remotely measures the absolute temperature of a specific point on a target. The camera provides a 25-mm lens and can detect a temperature range of -10 ^{0}C to 450 ^{0}C [58]. The images were acquired every eight seconds and analyzed with AnalyzIR$^+$5.0 software. The software enables us to investigate the mean temperature, maximum temperature, minimum temperature standard deviation, variance and emissivity.

Data were acquired from both the thermocouple and infrared thermography methods. During the laser treatment the infrared thermal camera was focused on the tumor to acquire the thermal images. These images were analyzed to obtain skin temperature profiles. The goal of this thermal mapping is to estimate the conditions of skin ablation and necrosis, tumor cell death caused by the heat and to study the noninvasive nature of the novel laser-immunotherapy method. The thermal mapping was first performed on several other samples such as gelatin phantom, agar gel, and chicken tissue.

4.3.6 Surface Temperature Measurement using a Mouse Model

A transplantable EMT6 mammary tumor model in female mice (C57BL-6) was used in our experiments. The mice were purchased from Harlan Sprague Dawley Co. (Indianapolis, Indiana) at the age of 5-6 weeks and weight of 15-25 grams.

The B16 melanoma tumor cells to be injected were stored frozen, grown in tissue culture, and injected 200 µl subcutaneously via 27 gauge hyperdermic needles on dorsal part of mice. Primary tumors appeared about 7-10 days after the tumor cell implantation.

In our experiment, immunoadjuvant glycated chitosan (GC, 200 µL, 1%) was injected intratumorally 24 hours prior to the laser treatment. ICG solution (200 µL, 0.25%) was injected intratumorally 30 minutes before the laser treatment. Prior to the treatment, the mice were anesthetized using a solution of xylazine and ketamine (15 mg xylazine to 87 mg ketamine) with a dose of 100 mg/kg intra muscularly (IM). Following the anesthesia overlying hair was clipped. All the procedures in the animal experiments were in compliance with protocol approved by the Institutional Animal Care and Use Committee (IACUC). The ICG and GC were injected into the center of the tumors and the tumors were irradiated by the 805-nm diode laser (power density 1 W/cm^2) directed to tumors for 10 minutes through a microlens-optical fiber with total energy delivery approximately 1000 J using a 1.5 cm beam size.

Four groups of mice were treated to investigate the role of changes in tissue conditions during the rise in temperature. The first group (1 mouse), a control mouse without tumor implantation, was used for the skin-temperature response study and was taken as the baseline. The second group (12 mice) was irradiated with the laser only. The third group (12 mice) was treated with the laser and ICG, and the fourth group (12 mice) was treated with the ICG and GC injections and followed by laser irradiation.

4.4 Results and Discussion

4.4.1 Measurement of Surface Temperature on Phantom

The thermal camera was used to acquire the thermal images during the dye-enhanced laser treatment experiments. Figure 4.3 (a) depicts an image of a dye-enhanced phantom sample inside of which a tumor was buried beneath a 2 mm thick layer of phantom. Fifty six such images were taken at time intervals of eight seconds and the corresponding temperature data were plotted as shown in Figure 4.3 (b) (squares). The experimental results were compared with the results obtained by simulation of surface temperature using the Monte Carlo finite difference method for the optical and thermal properties of dye-enhanced tissue (solid curve). The results are shown in Figure 4.3(b).

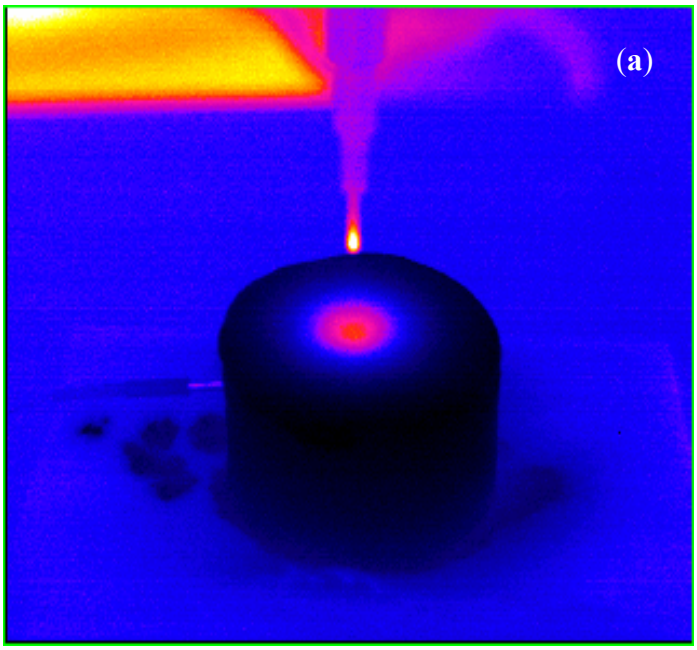

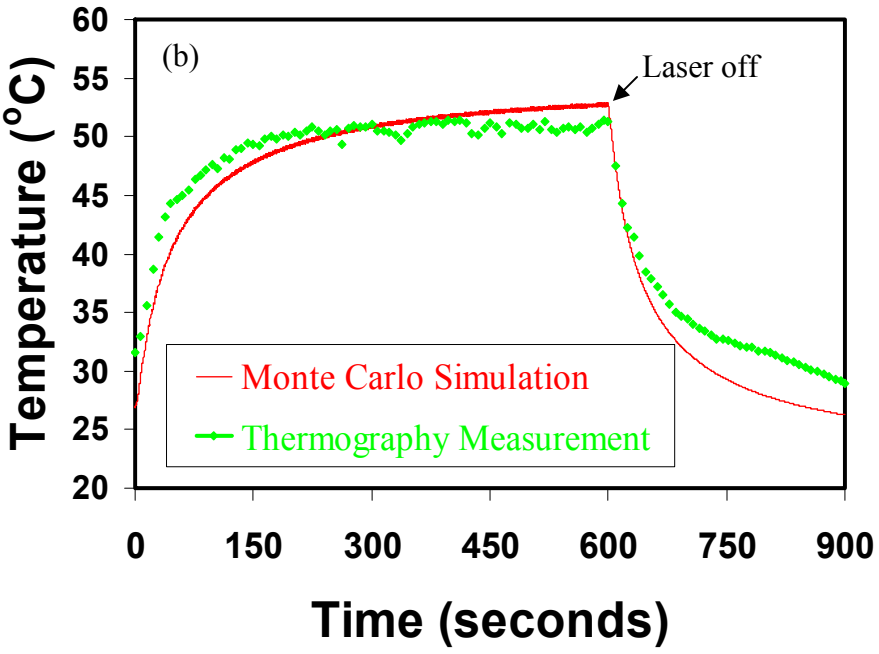

Figure 4.3 (a) Thermal image of a cylindrical gel phantom during laser irradiation. A spherical gel with enhanced absorption is buried beneath a 2-mm thick layer of normal gel. The sample was irradiated by the laser with a power density of 1 W/cm^2, a beam size of 1.5-cm radius, and a duration of 600 seconds. (b) Surface temperature at the center of the gel sample during the laser irradiation. Thermal images were acquired with a time interval of 8 seconds between two acquisitions. The temperature measured using the IR camera (diamonds) is compared with that of Monte Carlo simulation (thin curve).

4.4.2 Measurement of Surface Temperature using Chicken Breast Tissue

Experimental data from the images of the chicken breast tissue sample after 350 seconds after onset of laser irradiation were obtained as shown in Figure 4.4 (a). The surface temperature is plotted as a function of radius, r and angle θ using a matlab code (see appendix C), as shown in Figure 4.4 (b). A 3D-plot in Figure 4.4 (c) represents the radial surface temperature increase. The color bar indicates the scale of temperature for a particular color.

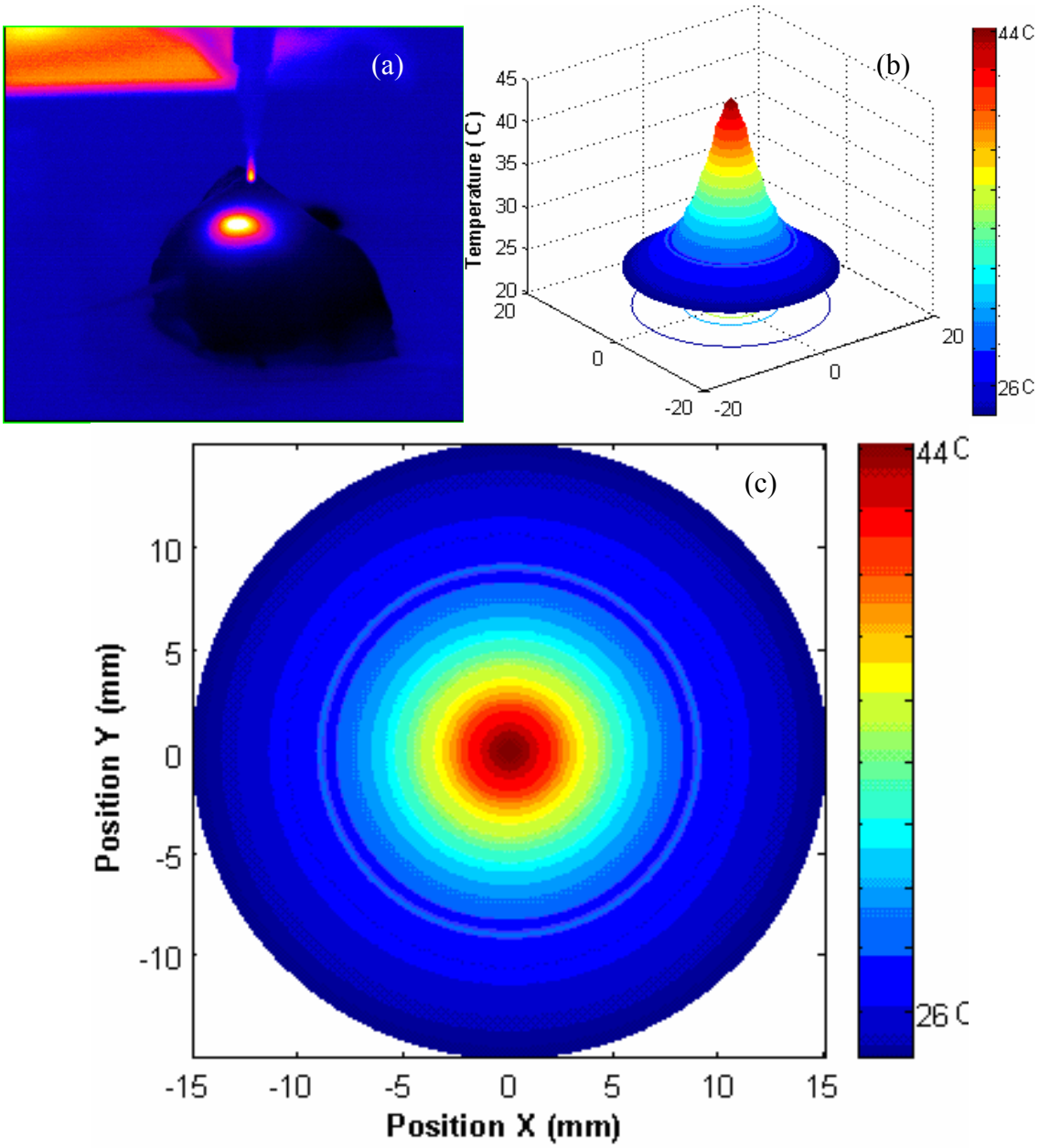

Figure 4.4 Temperature distributions on chicken breast tissue surface after laser irradiation of 350 seconds after irradiation of laser with a power density of 1 W/cm^2 and a beam radius of 1.5 cm. (a) The IR image of chicken during irradiation. (b) 2-D surface temperature distribution after the laser irradiation. (c) 3-D surface temperature distribution after laser irradiation.

4.4.3 Measurement of Surface Temperature using Live Animals

Thermal images on mice were acquired with on infrared camera as shown in Figure 4.5 and Figure 4.6. In the images, as the temperature rises the background color of the images becomes darker, whereas the bright spot is the tumor target. The first image is obtained after 8 seconds of laser irradiation. A total of 85 to 125 images were stored every 8s interval of time for all four groups of mice. The images were analyzed using AnaPlus5.0 software to determine the point and line temperature of the region of interest (ROI). The real-time image and line temperature plot on a mouse tumor injected with ICG are depicted in Figure 4.5. The peak temperature profile in Figure 4.5 (b) shows the rise in temperature on the target with minimum surrounding tissue damage.

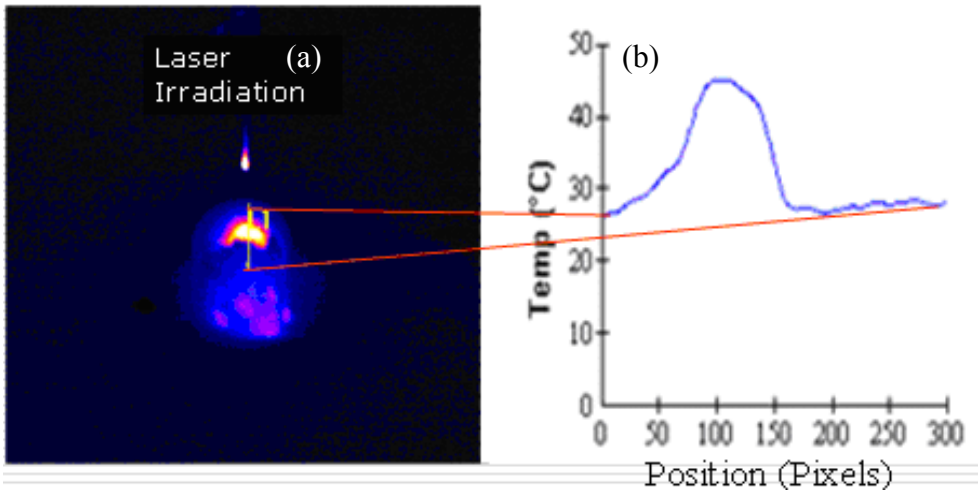

Figure 4.5 Real-time temperature measurements. (a) IR image acquired by the thermal camera for tumor-bearing mice injected with ICG. The laser power density was maintained 1W/cm^2. The image was acquired at time t = 150 seconds after the onset of laser irradiation. (b) The line temperature profile of the image on (a). The targeted tumor temperature rises to 46 ^{0}C sufficient for the onset of tissue destruction.

IR images of live mice injected with ICG and GC are shown in Figure 4.6. The laser power density was maintained at 1 W/cm^2. The change in color depicts the

temperature rise. In these experiments, three mice were treated at the same time using a beam splitter (Figure 4.6).

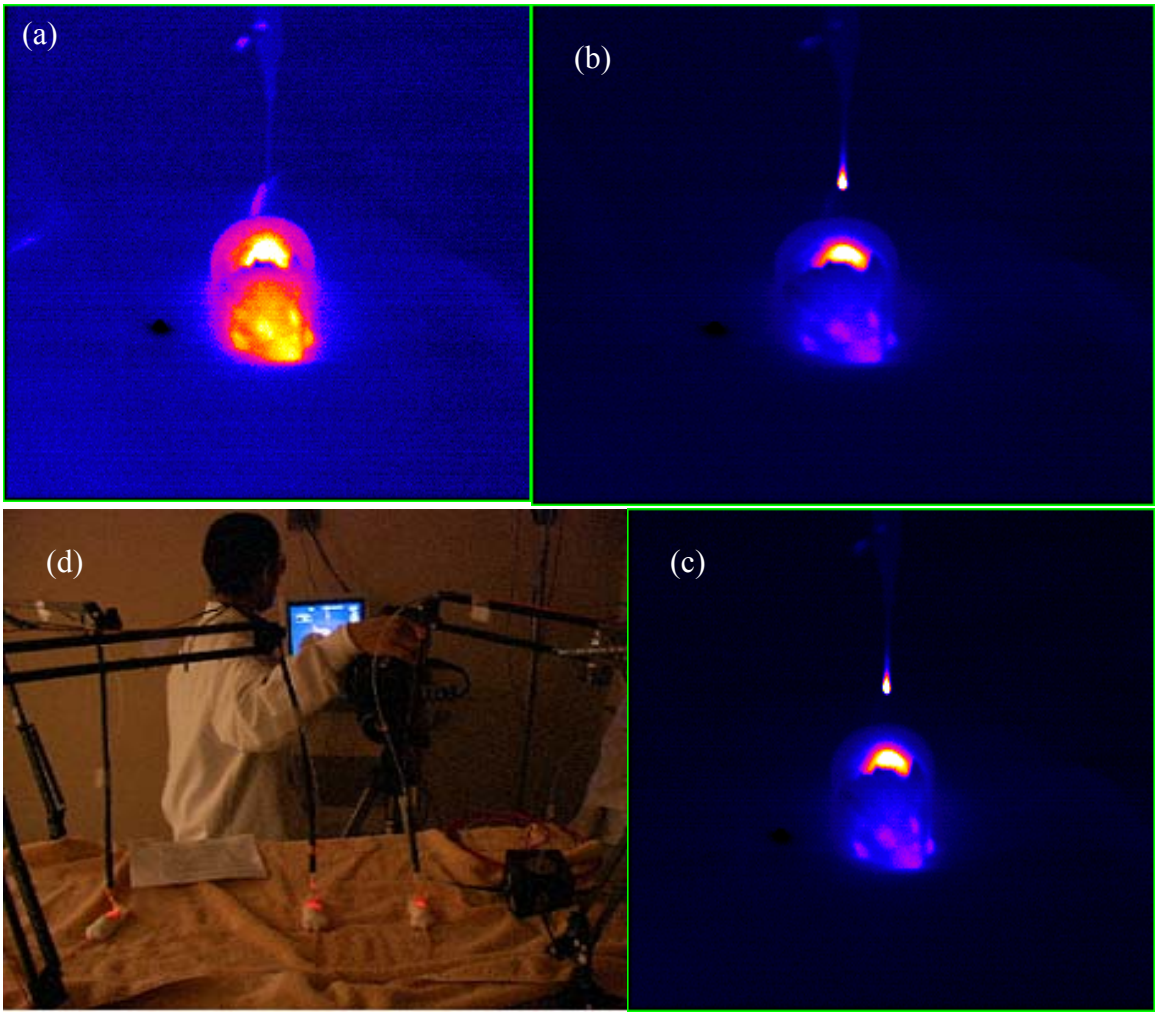

Figure 4.6 Infrared images acquired during laser irradiation on live tumor-bearing mice at different times. (a) Image after 40 seconds, the maximum temperature rises to 30^0C. (b) Image after 300 seconds, the maximum temperature reaches to 54^0C. (c) Image after 600 seconds, the maximum temperature rises to 65^0C. The laser power density was maintained at 1 W/cm^2 throughout the experiment, with a beam radius of 1.5 cm. The tumors were injected with GC and ICG before laser treatment (see text). (d) A real-time treatment experiment. Three mice were treated at the same time.

Temperature responses of skin and tumor to laser irradiation are shown in Figure 4.7. The mice were treated with 805-nm laser for 10 min with a power density of 1W/cm^2. The data compare the temperature response to laser with and without tumor. It is revealed

that tumor is more sensitive to laser absorption than the normal healthy skin. The heating rate and cooling rate are faster for tumors subjected to laser radiation and following completion of treatment. Data also show that the tumor is colder than the normal skin prior to laser treatment.

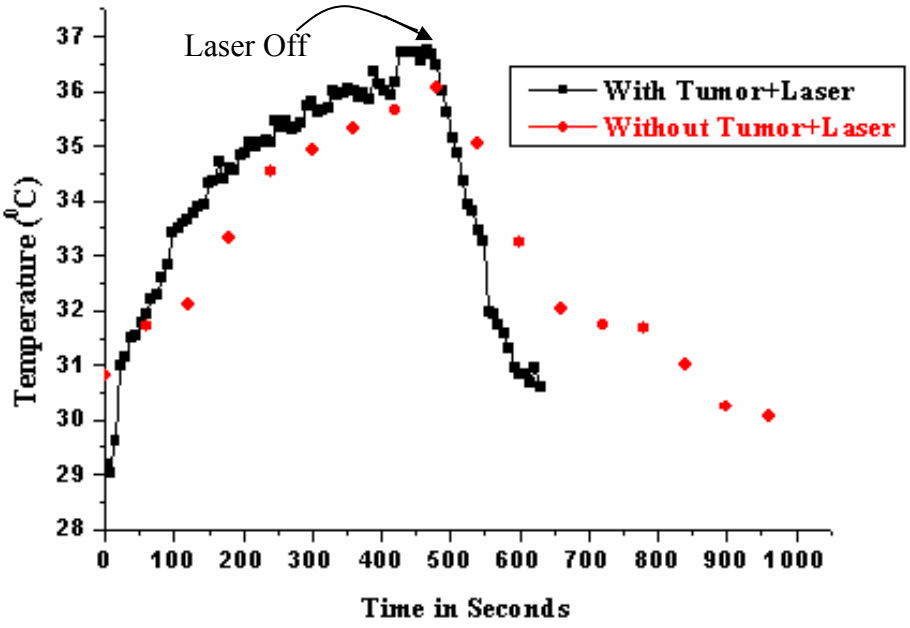

Figure 4.7 Distribution of temperature as a function of time during laser treatment on mice. Red points reveal temperature pattern on a reference mouse, which illustrates the laser-temperature response of live skin without tumor . The black solid curve shows temperature profile on a tumor-bearing mice treated with 805-nm laser (t = 10 min, Power density = 1W/cm^2). The two plots are shown for comparison.

Figure 4.8 shows the comparison of temperature increase with laser power density of 1W/cm^2 on tumor with and without Glycated Chitosan (GC). This experiment was performed to find whether the application of GC affects temperature increase. However, the result shows GC alone does not contribute to temperature increase significantly.

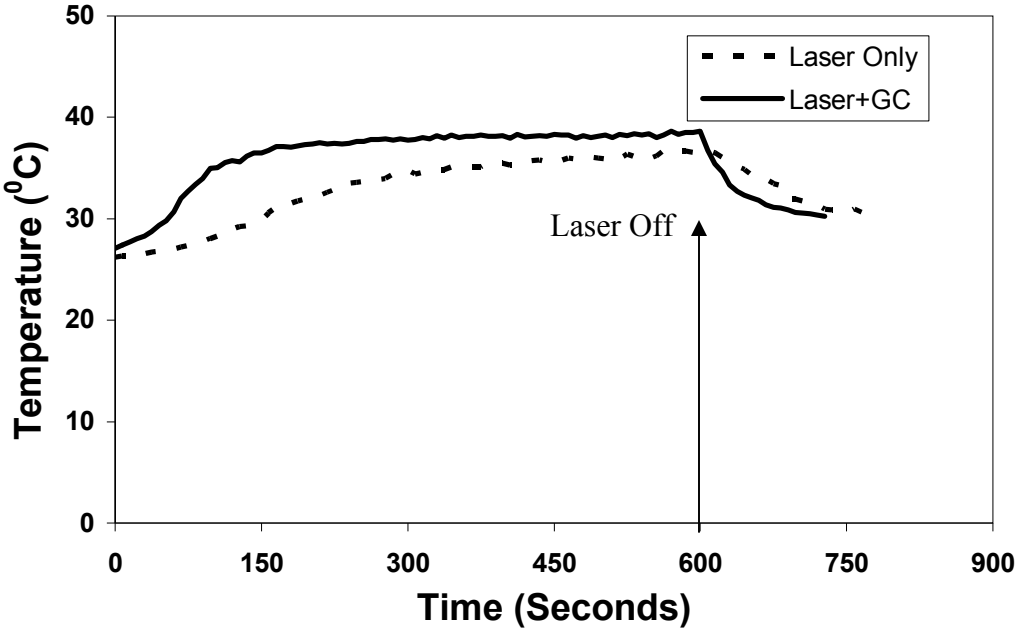

Figure 4.8 Surface temperatures of tumor-bearing mice at the center of the treatment sites during and after laser irradiation. The temperature was measured for the tumor treated by laser only (dotted curve) and by laser after GC injection (solid curve). The laser irradiation duration was 600 seconds, the laser power density was 1W/cm^2, and beam size was 1.5 cm.

Figure 4.9 depicts the temperature increase as a function of time on an ICG injected mouse and on a ICG and GC injected mouse. The contribution to temperature increase by ICG and GC is slightly higher than the contribution by ICG alone. The time interval to acquire images was eight seconds with an energy delivery of 1,000 Joules with a beam of size of 1.5 cm for 10 minutes. A 1W/cm^2 power density was maintained throughout all experiments.

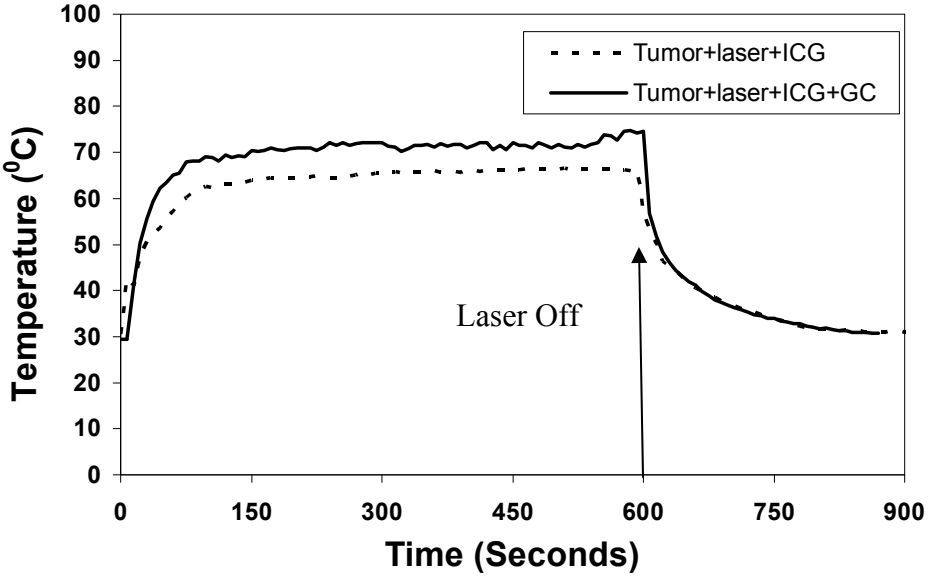

Figure 4.9 Surface temperatures of tumor-bearing mice at the center of the treatment sites during and after laser irradiation. The temperature was measured for the tumor treated by laser after intratumor ICG injection (dotted curve) and after ICG-GC injections (solid curve). The laser power density was 1W/cm^2.

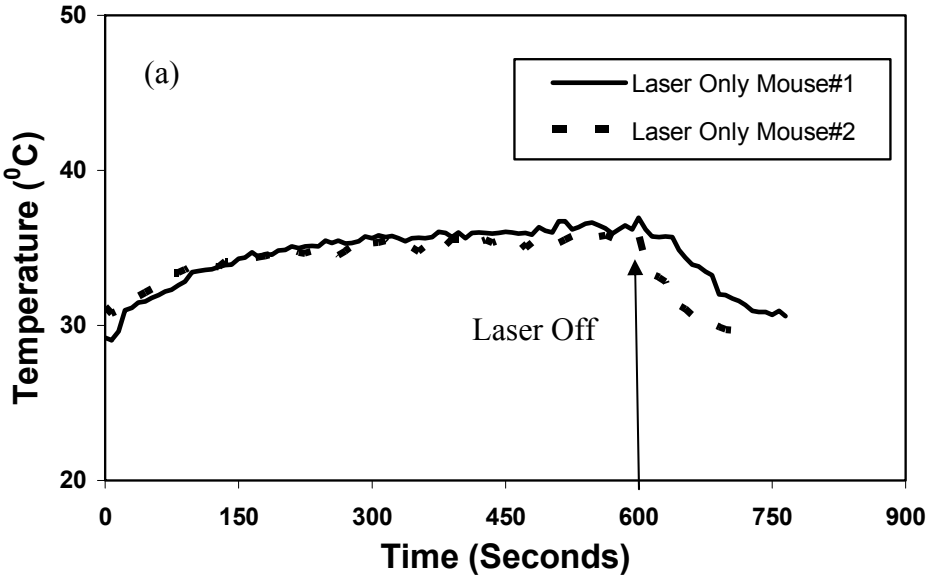

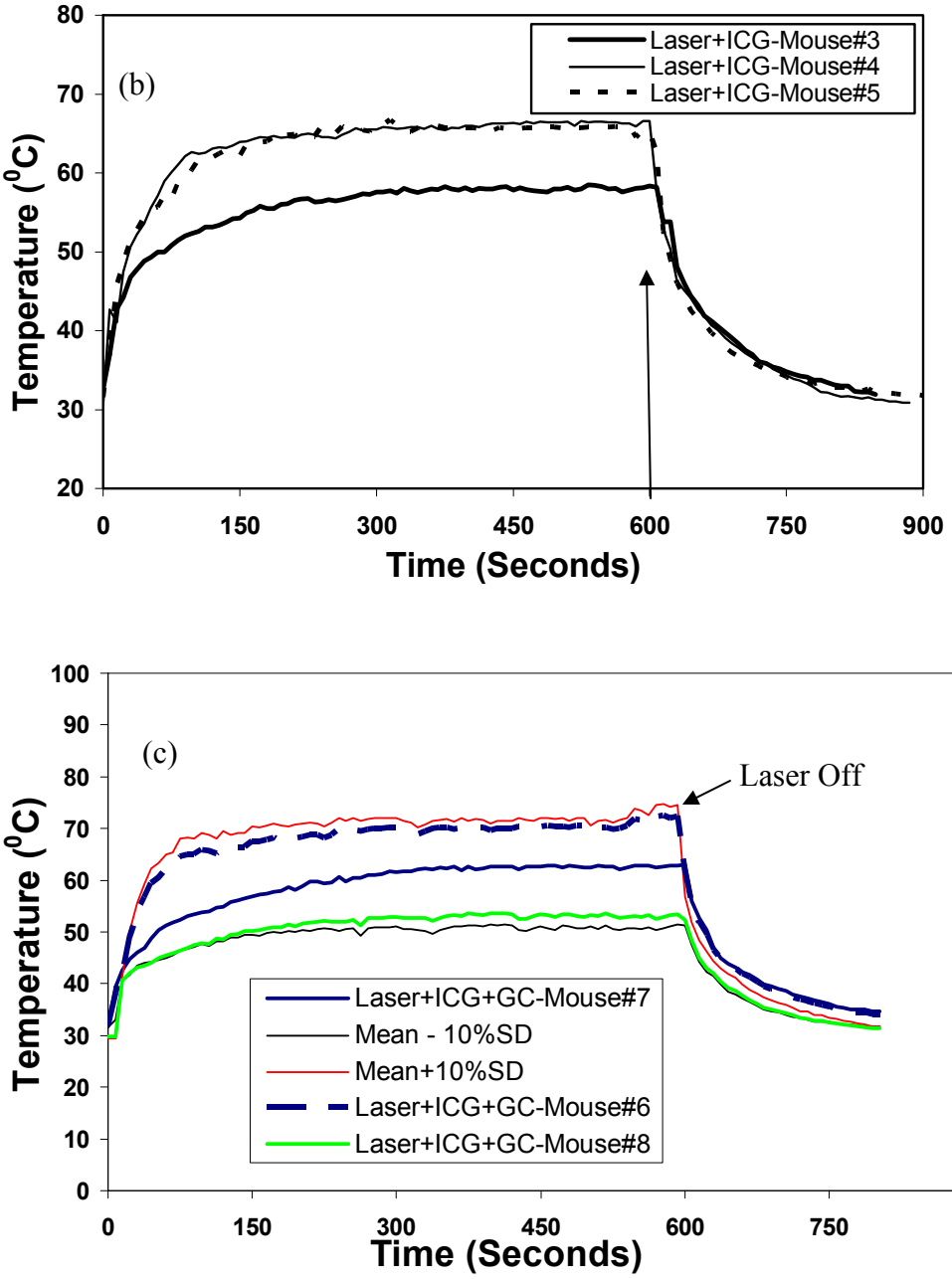

Figure 4.10 Surface temperatures of tumor-bearing mice during and after laser irradiation under different treatment conditions. (a) Two mice were treated with laser light only in which mouse #1 (thick solid curve) had a tumor size of 0.1 cm^3 and mouse #2 (dotted curve) had a tumor size of 0.315 cm^3 at the time of laser treatment. (b) Three mice were treated with an injection of ICG followed by laser irradiation. In this group, mouse #3 (thick solid curve) had a tumor size of 0.192 cm^3, mouse #4 (thin solid curve) had a tumor size of 0.144 cm^3, and mouse #5 (dotted curve) had a tumor size of 0.180 cm^3 at the time of laser treatment. (c) Three mice were treated with the injection of ICG and GC followed by laser irradiation. In this group, mouse #6 (dotted curve) had a tumor size of 0.192 cm^3, mouse #7 (thick solid curve) had a tumor size of 0.245 cm^3, and mouse #8 (green solid curve) had a tumor size of 0.100 cm^3 at the time of laser treatment. The data lie within 10% standard deviation. The tumors were irradiated for 600 seconds with a power density of 1 W/cm^2 and a beam radius of 1.5-cm.

Figure 4.10 shows an increase in temperature with time. The temperature increase varies with different tissue conditions, although the laser power density, dye and GC concentration were maintained the same in all experiments. The results show that with all the conditions keeping the same, the temperature increase depends on an individual mouse. For example, mice with the same concentration of ICG injected into the tumor have a different temperature increase: mouse #1 has an equilibrium temperature of 56 ^{0}C, mouse #2 has an equilibrium temperature of 65 ^{0}C, and mouse #3 also has an equilibrium temperature of 65 ^{0}C. However, the disagreement in temperature increase lies within 10% standard deviation (top and bottom curves in Figure 4.10 (c)). This discrepancy may be due to several reasons: for example, different feeding habits for the individual mice, unequal tumor mass, errors in tumor cells implantation and ICG injection.

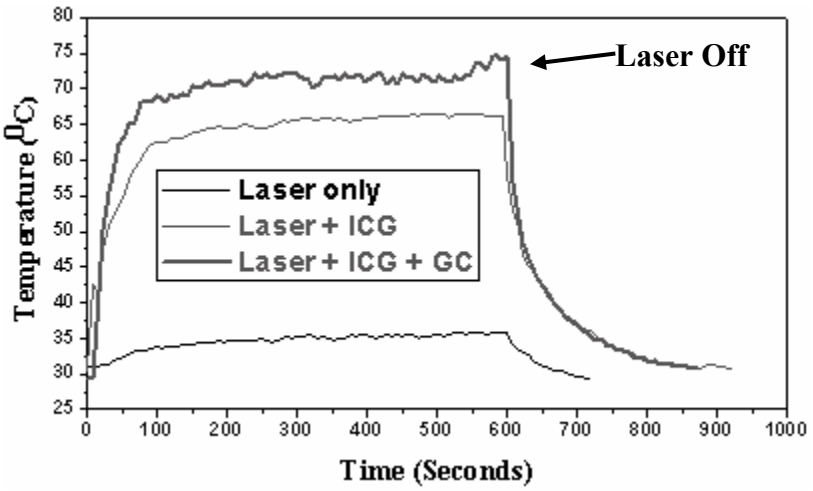

Figure 4.11 Comparison of temperature increase during three different components of laser immuno-therapy. The thin curve is a treatment by laser only, the medium thick-curve is a treatment by injection of 0.25% ICG followed by irradiation of laser, and the thick-curve is a treatment by injecting 0.25% ICG and 1% GC followed by laser irradiation.

Figure 4.11 also shows an increase in temperature with time. In this data, temperature increase in three different-component treatment results are compared. The temperature increase during different treatment conditions shows that the ICG and GC

injection contributes significantly in temperature increase. This implies that the dye enhancement selectively can heat the tumor target. As seen in Figure 4.11, the temperature increase with the laser treatment is only about 5 ^{0}C. However, the temperature increase with ICG and laser combination therapy was about 25 ^{0}C and with the ICG-GC-laser combination therapy, the temperature increased by 30 ^{0}C. This infers that ICG and GC injection potentiates the laser therapy. In both the cases, the tumor temperature attains the cancer cell damage range of 60 ^{0}C - 70 ^{0}C resulting in an increase in mice survival rate (see Figures 5.2, 5.3, and 5.4 of Chapter 5).

4.4.4 Tissue Thermal Damage Analysis

Thermal damage is a one-by-one process in which native biomolecules are activated and denaturized (a lower energy state). The rate of damage formation is proportional to the number of activated biomolecules. Thermal damage exponentially depends on temperature and linearly depends on time of exposure [60]. Thermal damage predicted from the spatial and temporal temperature distribution is given by the Arrhenius damage integral,

$$\Omega(\vec{r}, t) = A \int_0^{t_0} e^{\frac{-E_a}{R\,T(r,t)}} dt \qquad (4.10)$$

where A is a frequency factor (s^{-1}), t_o is the total heating time[s], E_a is activation energy [J/moles] [58] (related to enthalpy and entropy), and R is universal gas constant, 8.31 J/moles.K, T [K] is the absolute temperature and r is the radial position from the axis of the laser spot. The tissue in effect is injured only if $\Omega \geq 0.54$ and the damage is

irreversible for $\Omega \geq 3000$ [58]. The exponential dependence of damage on the inverse of absolute temperature indicates that the temperature required to cause significant damage is quite sensitive to the time of laser exposure. The threshold temperature is the temperature at which the damage parameter Ω is one for a given duration, t_o.

$$T_{th} = \frac{E_a}{R[\ln(t_0) - \ln(1/A)]} \qquad (4.11)$$

Below this threshold temperature, the rate of damage accumulation is negligible and above the threshold temperature, the damage increases rapidly by the exponential nature of the damage function. The estimates of A and E_a can be made by making a small change in temperature on the sample due to the temperature sensitivity of the damage integral. The idea is to expose the specimen with a constant temperature heat source such as laser light for a desired time interval. For a time invariant model with Ω = 1, the integral in Equation 4.10 simplifies to

$$\ln(t_0) = (\frac{E_a}{R})\frac{1}{T} + \ln(\frac{1}{A}) \qquad (4.12)$$

The Arrhenius plot of equation (4.12) gives the values for the parameters E_a and A.

4.4.4.1 The Arrhenius Plot

Laser tissue damage is analyzed using the Arrhenius equation at a point r = 2 mm from the axis of the laser beam on the treatment region. The Arrhenius plot of Equation 4.12 using the saturation temperature data in our experiment are shown in Figure 4.11 for different times. The temperature and corresponding time data were plotted as ln(t) versus

inverse temperature, T^{-1}. The slope of the graph was used to determine the activation energy, E_a and the intercept to obtain the inverse time factor, A (Figure 4.12). In our calculation, the value of A was obtained to be 2.22 x 10^{89} (± 8.36 x 10^{88}) s^{-1} and the value of E_a obtained was 5.883 x 10^5 (± 2.8 x 10^4) $Jmol^{-1}$

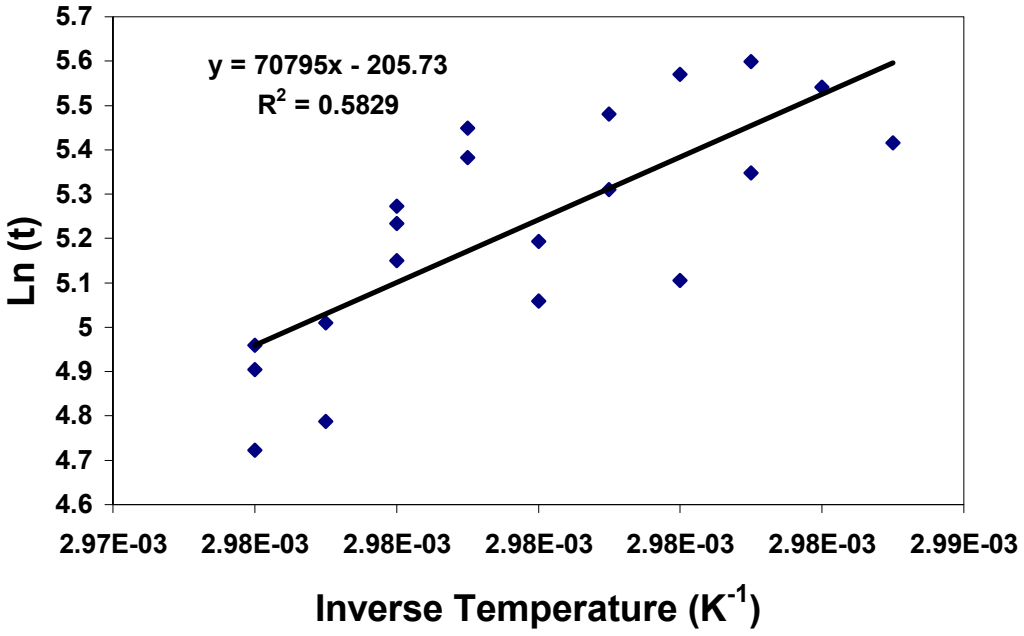

Figure 4.12 The Arrhenius plot for the experimental temperature obtained from mice laser-treatment. Coefficients A and E_a are determined based on linear fit of data obtained from the saturation temperature and time from Figure 4.10. The threshold thermal damage, Ω, was taken to be unity. The onset of plateau on the temperature-time graph in Figure 4.10 is determined from the abrupt change in slope of the curves at a time point of 175 seconds. Results agree with the in vitro studies.

This result agrees with the previous studies [59]. Setting the damage threshold as ≤ 0.54 and permanent damage at ≥ 3000, it is clearly shown that five (mouse # 1, 2, 3, 4, and 6) out of six mice have tissue damage started before temperature saturates. The time of irradiation was 95.5 s, 112.5 s, 97.5 s, 67.5 s, 45 s, and 82.5 s on respective mice. Mouse #6 has its permanent tissue damage even before its saturation temperature. However, in mouse #5, the tissue damage has not even started at its saturation temperature.

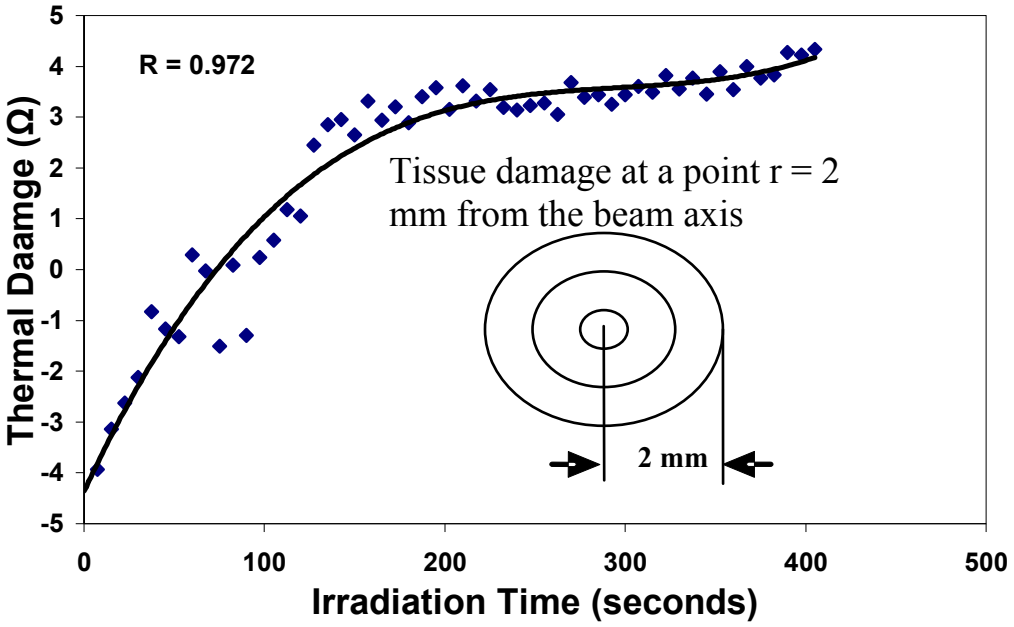

Figure 4.13 The tissue damage, Ω, calculated from Equation 4.10 as a function of time at a position, r = 2 mm from the axis of the laser beam on the treatment site. As shown at the inset is a schematic damage area. A polynomial fit (solid curve) shows how the damage propagates. The damage starts at, Ω = 0.54 at a time of 75 seconds and the damage becomes irreversible above 3000.

The temperature-time data obtained from the images of mice during dye-enhanced laser treatment are used to calculate the damage parameter. Thermal damage, Ω, versus time plot is shown in Figure 4.13. A polynomial fit on the data shows the nature of the damage. The damage saturates at 175 seconds after the onset of laser irradiation. The onset of the plateau temperature is determined from a point at which the abrupt change in slope of the temperature-time curve occurs.

As the temperature at the plateau region is almost invariant with time during laser exposure, the damage integral function becomes independent of time and space for a radial fixed point 2 mm from the beam axis. The damage threshold is calculated for a value of Ω a unity (Figure 4.13). Below threshold, the rate of damage accumulation is

negligible and above the damage threshold the damage accumulation increases rapidly shown by the exponential nature of the damage function in Equation 4.10. The onset of damage saturation is at about 175 seconds. Above $\Omega = 3000$, damage becomes irreversible and a scar is formed on the treatment site. Sufficiently below the value of $\Omega = 3000$, a number of activated biomolecules make a transition to their native state.

The high standard deviation in our results is caused by the inaccuracy in measurement of the temperature due to breathing at the time of image acquisition. This causes the change of position at the point of consideration on the mouse and hence there is an error in the temperature measurement. However, results agree with the in vitro studies [59-61]. Since biological tissues are inhomogeneous, there are random fluctuations in tissue characteristics, and in part due to the difficulty of resolving small temperature differences. As a result, the prediction of the observed damage boundaries in long exposure experiments is difficult. However, in small spot size exposures in a relatively short duration, the experimental results compare reasonably with the theoretical predictions. These results can be extremely helpful in thermal therapies for cancer treatments.

4.5 Conclusion

The surface and volume temperatures during laser treatment are crucial for optimal outcome. It has been demonstrated that treatment parameters such as tissue conditions and laser parameters can be adjusted to improve the effectiveness in photothermal therapy of cancer treatment. In this study, it is further demonstrated that the computational and experimental results for surface temperature increase agree well. However, the accuracy of the result depends on an individual biological condition. The infrared thermal imaging technique is suitable for its adjunctive use during treatment. The light transport and heat diffusion model for the simulation of laser tissue interaction are robust and can predict the thermal response of the tissue during treatment.

The temperature profiles shown in Figures 4.8 to 4.11 indicated the feasibility of systematic control of the treatment parameters to achieve the thermal outcome within the desired range. However, the different temperature profiles shown in Figure 4.10 present challenges in controlling the photothermal therapy, due to different physiological conditions and anatomical structures. In laser immunotherapy [15, 16], where the photothermal reactions serve as a precursor of host immunological responses, a wide range of treatment parameters could affect the outcome of treatment. Therefore, further studies are needed to correlate the thermal outcome and immunological responses in order to monitor the laser immunological treatment of cancer.

Chapter 5

Laser-Immunotherapy for Primary Tumors and Metastases

5.1 Introduction

Cancer is a disease that involves dynamic changes in the genome. It is a type of genetic disease in which not only one, but several mutations are required. Each mutation generates a disorder of genome base pairs and geometrical multiplication of new cells associated with a gradual increase in tumor size causing malignancy [62]. Generally, three to six such mutations are required to complete one cancer growth cycle [63]. Significant advances have been made in the molecular and cellular knowledge of cancer but very little is understood about the physiology underlying human carcinogenesis. Efforts are underway to transform recent molecular knowledge in an understanding of the complex phenomena existing in genes, cells, tissues, organs, apparatuses and organism [64]. Carcinogenesis depends on a number of variables such as growth inhibitory signals, apoptosis, cell proliferation and angiogenesis, metastases, which make it one of the most complex phenomena in biology [64-65].

A number of treatment modalities such as radiation therapy, chemotherapy, and surgery have been developed in the past and are still in use for different types of cancer

treatment. Some newly emerging modalities such as photodynamic therapy and gene therapy are also under clinical trial. An ideal treatment modality for the treatment of metastatic tumors should be able to eradicate the primary tumor and bring out a tumor selective response leading to the elimination of metastases while providing long-term tumor resistance [16]. Induction of the immune response in the host is the most effective cancer treatment mechanism. Such a response not only cures detected and treated primary tumors but also affects the undetectable metastases at distant sites [16, 66].

Glycated Chitosan (GC) has been used as an immunostimulant for cancer treatment in laser immunotherapy [66]. The function of GC is to enhance the host immune response after direct cancer cell destruction by a selective laser photothermal interaction. In this study, we used the laser-immunotherapy to treat mammary tumors in mice. The survival of treated animals were compared with untreated control animals. The experimental results of this study agree previous studies [67-68], showing that immunoadjuvants may play an active role in laser-related metastatic cancer treatment and that GC significantly enhances the efficacy of the treatment.

5.2 Materials and Method

5.2.1 Components of Laser Immunotherapy

Laser immunotherapy consists of three main components: a near-infrared laser (DIOMED 25, Diomed, Cambridge, UK), a laser absorbing dye indocyanine green (Becton Dickinson, Cockeysville, MD, USA) and an immunoadjuvant Glycated Chitosan (a biopolymer prepared by incubating an aqueous suspension of Chitosan with a 3-fold excess of galactose and subsequent stabilization by borohydride reduction of the mixture of Schiff bases and Amadori product) [66].

5.2.2 Tumor Model

The transplantable EMT6 mammary tumor model in BALB/c female mice was used in our experiments. The mice were purchased from Harlan Sprague Dawley Co. (Indianapolis, Indiana) at the age of 5-6 weeks and weight of 15-25 grams. All the procedures in the animal experiments are in compliance with protocol approved by the Institutional Animal Care and Use Committee (IACUC).

The tumor cells were stored frozen, grown in tissue culture, and 10^6 viable cells were implanted subcutaneously per mouse via a 27-gauge hyperdermic needles on dorsal part of the mice. Primary tumors were apparent about 7-10 days after the tumor cell implantation. In our experiment, immunoadjuvant glycated chitosan (GC, 200 μL, 1%) was injected intratumorally 24 hours prior to the laser treatment. ICG solution (200 μL, 0.25%) was injected intratumorally 30 minutes before the laser treatment.

5.2.3 Treatment Procedure of Laser Immunotherapy

In this experiment an 805-nm laser and ICG were used for photothermal interaction in combination with GC for tumor treatment. Mice tumors were treated with combination of laser-ICG-GC and immunological studies were performed. The treatment was performed 10 days after tumor cell implantation when the tumors appeared and tumor volume in most of the mice became 0.12 cm^3. Prior to treatment, mice were anesthetized using 0.65 ml xylazine mixed with 0.87ml ketamine and following anesthesia overlying hair was clipped with a #40 clipper blade. The ICG and GC were injected at the center of the tumors and the tumors then were irradiated by the laser with power density 1 W/cm^2 for 10 minutes equivalent to an energy delivery of 1000 Joules per mouse.

In the mouse model, four groups of mice were treated to investigate the role of different tissue conditions in the activation of immune response of the body system. The first group of 4 mice was tumor-bearing controls. The second group of 12 mice was tumor-bearing mice treated only with laser irradiated at power density of 1 W/cm^2 for 10 minutes. The third group of 12 mice was tumor-bearing mice treated with laser and an intratumor injection of 200 μL of 0.25 % ICG, the fourth group of 12 mice was a tumor-bearing mice treated with an intratumor injection of 200 μL of 0.25 % ICG and 1%GC followed by laser irradiation, and fifth group of 12 mice was treated with intratumor GC injection only.

5.2.4 Post Treatment

After the laser treatment, the mice were housed in individual cages. The treated mice were observed daily and the dimensions of the tumor were measured weekly. The

average survival time of each treatment group was compared with that of the untreated control group as explained in the result section below.

5.3 Results

In this study, Kaplan-Mayer plots were plotted from the data collected weekly for all different treatment groups.

5.3.1 Survival Study

The mice survival data observed after treatment using laser only and GC only are shown in Figure 5.1. The survival time were compared with the control group. As shown in Figure 5.1, the mice treated with the laser-only group died with an average survival time closer to that of control group.

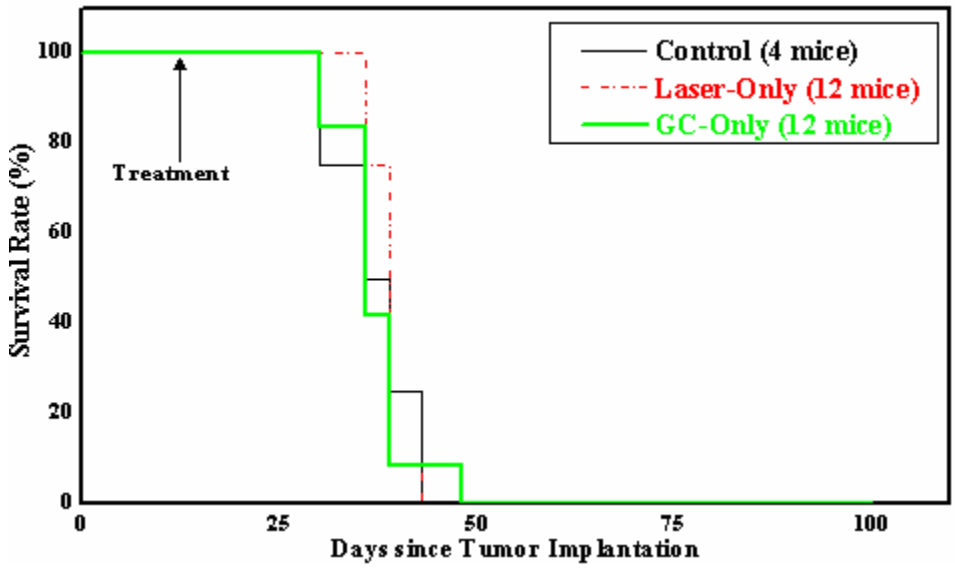

Figure 5.1 Survival study of tumor-bearing mice treated by one-component of laser immunotherapy. The thin solid curve represents survival rates for control mice. The red thin dash-dotted curve represents survival rates for mice treated with 805-nm laser only with laser power density of 1 W/cm^2 for 10 min. The green thick solid curve represents survival rates for mice treated with intratumor injection of 200 μL of solution of 1% GC.

The mouse survival rate in the group treated by the two-component combination, a laser-ICG group is shown in Figure 5.2. This was focused on the effects of laser with dye enhancement in the treatment of cancers.

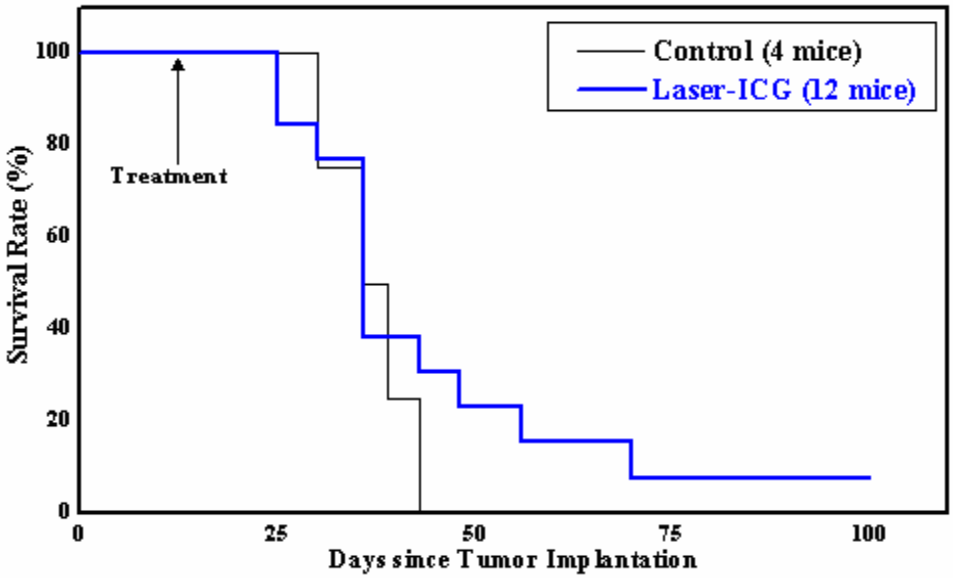

Figure 5.2 Survival study of tumor-bearing mice treated by two-component of laser immunotherapy. The thin solid curve represents the survival rates for control mice. The thick blue color solid curve represents survival rates for mice treated with intratumor injection of 200 μL solution of 0.25% ICG followed by laser irradiation at power density 1 W/cm^2 for 10 min.

As shown in Figure 5.2, the mice treated with laser-ICG combination group survived with an average survival time about 100 days, which is longer than the control mice. However, the number of mice that survived is very small. Therefore, there requires more sets of experiments to obtain better result.

The results using standard treatment procedure of laser immunotherapy (laser-ICG-GC combination) are shown in Figure 5.3.

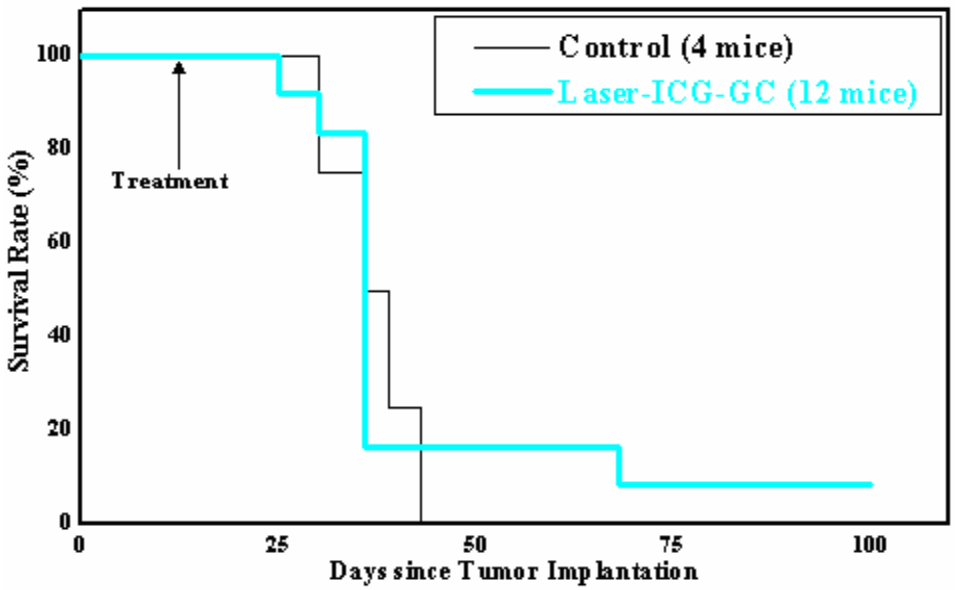

Figure 5.3 Survival studies of tumor-bearing mice treated by all three components of laser immunotherapy. The thin solid curve represents survival rates to control mice. The cyan color solid curve represents survival rates for mice treated by the laser-ICG-GC combination. The mice were injected with 200 µl of solution of 0.25% ICG and 200 µl of solution of 1% GC followed by laser irradiation at power density 1 W/cm^2 for 10 min.

As shown in Figure 5.3, the mice treated with laser-ICG-GC combination group survived with an average survival time longer than the control mice. However, only a small fraction survived for longer time. All the mice in this group were treated only with 805-nm laser at a laser power density of 1 W/cm^2 for 10 minutes.

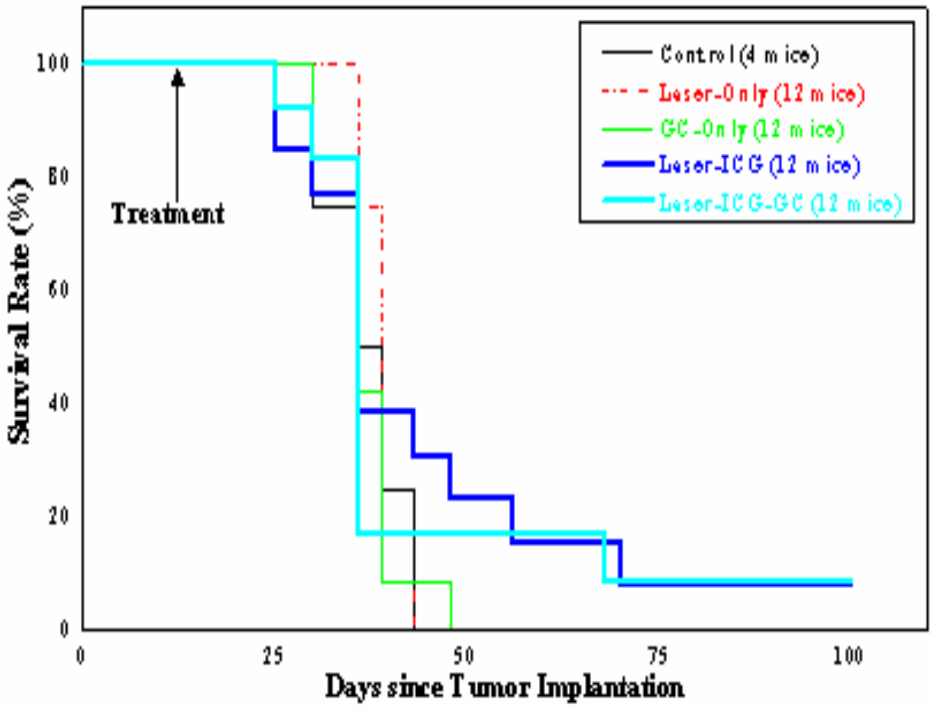

Figure 5.4 Survival studies of tumor-bearing mice treated by all components of laser immunotherapy. The thin solid curve represents survival rates for control mice. The red dash-dotted curve represents survival rates of mice treated with 805-nm laser only at laser power density of 1 W/cm^2 for 10 min. The green solid curve represents survival rates for mice treated with intratumor injection of 200 µl of solution of 1% GC. The dashed blue curve represents the survival rates for mice treated by the laser-ICG-GC combination. The cyan color solid curve represents survival rates for mice treated with intratumor injection of 200 µl of solution of 0.25% ICG followed by laser irradiation at power density 1 W/cm^2 for 10 min.

The comparison of survival rates for one-, two- and three-components of laser immunotherapy are shown in Figure 5.4. The results are inspiring to further study. However, this study alone can not provide the best information for the increased life time of the mice. Because the number of long time survived mice is small.

5.4 Discussion and Conclusion

The success of laser therapy can be attributed to several factors, such as even distribution of photon absorption enhancing dye and immune-stimulants, laser energy application, and more importantly the complicated photon migration inside the inhomogeneous tissue media. Combination therapy using immunoadjuvants is becoming popular in cancer treatment over other conventional methods such as radiation therapy, photodynamic therapy, and chemotherapy. When used appropriately, the immunoadjuvants can significantly improve the efficacy of cancer treatment by stimulating the host immune system. Laser immunotherapy targets not only primary tumor mass but also induces an anti-tumor immunity to fight against the metastases.

In the treatment of metastatic breast tumor (EMT6) in mice, the results can be divided into two categories: first with long-term survival mice and second short-term survival mice. Mainly two groups treated with laser-ICG-GC combination and laser-ICG combinations belong to the first category. In addition to that, some mice from GC-only group and laser-only group were also survived longer times falling into first category (see the thin solid line and dashed curve in Figure 5.4). In this category, 1 mouse in each of the groups (laser-only, GC-only, and laser-ICG) survived for longest time. However, a number of mice in laser-ICG-GC group survived longer than the control mice. All together, 6 mice out of 48 treated mice, (1 from control group, 2 from laser-ICG-GC group and 3 from laser-ICG group) did not develop tumors. This may be likely due to error in tumor cell injection or their body immune system may be strong enough to fight against the injected tumor cells. The laser-ICG-GC combination shows better survival

rate as relatively larger number of mice survived in this group for relatively longer duration.

In the second category, mice survived for a relatively short time. Two mice died after “day one” treatment (1 from laser-ICG-GC group, 1 from laser-ICG group). The reason for their death is unknown. In conclusion, although the laser-ICG-GC combination treatment results are better than other combination groups, there requires further study for the better treatment outcome in order to investigate whether the model can predict a large number of mice that can survive for longer time.

Chapter 6

Summary and Further Recommendations

This work focuses on the laser-immunotherapy for the treatment of primary and metastatic tumors, specifically on tissue temperature measurement using different temperature probes. Prior to the experiments, Monte Carlo method for the light transport in tissue and a finite difference method for the solution of heat diffusion equation were performed to estimate the laser dose parameters, concentration of dye and the concentration of immunoadjuvant. The specimens used for this investigation purpose were gelatin phantom, rats and mice.

Prior knowledge of predicting the induced tissue damage during treatment is important for several reasons. The thermal imaging and dose calculation can increase the level of safety by providing information to avoid damage to the surrounding normal tissue. This reduces the treatment time and minimizes the risk of causing thermal scars in the overlying tissue. During laser-induced thermotherapy, it is important to have the knowledge of temperature in the target tissue. At this point, the non invasive temperature measurement probes are valuable. Monte Carlo method can effectively simulate absorption and scattering of light in tissue, hence providing the spatial distribution of photon absorption. Temperature distribution and tissue response in the target and surrounding tissue depends on the photon absorption and heat transfer in the tissue during

laser irradiation. Magnetic resonance imaging thermometry (MRT) and infrared thermography (IRT) were the methods used for the measurement of temperature in the biological tissues during the treatment of primary and metastatic tumors. Thermal imaging helps estimate the laser-dose for the application to cancer treatment. The prediction of the laser induced tissue damage during cancer treatment is important for optimal treatment outcome.

In MR imaging, paramagnetic susceptibility has a significant role in determining chemical shift in biological molecules. Many researchers have used water proton chemical shift (the diamagnetic contribution to chemical shift). In this study, effect of paramagnetic materials such as iron in hemoglobin on chemical shift has been discussed along with the water-proton chemical shift. MRT method in the in-vivo temperature monitoring during laser-tumor treatment has been used in this study. Monte Carlo method for the light transport in tissue and a finite difference method for the solution of heat diffusion equation were performed to estimate the laser dose parameters, concentration of dye and immunoadjuvant. The specimens used for this investigation purpose were a gelatin phantom, rats and mice. The temperature profiles in this study agree with the simulation results. This study shows that we have better temperature control over treatment parameters by changing the target tissue conditions. The survival study in mice shows that the selective heating of the target tissue using combination therapy may increase the survival rate.

Further Recommendations

It has been shown in an in vivo study that near infrared laser light and silica-gold nanoshells as an absorption enhancing agent can increase the average maximum temperature sufficient to induce an irreversible damage to the tumor cells [13]. The efficacy of the treatment can be further increased by using gold nanoshells. This is because these particles can produce oscillating electrons on their surface with NIR light causing resonance with the plasma surface, hence greater light absorption. In addition, heat deposition rate and surface evaporation kinetics with respects to the temperature change requires more detailed study in the future.

The disadvantage of laser induced thermal therapy is that for a relatively high temperature gradient along the beam axis, it creates a nonuniform thermal distribution through the treated tumor volume. It is also difficult to shape the thermal lesion to match the tumor without moving the fiber. Clinically, the movement of the optical fiber is not desirable. Therefore, multiple fibers are required to irradiate the tumor through different angles to provide uniform thermal delivery. This provides a better method to uniform heating of primary tumor.

MR-guided thermal treatment requires integration of therapeutic devices with the imaging system because of the limited work space for clinician. Most importantly, we are entering to a new area of combined diagnostic and therapeutic applications. There are still unresolved problems in manufacture of devices that integrate diagnostic and therapeutic applicators for clinical trial. The future of laser treatment depends not only on the improvement in the real-time temperature monitoring but also on the possibilities to improve the control of the tissue effect, to increase the treated volume at the treatment

site, and to achieve tumor cell death without carbonization. In addition, the infrared thermography can lead to the detection of breast and skin cancers (70).

BIBLIOGRAPHY

1. Cancer Facts and Figures, 2007. American Cancer Society. Website: http://www.cancer.org/downloads/STT/CAFF2007PWSecured.pdf

2. Liota L.A. and Stetler-Stevenson. Principles of Molecular Cell Biology of Cancer: Cancer Metastases, in Cancer: Pinciples and Practice of Oncology, Edited by Vincent T. DeVita, Samual Hellman and Steven A Rosenberg, JB Lippincott Co., Philadelphia: 134-149, 1993.

3. Castano A.P., Tatian N.D., Michael R.H. Mechanism of Photodynamic therapy: part-three. Photodiagnosis and Photodynamic therapy 2: 91-106, 2005.

4. Chen, W.R., Robert, L.A., Sean, H., Dickey, D.T., Bartels, K.E. and Nordquist, R.E. Chromophore-enhanced laser tumor tissue photothermal interaction using an 805 nm laser, Cancer letters 88:15-19, 1995.

5. Chen, W.R., Robert, L.A., Higgins A.K, Bartels, K.E., Nordquist, R.E. Photothermal effects on mammary tumors using indocyanine green and an 808-nm diode laser: an invivo efficacy study. Cancer letters 98:169-173, 1996..

6. Jampel, H.D., Duff G.W., Gershon, R.K., Atkins, E., Durum, S.K. Fever and Immunoregulation: Hyperthermia augments the primary in vitro humeral immune response, J. Exp. Med.157: 1229-1238, 1983.

7. Anghileri, L.J, Robert, J. Hyperthermia in Cancer Treatment, Boca, Raton FL: CRC press, 1986.

8. Hamblin, M.R, Castano, A.P., and Morz, P. Combination immunotherapy and Photodynamic therapy for cancer. Proc. of SPIE vol. 6087: 608702-1-12, 2006.

9. Crochet, J.J., Gnyawali, Surya C., Chen, Y., Lemley, E.C., Bartels, K.E., Liu, H., Chen, W.R. Temperature Distribution in Selective Laser-Tissue Interaction. J. Biomed. Optics 11(3):0340 31-1-10, 2006.

10. Field, S.B., Morris, C.C. The Relationship between Heating Time and Temperature. Radiother. Oncol.1(2):179-186, 1983.

11. Markus, R.F. Lasers more than a cosmetic tool. J. Dermatological Treatment 11:117-124, 2000.

12. Chen, W.R., Adams R.L., Higgins A.K., Bartels, K.E., and Nordquist, R.E. "Photo-thermal effects on murine mammary tumors using indocyanine green and 808 nm diode laser: an in vivo efficacy study." Cancer Lett. 98:169–173, 1996.

13. Hirsch, L.R., Stafford, R.J., Bankson, J.A., Sershen, S.R., Rivera, B., Price, R. E., Hazle, J.D., Halas, N.J., and West, J.L. "Nanoshell-mediated near-infrared thermal therapy of tumors under magnetic resonance guidance," Proc. Natl. Acad. Sci. U.S.A100:13549–13554, 2003.

14. Dewhirst, M. W., Conner, W. G., and Sim, D.A. "Preliminary result of phase III trial of spontaneous animal tumors to heat and/ or radiation early normal tissue response

and tumor volume influence on initial response," Int. J. Radiat. Oncol., Biol., Phys. 8:1951–1962, 1982.

15. Chen, W.R., Adams, R.L., and Nordquist, R.E. "Laser-photosensitizer assisted immunotherapy: A novel modality in cancer treatment," Cancer Lett. 115:25–30, 1997.
16. Chen, W.R., Zhu, W.G., Dynlacht, J.R., Liu, H., and Nordquist, R.E. "Long-term tumor resistance induced by laser photo-immunotherapy," Int. J. Cancer 81:808–812, 1999.
17. Wang, L. and Jacques, S. Monte Carlo modeling of light transport in multi-layered tissues in standard C, http://biomed.tamu.edu/~lw or http://ece.ogi.edu/omlc. , 1998.
18. Wang, L. H., Nordquist, R.E., and Chen, W.R. "Optimal beam size for light delivery to absorption-enhanced tumors buried in biological tissues and effect of multiple beam delivery: a Monte Carlo study," Appl. Opt. 36:8286–8291, 1997.
19. Wang, L. and Jacques, S., "Monte Carlo modeling of light transport in multi-layered tissues," Laser Biology Research Lab., The Univ. Texas M.D. Anderson Cancer Center http://oilab.tamu.edu/mcr5/Mcman.pdf., 1995.
20. Welch, A.J., van Gemert, M. J. Optcal-thermal response of laser-irradiated tissue, Plenum Press, New York, 1995.
21. Adam P. Finite difference solutions of the heat equation, MIT open courseware, (http://ocw.mit.edu/NR/rdonlyres/Nuclear-Engineering/22-00JIntroduction-to-

Modeling-and-SimulationSpring2002/55114EA2-9B81-4FD8-90D5-5F64F21D23D0/0/lecture_16.pdf), 2002.

22. Ishihara, Y., Calderon, A., Watanabe, H., Okamoto, K., Suzuki, Y., Kuroda, K., and Suzuki, Y. A precise and fast temperature mapping using water proton chemical shift. Magn. Reson. in Medicine 34: 814-823, 1995.
23. Quesson, B., Jacco, A.Z., Chrit, T.W. Magnetic resonance temperature imaging for guidance of thermotherapy, J. Magn. Reson. Imaging: 12:525-533, 2000.
24. Hindman, J.C. Proton resonance shift of water in the gas and liquid state, Journal of chemical physics 44(12):4552-4592, 1966.
25. Saher, M. M., Stephen, J.D., Jia-Hong G., Randolph D.G. Temperature mapping of laser-induced hyperthermia in an ocular phantom using magnetic resonance thermography. J. Biomed. Optics 9(4): 711–718, 2004.
26. Young, I.R., Jeffery W.H. Modeling and Observation of temperature changes in vivo using MRI. Mag. Reson. in Medicine 32:358-369, 1994.
27. Viola, Rieke., Karl, K., Vigen, G. S., Bruce L.D, Pauly J.M. and Kim Butts Referenceless PRF shift thermometry. Mag. Reson. in Medicine 51:1223-1231, 2004.
28. De Poorter, J. Non-invasive MRI thermometry, with the proton resonance frequency method: study of susceptibility effects, Magnetic Resonance in Medicine 34: 359-367, 1995.
29. Charles K. Introduction to Solid State Physics, John Wiley & Sons, Inc.,7th Ed. p490, 1996.

30. Van Vleck, J. H. The theory of electric and magnetic susceptibilities, Oxford University Press, p25, 1932.
31. Weast, R. C., Astle, M.J. CRC handbook of chemistry and physics, CRC press, Boca Raton, FL, 1981.
32. Janowski, T. and Wolinski, K., Relationship between magnetic shielding and magnetizability, Journal of Chemical Physics 117(5), 2002.
33. Schenck J. F. Biological effects and safety aspects of nuclear magnetic resonance imaging and spectroscopy, Ann. N. Y. Acad. Sci. 649: 291, 1992.
34. Kevin, P.N., Hall, L.D., Bows, J.R., Michael Hale, Patrick, M.L. Three-dimensional MRI mapping of microwave induced heating patterns. Journal of Food Science& Technology: 34:305-315, 1999.
35. De Poorter, J., De Wagter, C., De Deene, Y., Thomsen, C., Stahlberg, F. and Achten, E. Proton resonance frequency shift method compared with molecular diffusion for quantitative measurement of two-dimensional time dependent temperature distribution in a phantom. Journal of Magnetic Resonance Imaging B103:234-241, 1994.
36. Dikinson, R.J., Hall, A.S., Hind, A.J. and Young, I.R. Measurement of changes in tissue temperature using MR Imaging. Journal of Computer Assisted Tomography 10(3):468-472, 1986.

37. Olsrud, J., Ronnie, W., Sara, B., Annika, M.K. MRI thermometry in phantoms by use of the proton resonance frequency shift method: application to interstitial laser thermotherapy. Phys. Med. Biol. 43: 2597-2613, 1998.

38. Michel, P., Martine, M.G., Pascale, F.P., Pierre, P., Jean, P.C., Delacretaz, G., Lopez, F.M., and Guilhem, G. MRI thermometry in laser-induced interstitial thermometry. Lasers in Surgery and Medicine 32:54-60, 2003.

39. Florian, B., Mattner, J., Stehling, M.K., Ulrich, M.L., Peller, M., Ralf, L., Jurgen, W. Non-invasive temperature mapping using MRI: comparison of two methods based on chemical shift and T1-relaxation. Magnetic Resonance Imaging 16(4):393-404, 1998.

40. Peters, R.D., Hinks R. S., and Henkelman, R. Mark. Heat source orientation and geometry dependence in proton-resonance frequency shift magnetic resonance thermometry. Mag. Reson. in Med 41: 909-918, 1999.

41. Moser, E., Winklmayr, E., Holzmuller, P., and Krssak, M. Temperature and pH-dependence of proton relaxation rates in rat liver tissue. Magnetic resonance imaging 13(3): 429-440, 1995.

42. David, H.G. and Gore, J.C. Temperature dependence of magnetization and relaxation, J. Magnetic Resonance 172: 133-141, 2005.

43. MacFall, J.R., Prescott, D.M., Charles, H.C., Samulsk, T.V. Proton MRI phases thermometry in vivo in canine brain, muscle and tumor tissue. Med. Phys 23(10): 1775-1782, 1996.

44. Cerdonio, M., Silvia, M., Stefano, V., Young, A. Variability of the magnetic moment of carbon monoxide hemoglobin from crap, Biophysics, Proc. Natl. Acad. Sci. USA 77(3): 1462-1465, 1980.

45. Cherrick, R.G., Stein, S.W., Leevy, C., Davidson, C.S. Indocyanine green: Observations on physical properties, plasma decay, and hepatic extraction. J. Clin Invest, 39: 592-600, 1960.

46. Bednarski, M.D., Lee, J.W., Callstrom, M. R. In vivo target-specific delivery of macromolecular agents with MR-guided focused ultrasound. Radiology 204:263-268, 1997.

47. Barnes, B.R., Diagnostic Thermography. Applied Optics, 7 (9): 1673-1685, 1968.

48. Xie, W., McCahon, P., Jakobsen, K. and Paris, C. Evaluation of the ability of digital infrared imaging to detect vascular changes in experimental animal tumors. Int. J. Cancer 108: 790-794, 2004.

49. Michal, Z. Breast cancer diagnostics using IR camera, PhD thesis

50. Takashi, M., Ozaki, M., Nishiyama, T., Imamura, M., Kumazwa, T. Comparison of infrared thermometer with thermocouple for monitoring skin temperature. Crit Care Med 28(2): 532-535, 2000.

51. Bryan, F.J. A Reappraisal of the use of infrared thermal image analysis in medicine. IEEE Transaction on Medical Imaging 17(6): 1019-1027, 1998.

52. Orenstein, A., Kostenich, G., Tsur, H., Kogan, L., Malik, Z. Temperature monitoring during photodynamic therapy of skin tumors with topical 5-aminolevulinic acid application. Cancer Letters 93: 227-232, 1995.

53. Partovi, F., Izatt, J.A., Cothren, R.M., Kittrell, C., Thomas, J.E., Strikwerde, S., Kramer, J.R., Feld, M.S. A Model for thermal ablation of biological tissue using laser radiation. Lasers in Surgery and Medicine 7: 141-154, 1987.

54. Hildebrandt, B., Wust, P., Ahlers, O., Dieing, A., Sreenivasa, G., Kerner, T., Felix, R., Riess, H. The cellular and molecular basis of hyperthermia. Crit. Rev. Oncol. Hamatol. 43: 33-56, 2002.

55. Dereniak, E.L., Crowe, D.G. Optical radiation detectors. John Wiley & Sons., 1984.

56. Prahl, S. Optical absorption of indocyanine green (ICG), http/omlc.ogi.edu/spectra/icg/index.html.

57. Lab mannual, Prism DS infrared camera

58. Henriques, F. C. Studies of thermal injury V. Archieves of Pathology 43: 489-502, 1947.

59. Orgill, D.P., Porter, S.A., Taylor, H.O. Heat injury to cells in perfused systems. Ann. N. Y. Acad. Sci. 1066: 106-118, 2005.

60. Agah, R., Pearce, J. A., Welch, A. J. Rate process model for arterial tissue thermal damage. Lasers in Surgery and Medicine 15: 176-184, 1994.

61. Joshua, T., Bernard, C, Vargas, G., McNally, K.M., and Welch, A. J. Pulsed laser-induced thermal damage in whole blood. J. Biomedical Engineering 122: 196-202, 2000.

62. Kinzler, V.B., Kenneth, W. The multistep nature of cancer. Trends Genet 9: 138-141, 1993.

63. Grizzi, F., Maurizio, C.I. Cancer: looking for simplicity and finding complexity. Cancer Cell International 6(4): 1-7, 2006.

64. Brafford, P. and Herlyn, M. Gene expression profiling of melanoma cells – searching the haystack, J Transl. Med.3 (2): 1-2, 2005.

65. Szathmary, E., Jordan, F., Pal, C. Molecular biology and evolution: Can genes explain biological complexity? Science 292: 1315-1316, 2001.

66. Chen, W.R., Carubelli, R, Liu, H, and Nordquist, R.E. Laser immunotherapy: A novel treatment modality for metastatic tumors. Molecular Biotechnology 25(1): 37-43, 2003.

67. Chen, W.R., Liu, H., Ritchy, J., Bartels, K.E., Lucroy, M.D., and Nordquist, R.E. Effects of different components of laser immunotherapy in the treatment of metastatic tumors in rats. Cancer Research 62: 4295-4299, 2002.

68. Chen, W.R., Korbelik, M., Bartels, K.E., Liu H., Jinghai, Sun, and Nordquist, R.E. Enhancement of laser cancer treatment by a chitosan-derived immunoadjuvant. Photochemistry and Photobiology 81 (1): 190-195, 2005.

69. Kahn, T., Bettag, M., Ulrich, F. et al. MRI-guided laser-induced interstitial thermotherapy of cerebral neoplasm. J. Comput. Assist. Tomogr 18: 519-532, 1994.

70. Gnyawali, S.C., Chen, Y., Wu, F., Bartels, K.E., Wicksted, J.P., Liu, H., and Chen, W.R., Temperature Measurement on Tissue Surface during Laser Irradiation. Medical and Biological Engineering and Computing, accepted for publication, 2007.

APPENDIXES

Appendix A: Monte Carlo Simulation Codes

```
#include "mcsfd.h"
#defineSTANDARDTEST 0
#defineCOSZERO (1.0-1.0E-12)
#defineCOS90D 1.0E-6
/*************************************************/
/* Global Variables for RandomNum Generator      */
/*************************************************/
#defineMBIG 1000000000
#defineMSEED 161803398
#defineMZ 0
#defineFAC 1.0E-9
/*************************************************/
/* Random Number Generator                       */
/*************************************************/
double ran3(int *idum)
{   static int inext,inextp;
    static long ma[56];
    static int iff=0;
    long mj,mk;
    int i,ii,k;
    if(*idum<0 || iff==0)
    {    iff=1;
         mj=MSEED-(*idum<0 ? -*idum: *idum);
         mj%=MBIG;
         ma[55]=mj;
         mk=1;
         for(i=1;i<=54;i++)
         {    ii=(21*i)%55;
              ma[ii]=mk;
              mk=mj-mk;
              if(mk<MZ) mk+=MBIG;
              mj=ma[ii];
         }
         for(k=1;k<=4;k++)
         for(i=1;i<=55;i++)
         {     ma[i]-=ma[1+(i+30)%55];
               if (ma[i]<MZ) ma[i]+=MBIG;
         }
         inext=0;
         inextp=31;
         *idum=1;
```

```
    }
    if(++inext==56) inext=1;
    if(++inextp==56) inextp=1;
    mj=ma[inext]-ma[inextp];
    if(mj<MZ) mj+=MBIG;
    ma[inext]=mj;
    return mj*FAC;
}

double RandomNum(void)
{   static Boolean first_time=1;
    static int idum;
    if(first_time)
    {   if(STANDARDTEST) idum=-1;
        else idum=-(int)time(NULL)%(1<<15);
        ran3(&idum);
        first_time=0;
        idum=1;
    }
    return((double)ran3(&idum));
}

#undef MBIG
#undef MSEED
#undef MZ
#undef FAC

/*************************************************/
/* Calculates the weighting coefficient c.       */
/*************************************************/
void CalcC(Globals *g, Photon *p, int r)
{       double s,area;
        if(r==0) g->tphot=0;
        if(toupper(g->btype)=='G')
        {       s=g->beamdens*8*exp(-8*pow((r+0.5)*g->beamdr/g->beamr,2));
                area=2*PI*(r+0.5)*g->beamdr*g->beamdr;
                if(g->beamdr==0) p->c=1;
                else p->c=s*area/g->nphot;
        }
        else
        {       s=g->beamdens;
                area=2*PI*(r+0.5)*g->beamdr*g->beamdr;
                if(g->beamdr==0) p->c=1;
                else p->c=s*area/g->nphot;
        }
        g->tphot+=p->c*g->nphot;
```

```
}

/*****************************************************/
/* Initializes the photon packet                     */
/*****************************************************/
void LaunchPhoton(Globals *g, int i, Photon *p)
{       p->w=1.0-g->Rsp;
        p->dead=0;
        p->nlayeri=1;
        p->nbound=1;
        p->s=0;
        p->sleft=0;
        p->tru=0;
        p->x=(i+0.5)*g->beamdr;
        p->y=0;
        p->z=0;
        p->ux=0;
        p->uy=0;
        p->uz=-1;
}
/*****************************************************/
/* Calculates the boundary index of vector r.        */
/*****************************************************/
void nrerror(char *);
int CalcNVect(Globals* g, double* r)
{   int k,n=1000;
    double R=0.0;
    if(r[2]>0) n=0;
    else if(r[2]<=-g->maxdepth) n=g->nlayers+1;
    else
    {   for(k=1;k<=g->nlayers;k++)
        {    if(g->layer[k].type=='F')
                 if(r[2]<=-g->layer[k].hi && r[2]>-g->layer[k].hf) n=k;
             else
             {     R=r[0]*r[0]+r[1]*r[1]+(r[2]+g->layer[k].hi)*(r[2]+g->layer[k].hi);
                   R=sqrt(R);
                   if(R<=g->layer[k].hf) n=k;
             }
        }
    }
    if(n==1000) nrerror("CalcNVect Error.\n");
    return n;
}
/*****************************************************/
/* Calcs the index of the flat layer in which the  */
/* photon resides.                                   */
```

```
/*****************************************************/
int CalcNFlatVect(Globals* g, Photon *p)
{   int k,n=1000;
    if(p->z>0.0) n=0;
    else if(p->z<=-g->maxdepth) n=g->nlayers+1;
    else
    {   for(k=1;k<=g->nlayers;k++)
        {   if(g->layer[k].type=='F')
            {   if(p->z<=-g->layer[k].hi && p->z>-g->layer[k].hf) n=k;
            }
        }
    }
    if(n==1000) nrerror("CalcNFlatVect Error.\n");
    return n;
}
/*****************************************************/
/* Calculates the cos of the critical angles.       */
/*****************************************************/
double CriticalAngle(double ni,double nt)
{       double cos;
        cos= ni>nt ? sqrt(1.0-(nt*nt)/(ni*ni)) : 0.0;
        return cos;
}
/*****************************************************/
/* Calculates the Fresnel Reflectance at the bound.*/
/*****************************************************/
double RFresnel(double ni,double nt,double cosi,double *cost)
{       double r;

        if(ni==nt)
        {       *cost=cosi;
                r=0.0;
        }
        else if(cosi>COSZERO)
        {       *cost=cosi;
                r=(nt-ni)/(nt+ni);
                r*=r;
        }
        else if(cosi<COS90D)
        {       *cost=0.0;
                r=1.0;
        }
        else
        {       double sini,sint;
                double tcost;
```

```
                sini=sqrt(1-cosi*cosi);
                sint=ni*sini/nt;

                if(sint>=1.0)
                {       *cost=0.0;
                        r=1.0;
                }
                else
                {       double sinp,sinm,cosp,cosm;
                        *cost=tcost=sqrt(1-sint*sint);

                        cosp=cosi*tcost-sini*sint;
                        cosm=cosi*tcost+sini*sint;
                        sinp=sini*tcost+cosi*sint;
                        sinm=sini*tcost-cosi*sint;


        r=0.5*sinm*sinm*(cosm*cosm+cosp*cosp)/(sinp*sinp*cosm*cosm);
                }
        }
        return r;
}
/*****************************************************/
/* Records the photon weight transmitted at bound  */
/*****************************************************/

void RecordT(Globals *g,Photon *p, Store *s, Bound *b, double cos, int nb)
{       double r=p->x*p->x+p->y*p->y;
        r=sqrt(r);

        double ild,iad;
        int nl,na;

        if(toupper(g->layer[nb].type)=='F')
        {       ild=r/g->layer[nb].dl;
                nl=(int)ild;
        }
        else
        {       double a=acos((p->z+g->layer[nb].hi)/g->layer[nb].hf);
                ild=a/g->layer[nb].dl;
                nl=(int)ild;
        }

        iad=acos(cos)/g->da;
        na=(int)iad;
        if(na>g->na-1) na=g->na-1;
```

```
        if(nl>g->layer[nb].nl-1) b[nb-1].Tt+=p->c*p->w;
        else
        {       b[nb-1].Tt+=p->c*p->w;
                b[nb-1].Tl[nl]+=p->c*p->w;
                b[nb-1].Ta[na]+=p->c*p->w;
                b[nb-1].Tla[nl][na]+=p->c*p->w;
        }
        if(nb==g->nlayers+1) p->w=0;
}
/****************************************************/
/* Records the photon weight reflected at bound    */
/****************************************************/
void RecordR(Globals *g,Photon *p, Store *s, Bound *b, double cos, int nb)
{       double r=p->x*p->x+p->y*p->y;
        r=sqrt(r);

        double ild,iad;
        int nl,na;

        if(toupper(g->layer[nb].type)=='F')
        {       ild=r/g->layer[nb].dl;
                nl=(int)ild;
        }
        else
        {       double a=acos((p->z+g->layer[nb].hi)/g->layer[nb].hf);
                ild=a/g->layer[nb].dl;
                nl=(int)ild;
        }

        iad=acos(cos)/g->da;
        na=(int)iad;
        if(na>g->na-1) na=g->na-1;

        if(nl>g->layer[nb].nl-1) b[nb-1].Rd+=p->c*p->w;
        else
        {       b[nb-1].Rd+=p->c*p->w;
                b[nb-1].Rl[nl]+=p->c*p->w;
                b[nb-1].Ra[na]+=p->c*p->w;
                b[nb-1].Rla[nl][na]+=p->c*p->w;
        }
        if(nb==1) p->w=0;
}
/****************************************************/
/* Decides if the photon will transmit or reflect */
/* at the bottom boundary of a flat layer          */
```

```
/*****************************************************/

void CrossDownOrNot(Globals *g,Photon *p,Store *s,Bound *b,int nb)
{       double uz=SIGN(p->uz)*p->uz;
        double uz1;
        double r=0;
        int layer=p->nlayeri;
        double ni=g->layer[layer].n;
        double nt=g->layer[layer+1].n;
        double coscrit=CriticalAngle(ni,nt);
        if(uz<=coscrit) r=1.0;
        else r=RFresnel(ni,nt,uz,&uz1);

        if(RandomNum() > r)
        {       p->uz=SIGN(p->uz)*uz1;
                p->ux*= ni/nt;
                p->uy*= ni/nt;
                p->nlayeri=nb;
                RecordT(g,p,s,b,uz,nb);
        }
        else
        {       p->uz=-p->uz;
                RecordR(g,p,s,b,uz,nb);
        }
}
/*****************************************************/
/* Decides if the photon will transmit or reflect */
/* at the top boundary of a flat layer          */
/*****************************************************/
void CrossUpOrNot(Globals *g,Photon *p,Store *s,Bound *b,int nb)
{     double uz=SIGN(p->uz)*p->uz;
      double uz1;
      double r=0;
      int layer=p->nlayeri;
      double ni=g->layer[layer].n;
      double nt=g->layer[layer-1].n;
      double coscrit=CriticalAngle(ni,nt);

      if(uz<=coscrit) r=1.0;
      else r=RFresnel(ni,nt,uz,&uz1);
      if(RandomNum() > r)
      {  p->uz=SIGN(p->uz)*uz1;
           p->ux*= ni/nt;
           p->uy*= ni/nt;
           p->nlayeri=nb-1;
              RecordR(g,p,s,b,uz,nb);
```

```
	}
	else
	{	p->uz=-p->uz;
		RecordT(g,p,s,b,uz,nb);
	}
}
/*****************************************************/
/* Calculates the Surface Normal Vector to the photon*/
/*****************************************************/
void CalcUR(Globals *g,Photon *p,double *ur,int nb)
{	ur[0]=p->x;
	ur[1]=p->y;
	ur[2]=p->z+g->layer[nb].hi;

	double r=sqrt(ur[0]*ur[0]+ur[1]*ur[1]+ur[2]*ur[2]);
	ur[0]/=r;
	ur[1]/=r;
	ur[2]/=r;
}
/*****************************************************/
/* Calculates the dot product between to vectors   */
/*****************************************************/
double DotProd(double *v1,double *v2)
{	double cos=0;
	int i;
	for(i=0;i<3;i++) cos+=v1[i]*v2[i];
	return cos;
}
/*****************************************************/
/* Transmits through a Spherical boundary	*/
/*****************************************************/
void Transmit(Globals *g,Photon *p,double *up,double *ur,double cost,int layer,int
layerf)
{	double cosi=DotProd(ur,up);
	double r[3];
	int i;
	double ni=g->layer[layer].n;
	double nt=g->layer[layerf].n;
	cost*=SIGN(cosi);
	double sini=sqrt(1-cosi*cosi);
	double sint=sqrt(1-cost*cost);
	double ratio=ni/nt;

	for(i=0;i<3;i++) r[i]=cost*ur[i]+ratio*up[i]-ratio*cosi*ur[i];

	p->ux=r[0];
```

```
        p->uy=r[1];
        p->uz=r[2];
        p->nlayeri=layerf;
}
/*****************************************************/
/* Reflects at a Spherical boundary */
/*****************************************************/
void Reflect(Globals *g,Photon *p,double *up,double *ur,double cost,int layer,int layerf)
{     double cosi=DotProd(ur,up);
      double r[3];
      int i;
      double ni=g->layer[layer].n;
      double nt=g->layer[layerf].n;

      for(i=0;i<3;i++) r[i]=-2.0*cosi*(ur[i]);
      p->ux=up[0]+r[0];
      p->uy=up[1]+r[1];
      p->uz=up[2]+r[2];
}
/*****************************************************/
/* Crosses a photon into spherical boundary       */
/*****************************************************/
void CrossInOrNot(Globals *g,Photon *p,Store *s,Bound *b,double *ur,double
*up,double cosi)
{       double cost;
        double rfres=0;
        int nb;
        int layer=p->nlayeri;

        nb=p->nbound;
        int layerf=CalcNFlatVect(g,p);
        if(g->layer[nb].type=='S')
        {       if(nb==g->nlastf+1 && nb==layer);
                else if(layer==nb && nb!=g->nlastf+1) layerf=layer-1;
                else layerf=nb;
        }
        else
        {       if(nb==layer) layerf=layer-1;
                else layerf=nb;
        }

99999999999999999999    double ni=g->layer[layer].n;
        double nt=g->layer[layerf].n;

      double coscrit=CriticalAngle(ni,nt);
```

```
        if(cosi<coscrit) rfres=1.0;
    else rfres=RFresnel(ni,nt,cosi,&cost);

    if(RandomNum() > rfres)
    {   RecordT(g,p,s,b,cost,nb);
            Transmit(g,p,up,ur,cost,layer,layerf);
    }
    else
    {   RecordR(g,p,s,b,cost,nb);
            Reflect(g,p,up,ur,cost,layer,layerf);
    }
}
```

Appendix B: MRI Temperature Mapping Codes (Mathematica)

```
r="C:\MRIdata\Phantum4Apr1\4\2dseq";
 im="C:\MRIdata\Phantum4Apr1\5\2dseq";
dr=Partition[Partition[Partition[If[#    0,1,#]&/@BinaryReadList[r,"Integer16"],128],128]
,20];
 Length[dr]
ar=dr[[12]][[10]];
dim=Partition[Partition[Partition[If[#    0,1,#]&/@BinaryReadList[im,"Integer16"],128],
128],20];
 aim=dim[[12]][[10]];
 ratio8=N[aim/ar,5];
 Phase8=ArcTan[ratio8];
 ListDensityPlot[Phase8,ColorFunction    Hue];
 br=dr[[1]][[10]];
 bi=dim[[1]][[10]];
 ratio1=N[bi/br,4];
 Phase1=ArcTan[ratio1];
 ListDensityPlot[Phase1,ColorFunction    Hue];
 deltaPhase=Phase8-Phase1;
ListDensityPlot[deltaPhase,ColorFunction    Hue];
 dmag1=BinaryReadList["C:\MRIdata\Phantum4Apr1\2\2dseq","Integer16"];
 dmag2=Partition[Partition[Partition[dmag1,128],128],20];
 amg=dmag2[[1]][[11]];
 criteria=If[#>900,1.,0]&;
 g=Map[criteria,amg,{2}];
 mapphase=g*deltaPhase;
mapphase//MatrixForm;
Do[If[mapphase[[i,j]]<0,mapphase[[i,j]]=mapphase[[i,j]]+    ],{i,128},{j,128}];
 ListDensityPlot[mapphase,PlotRange    All,ColorFunction    Hue,Mesh    False];
    =42.57*10^6;
 B=7;
 TE=30*10^-3;
    =-10^-8;
 deltaT=Abs[mapphase/(    *B*TE*    )];
 MatrixForm[deltaT];
 Max[deltaT]
 35.1412
 ListDensityPlot[deltaT,PlotRange    All,Mesh    False,ColorFunction    Hue];
fig1=ShowLegend[ListDensityPlot[deltaT,PlotRange    All,Mesh    False,ColorFunction
   Hue,ColorFunctionScaling    True,DisplayFunction    Identity],{Hue,80,"45       C","20
C",LegendPosition    {1.05,-0.95}LegendSize    {0.2,2}}]
ListPlot3D[Table[deltaT+(0.10Random[]-.15)],ColorFunction    Hue]
 ListDensityPlot[deltaT,ColorFunction    Hue]
 row1=deltaT[[54]];
row2=deltaT[[55]];
```

```
r1=Table[row1];
r2=Table[row2];
a1=ListPlot[r1,PlotJoined    True,PlotStyle    RGBColor[0,1,0]];
 a2=ListPlot[r2,PlotJoined    True,PlotStyle    RGBColor[1,0,0]];
 Show[{a1,a2}]
```

Appendix C: IR Surface Temperature Mapping Codes (Matlab)

```
%experimental data for chicken with camera, each element is one pixel
%increament from center of a image/absolute temperature
T=[44.25 44.13 43.78 43.54 42.41 42.06 41.33 40.98 39.64 38.51 37.86 36.8 36.18 35.54
35.16 34.11 33.47 32.33 32.16 31.49 31.15 30.93 29.79 29.57 29.2 29.09 28.45 27.98
27.39 27.55 27.87 27.28 26.75 26.49 26.81 26.17 26.27 26.59 26.22 25.95 25.95 25.58
25.68 25.14 25.07 25.21 24.81 24.74 24.68 24.68 24.41];
%cartisian coordinates(x,y)
r=0:0.3:15;%pixels converted to mm
theta=0:pi/25:2*pi;
for i=1:51;%angular index
   for j=1:51;%radial index
      x(j,i)=r(j)*cos(theta(i));%x&y are matrices of ixj=51x51,
      y(j,i)=r(j)*sin(theta(i));%i for theta,j for r
      T1(j,i)=T(j);%T1 has col.elements all same like r1 col.has all
                  %elements the first element of T above.
   end
end
%figure, contour(x,y,T1,100)
figure, surfc(x,y,T1),shading interp
figure, pcolor(x,y,T1), shading interp %pseudocolor p1
```

VITA

Surya C. Gnyawali

Candidate for the Degree of
Doctor of Philosophy

Title: STUDY OF TISSUE TEMPERATURE DISTRIBUTION DURING LASER-IMMUNOTHERAPY FOR CANCER TREATMENT

Major Field: Physics Minor Field: Biomedical Physics

BIOGRAPHICAL

Education:

- ●PhD in Physics / Biomedical Physics, May 2007, Oklahoma State University
- ●MPhil in Physics /Thin-Film Physics, September 2001, Kathmandu University
- ●MSc in General Physics, August 1994, Tribhuvan University
- ●Bachelors Degree in Science, Trichandra College, Kathmandu, Nepal

Experiences:

- ●Teaching / Research Assistant of Physics, Department of Physics, Oklahoma State University, 2002-2007
- ●Research Assistant, Biomedical Engineering Program, University of Central Oklahoma, 2004-2007
- ●Assistant Professor of Physics, Kathmandu University, Nepal, 1997-2002

Activities and Awards:

- ● American Association of Physicists in Medicine, 2006-Present, ID#30463
- ● Physical Society of Nepal, life member
- ● Outstanding Leadership Award, International Students Organization (ISO)-Oklahoma State University, 2004
- ● Best Student Presenter Award, Student Conference of Sigma Xi, Seattle, 2005
- ● Outstanding Physics Student Award, Nepal-Japan Friendship Organization, 1991-1993

Name: Surya C. Gnyawali Date of Degree: May, 2007

Institution: Oklahoma State University Location: Stillwater, Oklahoma

Title: STUDY OF TISSUE TEMPERATURE DISTRIBUTION DURING LASER-IMMUNOTHERAPY FOR CANCER TREATMENT

Page in Study: 135 Candidates for the Degree of Doctor of Philosophy

Major Field: Physics Minor Field: Biomedical Physics

Scope and Method of Study: The ideal cancer treatment modality should not only cause primary tumor suppression but also induce an anti-tumor immunity, which is essential in controlling metastatic tumors. Motivation of this work is to monitor temperature during laser-cancer treatment. A Monte Carlo method for the light transport in tissue and a finite difference method for the solution of heat diffusion equation were performed to estimate the laser dose parameters, and concentration levels of dye and immunoadjuvant. The specimens used were gelatin phantom, rats and mice. Magnetic Resonance Imaging thermometry (MRT) and infrared thermography (IRT) have been used for the measurement of temperature in the biological tissues during treatment of the primary tumors. Thermal imaging is used to estimate the laser-dose in application to cancer treatment. The thermal imaging and dose calculation can increase the level of safety in the treatment by providing information on target tissue and also on surrounding normal tissue.

Findings and Conclusions: Magnetic Resonance Imaging (MRI) has been applied to measure the thermal distribution in gel phantom and tumor-bearing rats during laser treatment. Infrared thermography has been applied to measure the surface temperature under the same conditions in tumor-bearing mice. Intratumoral injection of both indocyanine green (ICG) and glycated chitosan (GC) followed by 805-nm laser irradiation has been found efficacious in the cancer treatment. The temperature rise with ICG and laser combination therapy was about 25 ^{0}C and with the ICG, GC, and laser combination therapy, the temperature increased by 30 ^{0}C. This infers that ICG and GC injection potentiates the laser-immunotherapy. In both the cases, the tumor temperature attains the cancer cell damage temperature range of 60 ^{0}C - 70 ^{0}C resulting in an increase in the survival time of the treated mice. More importantly, the temperature profiles in this study agree with the Monte Carlo simulation results. In summary, a combination therapy using a laser, a laser-absorbing dye, and an immunoadjuvant guided by temperature measurement probes, such as MRT and IRT, is an effective treatment modality.

Advisor's Approval: James P. Wicksted